



# Politecnico di Bari

Repository Istituzionale dei Prodotti della Ricerca del Politecnico di Bari

3D-printing techniques for low-cost production of microfluidic devices: An experimental study on the design and development of 3D-printed chips for improving mixing process and

This is a PhD Thesis

*Original Citation:*

3D-printing techniques for low-cost production of microfluidic devices: An experimental study on the design and development of 3D-printed chips for improving mixing process and DNA extraction within microfluidics / Zeraatkar, Mojtaba. - ELETTRONICO. - (2023). [10.60576/poliba/iris/zeraatkar-mojtaba\_phd2023]

*Availability:*

This version is available at <http://hdl.handle.net/11589/248060> since: 2023-02-28

*Published version*

DOI:10.60576/poliba/iris/zeraatkar-mojtaba\_phd2023

Publisher: Politecnico di Bari

*Terms of use:*

(Article begins on next page)



Politecnico  
di Bari

Department of Mechanics, Mathematics and Management

MECHANICAL AND MANAGEMENT ENGINEERING

Ph.D. Program

SSD: ING-IND/16-TECHNOLOGIES AND PROCESSING SYSTEMS

**Final Dissertation**

---

**3D-printing techniques for low-cost production of microfluidic devices: An experimental study on the design and development of 3D-printed chips for improving mixing process and DNA extraction within microfluidics**

---

by:

**Mojtaba Zeraatkar**

Supervisors:

Prof. Gianluca Percoco

Prof. Marco Donato de Tullio

*Coordinator of Ph.D Program:  
Prof. Demelio*

---

*Course n°34, 01/11/2018-31/01/2022*

## **Abstract**

Micromixers are one of the most important components in microfluidic devices, which is often required for sample dilution, reagent homogenization, and chemical or biological reactions. Mixing in microfluidic devices, characterized by low Reynolds numbers, is related to the laminar regime of the flow, resulting in a slow process that demands long time and length of the channel for complete mixing. In the past two decades, the vast majority of microfluidic micromixers have been built in polydimethylsiloxane (PDMS) by soft-lithography. The need for accessible and inexpensive microfluidic devices requires new manufacturing methods and materials as a replacement for traditional soft-lithography and PDMS.

Recently, with the advent of modern additive manufacturing (AM) techniques, 3D printing has attracted attention for its use in the fabrication of microfluidic devices. The purpose of this study is to introduce an alternative construction for microfluidic micromixers, where the effect of the extruded filaments in the Fused Filament Fabrication (FFF) technique is used to enhance mixing performance within microfluidic micromixers. A simple Y-shaped micromixer was designed and printed using FFF technique. Experimental and numerical studies were conducted to investigate the effect of the extruded filaments on the flow behavior. The experimental results showed that the presence of geometrical features on microchannels, due to the nature of the FFF process, can act as ridges and increase mixing performance similar to slanted groove mixers (SGM) and staggered herringbone mixer (SHM), with the difference that the patterned ridges in FFF method are an inherent property of the process. In comparison to passive and active micromixers, no complexity was added in the fabrication process, and the ridges are an inherent property of the FFF process. The unibody micromixers made through Polyjet, SLA, and FFF platforms are examined and compared in terms of performance and limitations of the different fabrication platforms. The results showed that FFF-printed micromixers have better performance in mixing two fluids at low flow rates.

Nucleic acid extraction is one of the essential steps required in the workflow of genetic analyses. In this study, a microfluidic chip is designed and fabricated for lysis and DNA extraction using magnetic beads separation method. The chip design includes three main processes: Lysis, Binding, and Extraction processes.

**Keywords:** Additive manufacturing; 3D-printing; extrusion-based printing; FFF printing; microfluidic micromixers; mixing enhancement; DNA extraction

# List of Contents

<b>Chapter 1 : Introduction</b> .....	11
1.1 Introduction.....	12
1.2 Scope of the Thesis .....	13
1.3 Structure of the Thesis .....	14
<b>Chapter 2 : Microfluidics</b> .....	15
2.1 Introduction.....	16
2.2 Microfluidics Fundamentals .....	16
2.2.1 Reynolds and Péclet numbers .....	16
2.2.2 Diffusion .....	17
2.2.3 Conservation of mass .....	19
2.2.4 Conservation of momentum.....	20
2.2.5 Navier-Stokes equations .....	21
2.2.6 Dean Flow .....	22
2.3 Mixing in Microfluidics .....	23
2.3.1 Passive Micromixers.....	24
2.3.2 Active Micromixers .....	29
2.4 Manufacturing of Microfluidic Devices .....	34
2.4.1 3D Printed Microfluidic Devices .....	38
2.5 Microfluidics for Lysis and DNA Extraction .....	46
2.5.1 Chemical lysis.....	49
2.5.2 Mechanical lysis.....	50
2.5.3 Electroporation lysis .....	51
2.5.4 Laser lysis .....	52
2.5.5 Thermal lysis.....	53
<b>Chapter 3 : Materials and Methods</b> .....	56
3.1 Introduction.....	57
3.2 FFF-Printing Parameters Affecting on Fluidic Behavior.....	57
3.2.1 Design and Fabrication of the Micromixers.....	59
3.2.1.1 Post Printing Steps .....	66
3.2.1.2 Materials and Chemicals.....	67

3.2.1.3	Instrumentation .....	69
3.2.1.4	Experimental setup.....	72
3.2.2	Numerical Simulation .....	74
3.2.3	Colorimetric Analysis .....	76
3.3	Design Lysis and DNA Extraction Chip.....	80
<b>Chapter 4</b>	<b>: Results and Discussion .....</b>	<b>88</b>
4.1	Introduction.....	89
4.2	The Effect of Extruded Width on Mixing.....	89
4.3	The Effect of the Material and Printer .....	96
4.3.1	Design of Experiments.....	96
4.3.2	Experiments and results .....	99
4.4	Experimental-Numerical Study.....	106
4.4.1	Fabrication .....	106
4.4.2	Experimental setup.....	107
4.4.3	Experimental and numerical results .....	108
4.5	Comparison of FFF devices with SLA and Polyjet .....	113
4.6	Chip Fabrication for Lysis and DNA Extraction .....	119
4.6.1	Experimental setup.....	119
<b>References</b>	.....	<b>129</b>
<b>Appendix A</b>	.....	<b>137</b>
<b>Appendix B</b>	.....	<b>141</b>

## List of Figures

<b>Figure 2-1.</b> Schematic illustration of Dean vortices.....	23
<b>Figure 2-2.</b> Left: Y-shaped mixer with a zigzag channel; Right: Serpentine mixer. ....	25
<b>Figure 2-3.</b> Diagram of serpentine laminating micromixer with F-shape units .....	26
<b>Figure 2-4.</b> Schematic diagram of one-and-a-half cycles of the SHM.....	27
<b>Figure 2-5.</b> Schematic diagram of a model for ultrahydrophobic drag reduction .....	28
<b>Figure 2-6.</b> Fluorescence micrographs of mixing between two streams.....	29
<b>Figure 2-7.</b> Diagram of a SAW mixer;.....	31
<b>Figure 2-8.</b> Active micromixer by pulsation .....	32
<b>Figure 2-9.</b> Experimental results of mixing by perturbed flows .....	32
<b>Figure 2-10.</b> Schematic drawing representing components of the thermal disturbance micromixer. ...	33
<b>Figure 2-11.</b> Configuration of the flow: the microchannel, the electrodes, and the two fluids used. ...	34
<b>Figure 2-12.</b> Schematic showing the required steps for fabrication the mold by soft-lithography. ....	36
<b>Figure 2-13.</b> Schematic diagram of the fabrication process.....	37
<b>Figure 2-14.</b> Schematic of the SLA printer. ....	39
<b>Figure 2-15.</b> Schematic of the Polyjet printer. ....	40
<b>Figure 2-16.</b> Schematic of the FFF printer.....	41
<b>Figure 2-17.</b> 3D-printed molds for PDMS microfluidic devices. ....	42
<b>Figure 2-18.</b> Microfluidic device made by SLA .....	43
<b>Figure 2-19.</b> 3D-printed microfluidic components. ....	44
<b>Figure 2-20.</b> 3D-printed reactionware;.....	45
<b>Figure 2-21.</b> CAD designed versus 3D printed channels. ....	46
<b>Figure 2-22.</b> 3D printed TPU microfluidic device .....	46
<b>Figure 2-23.</b> Overview of magnetic bead-based DNA extraction.....	48
<b>Figure 2-24.</b> Schematic model of the cell membrane.....	48
<b>Figure 2-25.</b> Schematic representation of a microfluidic device for chemical lysis method. ....	49
<b>Figure 2-26.</b> Schematic representation of a microfluidic device for mechanical lysis method. ....	50
<b>Figure 2-27.</b> Schematic of the device with nanoscale barbs .....	50
<b>Figure 2-28.</b> Schematic representation of a microfluidic device for electrical lysis method. ....	51
<b>Figure 2-29.</b> Schematics of the low-voltage DC micro-electroporation chip. ....	52
<b>Figure 2-30.</b> Schematic representation of the laser lysis in microfluidics. ....	53
<b>Figure 2-31.</b> Schematic representation of a microfluidic device for thermal lysis method. ....	53
<b>Figure 2-32.</b> Schematic representation of the integrated microfluidic system.....	54
<b>Figure 2-33.</b> Photograph of the microfluidic induction heating system.....	55
<b>Figure 3-1.</b> Schematic showing the main FFF printing parameters .....	58
<b>Figure 3-2.</b> Performance of mixing in a Y-shape micromixer .....	59
<b>Figure 3-3.</b> CAD illustrations of the micromixer design with dimensions in mm. ....	60
<b>Figure 3-4.</b> Printing parameters.....	60
<b>Figure 3-5.</b> CAD drawing of the designed micromixer with dimensions in mm .....	62
<b>Figure 3-6.</b> Schematic showing the movement path of printing nozzle with a line width of 400 $\mu\text{m}$ . 63	

<b>Figure 3-7.</b> showing occlusion of the inlets with outer wall line width of 600 $\mu\text{m}$ .....	64
<b>Figure 3-8.</b> Manual calibration of the Ultimaker printers using calibration card.....	66
<b>Figure 3-9.</b> FFF 3D-printed micromixer with brim after removing from the build plate. ....	66
<b>Figure 3-10.</b> Supports under the connectors of a FFF printed mixer with gray PLA. ....	67
<b>Figure 3-11.</b> Preparation a mixture of DI water and Methylene blue. ....	69
<b>Figure 3-12.</b> FFF printers. Left: Ultimaker 3; Right: Ultimaker S5.....	70
<b>Figure 3-13.</b> SLA printers. Left: Formlabs Form 2; Right: MiiCraft Ultra 50.....	70
<b>Figure 3-14.</b> Stratasys Objet30 Polyjet printer.....	71
<b>Figure 3-15.</b> Left: High Precision Conoscan; Right: Nikon Eclipse MA200 microscope. ....	72
<b>Figure 3-16.</b> Canon camera with a macro lens used for capturing images from top of channels. ....	72
<b>Figure 3-17.</b> Transparent double-sided tape is applied to the top and bottom of the device.....	73
<b>Figure 3-18.</b> BS-300 Braintree syringe pumps for injecting solutions with disposable syringes. ....	73
<b>Figure 3-19.</b> Experimental setup and detection system for testing microfluidic systems.....	74
<b>Figure 3-20.</b> Experimental setup and detection system for testing microfluidic systems. ....	74
<b>Figure 3-21.</b> High quality structured–unstructured mesh.....	76
<b>Figure 3-22.</b> Data flowchart of the colorimetric analysis.....	77
<b>Figure 3-23.</b> Captured image from the top of the device .....	78
<b>Figure 3-24.</b> Displaying red intensity in different ROIs as an image.....	79
<b>Figure 3-25.</b> Mixing trend diagrams at flow rates of 50 and 100 $\mu\text{L}/\text{min}$ .....	80
<b>Figure 3-26.</b> Normalized mean square errors (MSEs) versus different ROIs .....	80
<b>Figure 3-27.</b> Block diagram of the steps of DNA extraction implemented on microfluidics. ....	81
<b>Figure 3-28.</b> CAD model of the initial chip .....	82
<b>Figure 3-29.</b> Structure of the inlet (a), and channel (b) in lysis process. ....	83
<b>Figure 3-30.</b> 3D CAD model of lysis and binding chip. ....	86
<b>Figure 3-31.</b> Fluke PTi120 thermal camera. ....	87
<b>Figure 3-32.</b> Thermo Scientific™ NanoDrop™ .....	87
<b>Figure 4-1.</b> 3D CAD model of simple Y-shaped micromixer with dimensions in mm. ....	89
<b>Figure 4-2.</b> Captured images at different flow rates from the top of the device .....	91
<b>Figure 4-3.</b> Schematic showing the cross section of the extruded filaments. ....	91
<b>Figure 4-4.</b> 3D model of device 2 (line width: 400 $\mu\text{m}$ ) with actual parameters for the ridges.....	92
<b>Figure 4-5.</b> 3D model of device 3 (line width: 600 $\mu\text{m}$ ) with actual parameters for the ridges.....	92
<b>Figure 4-6.</b> Calculated Mean Square Error (MSE) .....	93
<b>Figure 4-7.</b> Calculated Mean Square Error (MSE) .....	93
<b>Figure 4-10.</b> Calculated Mean Square Error (MSE). ....	94
<b>Figure 4-11.</b> Calculated Mean Square Error (MSE) .....	95
<b>Figure 4-12.</b> Printing parameters.....	98
<b>Figure 4-13.</b> Photographs of two different fabricated channels. ....	99
<b>Figure 4-14.</b> Residual plots for length of mixing. ....	100
<b>Figure 4-15.</b> Main and interaction effects plots for the length of mixing. ....	101
<b>Figure 4-16.</b> Pareto chart of standardized effects.....	102
<b>Figure 4-17.</b> Full top view of 3D printed microfluidic devices, demonstrating transparency .....	103

<b>Figure 4-18.</b> Surface plot for predicting the length of mixing. ....	105
<b>Figure 4-19.</b> Two printed channels. ....	106
<b>Figure 4-20.</b> (a) and (b) are schematic showing the movement path of printing nozzle. ....	107
<b>Figure 4-21.</b> Experimental setup for measuring mixing performance in microfluidic channel .....	108
<b>Figure 4-22.</b> The extent of fluid mixing for different ridge topographies.....	109
<b>Figure 4-23.</b> CFD results by COMSOL .....	110
<b>Figure 4-24.</b> Influence of the ridge height-to-channel height ratio .....	111
<b>Figure 4-25.</b> Evolutions of the concentration distributions.....	112
<b>Figure 4-26.</b> Flow visualization of the streamlines in channel 3 (flow rate 10 $\mu\text{L}/\text{min}$ ). ....	113
<b>Figure 4-27.</b> Fabricated micromixers by three different methods of printing. ....	114
<b>Figure 4-28.</b> Complete mixing obtained with the Polyjet micromixer.....	115
<b>Figure 4-29.</b> Mixing obtained in Polyjet micromixer with different flow rates. ....	116
<b>Figure 4-30.</b> Mixing obtained in SLA micromixer. ....	116
<b>Figure 4-31.</b> Mixing obtained in FDM micromixer. ....	116
<b>Figure 4-32.</b> Regions of interest in the different microchannels. ....	117
<b>Figure 4-33.</b> Diagram of the mixing trend in the microchannel.....	117
<b>Figure 4-34.</b> Required channel length for complete mixing .....	118
<b>Figure 4-35.</b> Fabricated chips with FFF method. ....	120
<b>Figure 4-36.</b> Experimental setup and detection system for testing chips. ....	120
<b>Figure 4-37.</b> Different solutions used for the test.....	121
<b>Figure 4-38.</b> Schematic of the lysis process inside the Lysis-Binding chip.....	121
<b>Figure 4-39.</b> Control of temperature using a thermal camera. ....	122
<b>Figure 4-40.</b> Binding process. ....	122
<b>Figure 4-41.</b> Extraction chip showing the beads absorbed by an external permanent magnet. ....	123
<b>Figure 4-42.</b> Natural PLA and HT PLA performance at temperature 60 $^{\circ}\text{C}$ .....	124
<b>Figure 4-43.</b> Chemical Structure of PMMA and PLA polymers. ....	124
<b>Figure 4-44.</b> Fixing PMMA substrate on the build plate .....	125
<b>Figure 4-45.</b> Representation of the 3D-printing process on top of a PMMA substrate.....	126
<b>Figure 4-46.</b> Printed channels with different shapes of the roof. ....	127
<b>Figure 4-47.</b> printed chip with HT PLA and PMMA substrate.....	127
<b>Figure 4-48.</b> Modified CAD design standard fitting connectors.....	128
<b>Figure 4-49.</b> Extraction chip printed using a DLP printer.....	128

## List of Tables

<b>Table 2-1.</b> Various methods of mixing enhancement in microfluidic devices.....	35
<b>Table 2-2.</b> Comparison of different cell lysis methods. ....	55
<b>Table 3-1.</b> Process parameters and materials used for the fabrication of the micromixers. ....	62
<b>Table 4-1.</b> Measured values for the fabricated microchannel. ....	91
<b>Table 4-2.</b> Measured values for the fabricated microchannel. ....	92
<b>Table 4-3.</b> Measured values for the fabricated microchannel .....	92
<b>Table 4-4.</b> Mixing performance of three printed devices with different extruded width. ....	96
<b>Table 4-5.</b> Factors and levels.....	96
<b>Table 4-6.</b> Proposed design of experiments. ....	97
<b>Table 4-7.</b> Fixed printing parameters during the experiments. ....	98
<b>Table 4-8.</b> The performance of mixing in each FFF printed micromixer.....	99
<b>Table 4-9.</b> Non- standardized effects, T and P values in factorial design. ....	102
<b>Table 4-10.</b> Nominal values of ridge parameters and the measured values .....	106
<b>Table 4-11.</b> Required length for each Y-shape serpentine micromixer.....	119
<b>Table 4-12.</b> Optimized parameters settings to print 3D microfluidic devices.....	126

## Nomenclature

### List of Abbreviations

AM	Additive Manufacturing
ABS	Acrylonitrile butadiene styrene
CAD	Computer Aided Design
CFD	Computational Fluid Dynamics
CCD	Charge-coupled device
PDMS	Polydimethylsiloxane
SLS	Selective laser sintering
FFF	Fused Filament Fabrication
FDM	Fused Deposition Modeling
SLA	Stereolithography
FDA	Food and Drug Administration
DI	Deionized [water]
DNA	Desoxyribonucleic Acid
RNA	Ribonucleic acid
ROI	Regions of interest
DMD	Digital micromirror display
FDA	Food and Drug Administration
mTAS	Micro total analysis systems
TMP	Transmembrane potential
TPU	Thermoplastic polyurethane
DLP	Digital Light Projection
MJM	Multijet Modeling
MEMS	Micro-Electro-Mechanical-Systems
MSE	Mean square error
IDTs	interdigital transducers
LOC	Lab on a chip
LW	Width of extruded filament
PCR	Polymerase chain reaction
PLA	Poly-lactic acid
PMMA	Polymethyl methacrylate
PET	Polyethylene terephthalate
SHM	Staggered herringbone mixer
SAR	Split-and-recombine micromixers
SGM	Slanted-groove micromixer
UV	Ultraviolet

## List of Symbols and Variables

### Latin Symbols

<b>Variable</b>	<b>Meaning</b>
A	Cross-sectional area
B	Magnetic flux density
b	Air gap
c	Molar concentration
$D_{eq}$	Hydraulic diameter
De	Dean number
E	Electric field
F	Force
$f$	Frequency of the disturbance action
Re	Reynolds number
Pe	Peclet number
u	Velocity of fluid
w	Width of the channels
r	Radius
s	Second
m	mass
p	Pressure
P	Wetted perimeter
h	Height of the channels
$h_1$	Height of patterned ridges
$\alpha h$	Amplitude of the ridges

### Greek symbols

<b>Variable</b>	<b>Meaning</b>
$\eta$	Viscosity
$\theta$	Extruded angle
$\rho$	Fluid density
$\mu$	Fluid dynamic viscosity
$\nu$	Fluid kinematic viscosity
$\phi$	Flow rate
$\lambda$	Ridge period

# **Chapter 1 :**

# **Introduction**

## 1.1 Introduction

Microfluidics is an emerging field that studies the behavior and control of fluids that are constrained geometrically to small scales. It is an enabling technology to perform biological and chemical experiments at greatly reduced spatial scales, with minimal material consumption and high throughput. Microfluidics allows for handling of fluid with volumes typically in the range of nano to microliters ( $10^{-9}$  to  $10^{-6}$  L) or smaller in channels with characteristic dimensions ranging from millimeters to micrometers (thinner than a hair) [1]. A strong motivation in microfluidic comes from the technologies known as micro total analysis systems ( $\mu$ TAS) or lab-on-a-chip (LOC). A lab-on-a-chip is a miniaturized device that integrates one or several analyses into a single chip, which are usually done in a laboratory; analyses such as DNA sequencing or biochemical detection.

Microfluidics devices have received increasing attention due to their compact size, automatic operation, faster detection, less reagent, higher sensitivity and in-field use [2]. Recently, with outbreak of the severe acute respiratory syndrome coronavirus 2 (SARS-CoV-2), many COVID-19 tests can give results within hours without the need to send a sample to a laboratory; a simple form of miniaturized technology in health care application [3]. Drug development is another example in the importance of microfluidics. The median cost to develop a cancer drug and bring to US market is \$648.0 million, with a median time of a decade [4], which is a long and costly process and in the most cases with a failure rate of 95% [5]. Compared with conventional drug screening methods, a microfluidic-based system has superior advantages in cell environment, sample consumption, reaction time, and cost of the operation [6]. These are examples in the importance of microfluidics in health care applications. In the past two-three decades, numerous academic works published which have proved the concept of microfluidic devices in biomedical and chemical experiments however, the translation of this technology to marketed products has been limited. This limited success can partly be explained from the lack of robust and reproducible manufacturing and scale-up, challenges in formulation, limited characterization methods, and stringent regulatory requirements [7]. The need for accessible and inexpensive microfluidic devices requires new manufacturing methods and materials, a

replacement for traditional soft lithography and polydimethylsiloxane (PDMS). Recently, with the advent of modern additive manufacturing (AM) techniques, 3D-printing has attracted attention for the fabrication of microfluidic devices, due to its automated, assembly-free 3D fabrication, rapidly decreasing costs, and fast-improving resolution and throughput. It seems with progress in microfluidics and supporting technologies such as 3D printing, these devices will be more accessible to all people in future and easy to use such as smartphones, which open the possibility for novel applications including on-demand pharmaceuticals and pharmaceutical production, as well as wearable technologies.

One of the most important components in microfluidic devices are micromixers. Micromixers are often required for sample dilution, reagent homogenization, and chemical or biological reactions. The mixing process inside the small dimensions of microfluidic devices is a challenge. The difficulty related to mixing results from laminar flows that can be explained by low Reynolds number. As a result, mixing in microfluidic devices rely on diffusion phenomenon between the different species flows, which is an inherently slower process and requires a long channel to achieve sufficient mixing. In the past two decades, various systems for achieving mixing within a reasonable time and length of a microchannel have been introduced. These systems are generally divided into passive and active. While each method has its own advantages and disadvantages, the fabrication process of the microfluidic micromixers is also essential. Passive and active methods typically require complex geometries of ridges or grooves and need to have movable parts, which increase the difficulty for fabrication.

## **1.2 Scope of the Thesis**

The purpose of this study is to introduce an alternative construction for microfluidic micromixers using low-cost 3D printing method. The extrusion-based 3D printing processes are limited by poor surface finish, due to the filament, deposited into beads or strands. The present study demonstrates in one specific application, intrinsic surface limitations can be used to improve some features such as mixing performances in microchannels. In the scope of this

work a microfluidic chip for DNA extraction and purification will be designed, developed, and characterized. The chip includes three main processes: Lysis process, Binding process, and Extraction process. The chip should sufficiently remove impurities and other molecules to provide pure DNA.

### **1.3 Structure of the Thesis**

In chapter 2, the theoretical background relevant to microfluidics and mixing process within micro scale of the channels will be summarized, followed by a review of the state of the art of microfluidic micromixers. Passive and active methods for mixing will be described with an example of each method. The current manufacturing methods for microfluidic devices are reviewed with particular attention to the challenges associated with each method, and further explore opportunities with developing technologies including 3D printing as a potential replacement for rapid prototyping through soft-lithography. In the last part, the current methods for lysis and DNA extraction within microfluidics will be summarized.

In chapter 3, the materials and methods used for this research will be described. The process parameters and design of experiments will be performed. The designed devices will be fabricated with different printing parameters. The hardware and software including printers, chemicals, instruments, colorimetric analysis, and numerical study for conducting the research will be explained.

In chapter 4, the results of this study will be summarized and discussed.

# **Chapter 2 : Microfluidics**

## 2.1 Introduction

In this chapter, we first discuss basic theories of fluid dynamics that are essential to characterize microfluidic systems: Two important dimensionless numbers, Reynolds number and Peclet number, are discussed to characterize flows and diffusion in microchannels. Fick's laws of diffusion and laminar flows inside micro scale of the channels are explained.

We then introduce current methods for mixing inside microfluidics; the advantages and disadvantages of each method are stated. The following section introduces the manufacturing methods for fabrication of microfluidic devices with a particular attention to 3D printing methods as a potential replacement for PDMS. We also describe methods of genomic analysis including lysis and DNA extraction processes.

## 2.2 Microfluidics Fundamentals

### 2.2.1 Reynolds and Péclet numbers

The microscale of the flow channels in microfluidic devices increases the surface-to-volume ratio, which is advantageous for many biomedical applications. However, microfluidic devices also have limitations. One of the challenges is mixing, which is often required for sample dilution, reagent homogenization, and chemical or biological reactions. The difficulty related to mixing in a microfluidic device, results from laminar flows that can be explained by low Reynolds number. The Reynolds number is a function of the geometric characteristics of the channel such as hydraulic diameter ( $D_{eq}$ ), flow velocities ( $V$ ), and kinematic viscosities ( $\nu$ ). It is defined by the following equation:

$$Re = \frac{D_{eq} \times V}{\nu}$$

The hydraulic diameter ( $D_{eq}$ ) is given by the ratio of 4 times the cross-sectional area  $A$  and the wetted perimeter  $P$ :

$$D_{eq} = \frac{4 \times A}{P}$$

When the Reynolds number is small, the effect of the viscous force is larger, dampening out any flow irregularities that might aid in fluid mixing. The Reynolds number  $Re$  is used to

determine if the flow is laminar, transient, or turbulent. The critical Reynolds number changes depending on the criteria such as the shape of the flow, parameters to be focused, and choice of the characteristic velocity and length [8]. For example, flow in a pipe is considered to be laminar when  $Re < 2300$ , transient when  $2300 < Re < 4000$ , and turbulent when  $Re > 4000$  [1]. In microfluidic devices because of low hydraulic diameter, combined with typically small ( $\sim 1 \text{ mm s}^{-1}$ ) flow velocities and with typical kinematic viscosities of on the order of  $10^{-6} \text{ m}^2 \text{ s}^{-1}$ , leads to very small Reynolds numbers for flow in microchannels ( $\sim 0-10$ ) [2].

Péclet number is dimensionless number very useful in microfluidic applications. Generally, in the context of thermodynamics, the Péclet number is the ratio of the thermal energy convected to the fluid to the thermal energy conducted within the fluid. However, in microfluidics the Péclet number represents the ratio of the convection rate over the diffusion rate in the convection-diffusion transport system:

$$Pe = \frac{uL}{D}$$

Where,  $U$  represents linear flow velocity in the control volume,  $L$  represents the length scale of the flow and  $D$  is the diffusion constant.

The Strouhal number is another dimensionless number, generally associated with active micromixers and represents the ratio between the residence time of a species and the time period of disturbance [9]:

$$St = \frac{fD_{eq}}{u}$$

Where,  $f$  is the frequency of the disturbance action.

### **2.2.2 Diffusion**

Given the low Reynolds number within in microfluidic devices, these systems are unable to use the advantages of the turbulent mixing that exists in macro-scale systems. As a result, mixing in microfluidic devices rely on diffusion phenomenon between the different species flows, which is an inherently slower process and requires a long channel to achieve sufficient mixing [10]. Fick's first law of diffusion states that the rate of transfer of molecules from

regions of high concentration to regions of low concentration is proportional to the concentration gradient. In a one-dimensional model of diffusion, the law is expressed as:

$$J = -D \frac{\partial c}{\partial x}$$

where J is the flux (number of molecules per unit area per unit time e.g., mol m<sup>-2</sup> s<sup>-1</sup>); D is the diffusion coefficient (e.g., m<sup>2</sup>/s); and c is the concentration (e.g., mol m<sup>-3</sup>).

The continuity equation (see the next section 2.2.3) and Fick's first law can be combined into Fick's second law of diffusion, which can be expressed in one dimension as:

$$\frac{\partial c}{\partial t} = D \left( \frac{\partial^2 c}{\partial x^2} \right)$$

As it is clear, the diffusion process depends on a series of factors such as the temperature, type of solute and solvent. The diffusion coefficient (D) is the parameter that take represents the temperature and the type of solute and solvent in Fick's law. Interestingly, a relation between the macroscopically observed diffusion behavior in the form of the diffusion coefficient and a macroscopic property of the molecules in the form of the hydrodynamic radius R can be stated, which named the Stokes-Einstein equation:

$$D = \frac{k T}{6 \pi \mu R}$$

Where, k is Boltzmann constant, T is the temperature, R is the radius of the particles and  $\mu$  is the viscosity. The equation shows the temperature dependence of the diffusion coefficient and allows to estimate the diffusion coefficient of the molecules when the hydrodynamic radius is known.

There are various mathematical models that describe the movement of fluids and various engineering correlations that can be used for special cases. However, the most complete and accurate description comes from partial differential equations (PDEs). For instance, a flow field is characterized by balance in mass, momentum, and total energy described by the continuity equation, the Navier-Stokes equations, and the total energy equation.

### 2.2.3 Conservation of mass

Every fluid we consider is endowed with a non-negative density, usually denoted by  $\rho$ , which in the Eulerian setting is a scalar function of  $x, t$ . Its unit are mass per unit volume. If we introduce the following quantities:

$V \rightarrow$  measurement of the control volume

$S \rightarrow$  total area of the control volume

$\rho \rightarrow$  density of the fluid

$B \rightarrow$  extensive quantity unknown

$b \rightarrow$  intensive quantity associated with the extensive

$\vec{u} \rightarrow$  transport speed

$\vec{n} \rightarrow$  normal unit vector

Then, the conservation of mass equation, where:

$$B \equiv M$$

And,

$$b = 1$$

Hence:

$$\int_V \frac{\partial \rho}{\partial t} dV + \int_S \rho \vec{u} \cdot \vec{n} dS = 0$$

Applying the divergence theorem, according to which:

$$\int_V \nabla \cdot \vec{u} dV = - \int_S \vec{u} \cdot \vec{n} dS$$

We get to:

$$\int_V \left[ \frac{\partial \rho}{\partial t} + \nabla \cdot (\rho \vec{u}) \right] dV = 0$$

Since, the choice of the control volume is arbitrary, while the previous equation holds for an assigned control volume, the only possibility is to impose the equality of the integrand function to zero, which allows to derive the general expression conservation of mass in differential form:

$$\frac{\partial \rho}{\partial t} + \nabla \cdot (\rho \vec{u}) = 0$$

The density is constant so, we obtain the formulation for incompressible flows:

$$\nabla \cdot \vec{u} = 0$$

### 2.2.4 Conservation of momentum

Newton's second law is simply the law of conservation of momentum. It states that the time rate of change of momentum of a system of particles is equal to the sum of external forces acting on that body. With indicating the momentum with  $Q$ , it can be expressed as:

$$Q = \int_{V_0} \rho u dV$$

According to Newton's second law:

$$\frac{dQ}{dt} = F$$

Where,  $F$  indicates the set of all the forces acting on the material volume under examination, among which the contact forces  $F_S$  (pressure forces and viscous forces) and those of volume  $F_V$  (weight force, centrifugal force and Coriolis force) are distinguished.

By distinguishing between the contact forces and those due to pressure, we obtain:

$$F_S = - \int_{S_0} p n dS + F'_S$$

Using the Reynolds transport theorem:

$$\int_{V_0} \frac{\partial \rho u}{\partial t} dV + \int_{S_0} p u u n dS + \int_{S_0} p n dS = F'_S + F_V$$

The equation expresses the balance of the momentum in integral form.

By placing:

$$F_S = \int_{S_0} T ndS = \int_{S_0} (-pI + \tau) ndS \quad \text{and} \quad F_V = - \int_{V_0} \rho f dV$$

Where,  $T$  is the surface stress tensor,  $p$  is the pressure on the control volume,  $I$  is the identity tensor,  $\tau$  is the viscous stress tensor, acting on the surface of the control volume at each point,  $f$  is the vector of the volume forces. The expression of the momentum in integral form can be rewritten as:

$$\int_{V_0} \frac{\partial \rho u}{\partial t} dV + \int_{S_0} \rho u u ndS = - \int_{S_0} pI ndS + \int_{S_0} \tau ndS - \int_{V_0} \rho f dV$$

With applying the divergence theorem, and imposing the equality of the integrating function to zero to affirm the independence of the equation from the control volume, we obtain:

$$\frac{\partial \rho u}{\partial t} + \nabla (\rho u u) = -\nabla p + \nabla \tau + \rho f$$

Therefore, the following form is the balance of momentum equation which is valid for both Newtonian and non-Newtonian flows:

$$\rho \frac{Du}{Dt} = -\nabla p + \nabla \tau + \rho f$$

### 2.2.5 Navier-Stokes equations

The Navier-Stokes equations govern the motion of fluids and can be seen as Newton's second law of motion for fluids. By considering the constitutive equation for the Newtonian fluids:

$$\tau = -\frac{2}{3}\mu(\nabla \cdot u)I + 2\mu E$$

Where,  $E$  is the symmetrical part of the tensor  $(\nabla u)$ . By replacing this expression within the differential form of the balance of momentum equation, we obtained:

$$\rho \frac{Du}{Dt} = -\nabla p + \rho f - \frac{2}{3} \nabla[(\mu \nabla \cdot u)] + 2 \nabla(\mu E)$$

This expression is called the Navier-Stokes equation. By considering incompressible flows at constant viscosity in space, the following expression is obtained:

$$\rho \frac{Du}{Dt} = -\nabla p + \rho f + \mu \nabla^2 u$$

These equations are always solved together with the continuity equation. In microfluidics or especially in passive micromixers, there are no important thermal gradients, so the system of fluid dynamics equations remains as following:

$$\begin{cases} \nabla \cdot u = 0 \\ \rho \left( \frac{\partial u}{\partial t} + u \cdot \nabla u \right) = -\nabla p + \rho f + \mu \nabla^2 u \end{cases}$$

Whenever we consider mass transport of a dissolved species (solute species) or a component in a gas mixture, concentration gradients will cause diffusion. If there is bulk fluid motion, convection will also contribute to the flux of chemical species. We introduced the Péclet number as a ratio of the convection rate over the diffusion rate. Therefore, in convection-diffusion transport system, the system of equations is as follow:

$$\begin{cases} \nabla \cdot u = 0 \\ \rho \left( \frac{\partial u}{\partial t} + u \cdot \nabla u \right) = -\nabla p + \rho f + \mu \nabla^2 u \\ \frac{\partial c_\alpha}{\partial t} + u \cdot \nabla c_\alpha + D \nabla^2 c_\alpha = 0 \end{cases}$$

Where,  $c_\alpha$  is the normalized molar concentration.

### 2.2.6 Dean Flow

In flow through curved channel geometries, curvature amplifies a lateral instability that drives a secondary cross-sectional flow field (Dean flow) characterized by the presence of two counter-rotating vortices located above and below the horizontal plane of symmetry of the channel. Consequently, two axial vortices will be induced with fluid flowing towards the outer channel wall from the center of channel and flowing towards the inner channel wall at top and

bottom of the channel. The dimensionless Dean number ( $De$ ) describes the ratio between inertial forces and centrifugal forces [11]:

$$De = Re \cdot \sqrt{\frac{D_{eq}}{2R}}$$

Where,  $Re$  is the Reynolds number,  $D_{eq}$  the hydraulic diameter of the channel and  $R$  the radius of curvature, which is defined as the mean value of the inner and outer channel wall curvature  $r_1$  and  $r_2$ , respectively. For Dean numbers below 50 no Dean vortices will be induced, whereas for values above 50 Dean vortices will provide an additional means for mixing in microfluidic channels [8]. Due to the small dimension, Dean numbers in microchannels are usually low, limiting the mixing in the microchannels.

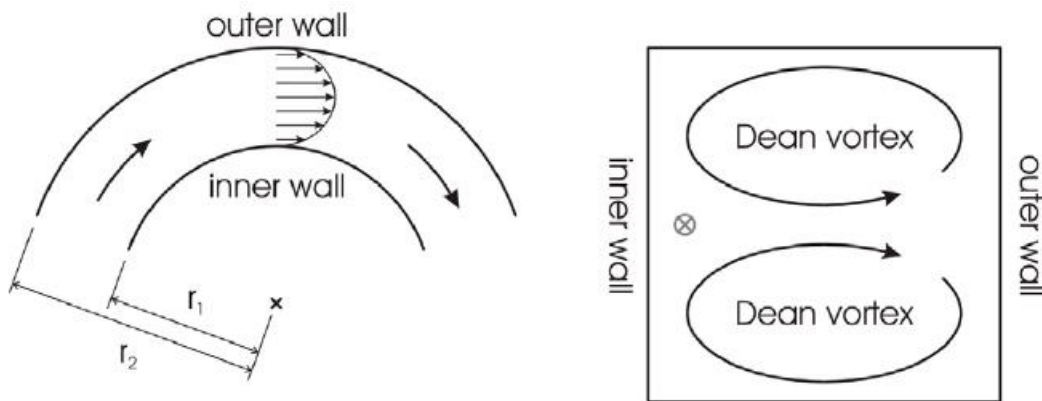


**Figure 2-1.** Schematic illustration of Dean vortices. Due to the higher fluid velocity centrifugal forces are larger in the center of the channel, resulting in two Dean vortices in the axial direction.

### 2.3 Mixing in Microfluidics

Microfluidic devices have a wide variety of chemical and biological applications, including biomedical diagnostics, DNA and protein analysis, food safety control, drug development, etc [12]. In the past two decades, these devices have received increasing attention. However, microfluidic devices also have limitations. One of the most important components in microfluidic devices are micromixers, which is often required for sample dilution, reagent homogenization, and chemical or biological reactions [13]. The mixing process inside the small dimensions of microfluidic devices is a challenge. The difficulty related to mixing results from laminar flows that can be explained by low Reynolds number. As a result, mixing in microfluidic devices rely on diffusion phenomenon between the different species flows, which

is an inherently slower process and requires a long channel to achieve sufficient mixing. In general, the efficient micromixers are those which can provide mixing between two or more fluids in:

- Short time
- Short length of channel
- Minimum energy consumption
- High mixing ratio

In the past two decades, various systems for solving mixing problems and enhance mixing in microfluidic devices have been introduced. These systems are generally divided into two groups, namely, passive and active [2, 10, 13-17]. On the other hand, active micromixers increase contact area between the fluids or induce the chaotic advection by using an external energy source, thus enhancing the mixing process [2]. Evaluating parameters for the performance of micromixer include the quality of mixing, channel length, mixing time and fabrication process. The ideal mixer is the ones that achieves the best mixing quality in the shortest time and length of channel; and on the other hand, the fabrication process is not difficult.

### **2.3.1 Passive Micromixers**

Passive micromixers do not require external energy source except the energy for driving the fluids. In these systems tried to enhance diffusion or chaotic advection by altering the structure or configuration of channels. The fabrication process and operation of these type of micromixers is easier because of not having moving parts within the micromixer [18]. This type of micromixers are incorporated into the system during the fabrication process and they are not externally controlled by users [19]. In the last years many new passive micromixers have been reported based on the structure of Y- and T-type [20], zigzag [21], serpentine [22], etc. In traditional Y-shaped or T-shaped, two different fluids are sent to be mixed through two separate inlets which join in a main mixing channel. The configuration of the inlets can be mainly of two types:

- T-shaped mixer: the inlet channels perpendicular to the mixing channel.

- Y-shaped mixer: the inlet channels inclined with respect to the mixing channel.

It should be noted that, for the traditional T- and Y-type micromixers, the mixing is rather slow and a long mixing channel is required since the mixing solely depends on diffusion of the species at the interface between the two fluids. In order to enhance the mixing, different configurations for the main channel proposed by adding obstacles or changing the geometry of the channel. Figure 2-2 show two proposed configurations; zigzag and serpentine for the main channel.

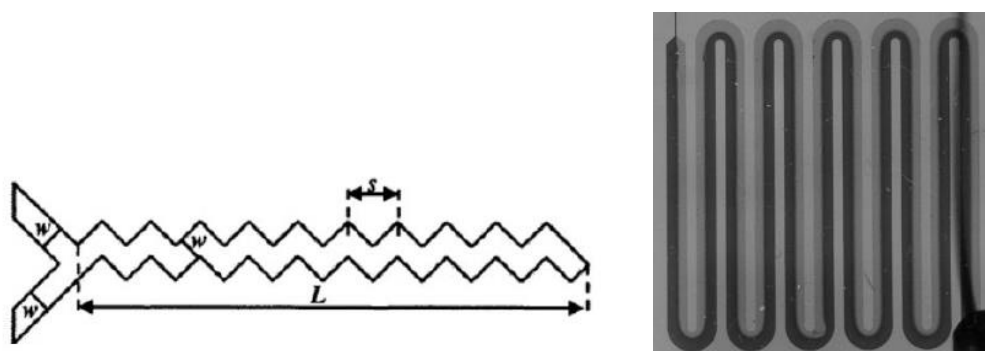


**Figure 2-2.** Left: Y-shaped mixer with a zigzag channel ( $w$  width of the channel,  $s$  length of the period,  $L$  total length of the channel); Right: Serpentine mixer.

Mixing process can be enhanced by using complex geometries or by twisting the inlet streams to reduce the mixing path. Once streams are combined, they can also be split and combined again in series to enhance mixing further. This type of micromixer is named Split-And-Recombine (SAR) mixer. Kim *et al.* [23] utilized a serpentine channel with F-shaped mixing units in order to realize the benefit of stream splitting and recombination to mixing efficiency. As shown in Figure 2-3, the splitting and recombination mechanism is obtained by dividing the fluid flows into smaller segments and recombining them in such a way to increase the contact area between different fluids. There are also many other micromixers which used the advantages of traditional T- and Y-shaped mixers in order to enhance mixing [24-26].

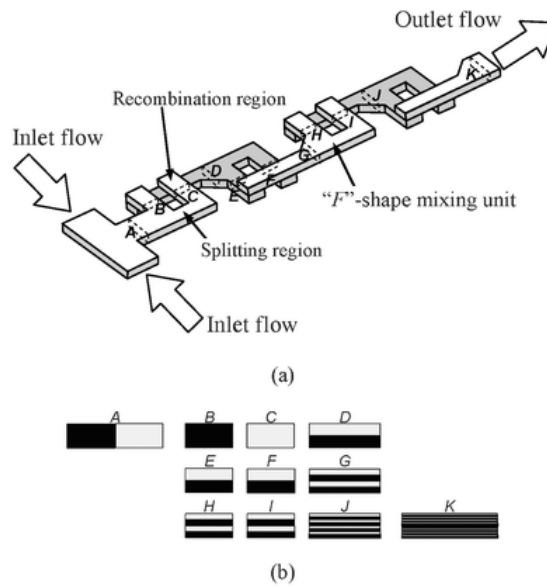


**Figure 2-3.** Diagram of serpentine laminating micromixer with F-shape units (a); (b) Images showing cross sections of two flows in different positions.

Another type of passive mixers are micromixers with slanted wells (ridges or grooves). These mixers are an expansion on traditional method of stream splitting for mixing enhancement. They are relatively easy to integrate within the microfluidic device and can provide additional mixing within the system without increasing the overall channel length. Stroock *et al.* [27] introduced the first with staggered herringbone grooves on the floor of the channel as shown in Figure 2-4. Staggered herringbone mixer (SHM) fabricated using soft-lithography by placing patterned grooves on the floor of a channel. The structure causes a chaotic flow by creating a repeated sequence of rotational and extensional flows. These patterned grooves allow greater mixing enhancement than the slanted wells.

In a similar study, Johnson *et al.* [28] developed a slanted groove mixer (SGM) using an excimer laser system to create a series of slanted wells on the microchannel floor to achieve quick mixing by introducing transverse transportation of the fluids. Johnson *et al.* using the four-welled structure achieved 74.7% mixing at a distance of 183  $\mu\text{m}$  past the T-junction when using a flow rate of  $0.06 \text{ cm s}^{-1}$ .

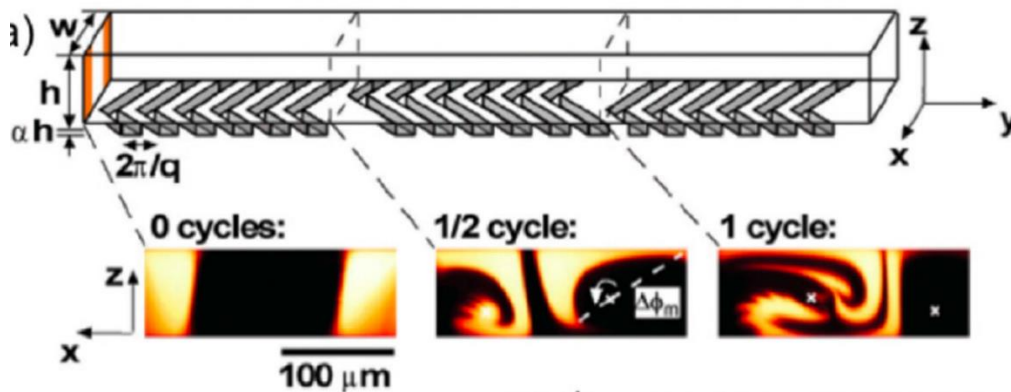


**Figure 2-4.** Schematic diagram of one-and-a-half cycles of the SHM. A mixing cycle is composed of two sequential regions of ridges; the direction of asymmetry of the herringbones switches with respect to the centerline of the channel from one region to the next. At the bottom are confocal micrographs of vertical cross sections of a channel [27].

Generally, when the grooves are deep enough, the channel length required for complete mixing drops dramatically using patterned grooves/ridges. However, these types of grooves/ridges do have a drawback, as they create dead volume within the channel.

The effect of inherent patterned ridges made by FFF method which is the subject of this study is similar to those introduced by Johnson and Stroock works. Many other different types of patterned grooves have been studied to show the effects of various micro and macro ridges or grooves on mixing enhancement in microfluidic devices [29-31]. Yun *et al.* [32] investigated the geometric effects of fabricated grooves using laser cutting and milling machines on the cross-movement of dye solutions. The results showed the effect of groove depth on the lateral transport of dye solutions. Kwak *et al.* [33] studied the mixing efficiencies of negative and positive groove patterns. Their study showed that a positive pattern has a better mixing efficiency than the conventionally used negative pattern. Computational Fluid Dynamics (CFD) models also have been used to simulate numerically the flow generated by patterned grooves [34].

One of the interesting methods for mixing enhancement is using ultra-hydrophobic surfaces for the microfluidic micromixers. Ou *et al.* introduced a passive mixer which utilizes a series of ultra-hydrophobic surfaces with oblique oriented micro ridges for mixing enhancement within microfluidic systems [35] (Figure 2-5). The used method for the enhancement works on a similar principle to micromixers described in the previous section; with this difference that a

shear-free air-water interface supported between hydrophobic micro ridges results in large slip velocities along these ultra-hydrophobic surfaces and significant reduction in drag forces by more than 40% [36].

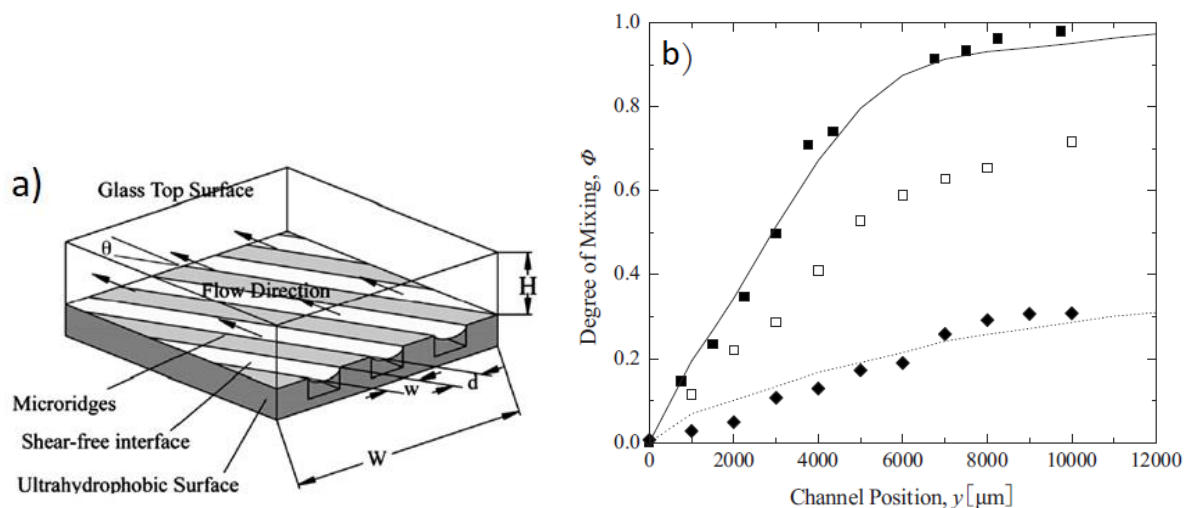


**Figure 2-5.** (a) Schematic diagram of a model for ultrahydrophobic drag reduction; (b) Improvement in the degree of mixing by hydrophobic microridges (solid squares) in comparison with hydrophilic microridges (open squares), and smooth surface (solid diamonds).

Microdroplet-based mixers are another type of passive mixers where mixing enhancement between fluids happened by using microdroplets. Microdroplets can be generated inside microfluidics using different methods such as electric fields [37], micro-injectors [38], and needles [39]. However, the most widely used methods for droplet generation rely on flow instabilities between immiscible fluids that lead to the so-called multiphase flow. For example, some researchers have created devices that produce droplets of reagents suspended in an immiscible carrier fluid (e.g., oil). Gunther *et al.* created a device that operates in a similar manner to enhance the mixing within liquid droplets [40]. In this mixer as shown in Figure 2-6, optimal mixing achieves between two miscible liquid streams by introducing a gas phase, forming a segmented gas-liquid (slug) flow, and completely separating the mixed liquid and gas streams in a planar capillary separator. The recirculation motion associated with segmented flow enhances advection in straight microchannels without requiring additional fabrication steps. The liquid was removed downstream using a capillary separator after mixing occurred in each droplet and thus the final flow from the device is a single phase. Figures 2-6 (b) and (c) show the streamlines for the recirculation in a straight channel and a winding channel,

respectively. The recirculation occurs within the plugs is highly sensitive to the initial distribution of the fluids inside the plugs. However, an optimal mixing of the fluids can be achieved by simply altering the relative flow rates of the fluids and immiscible carrier fluid to an experimentally determined value [41].

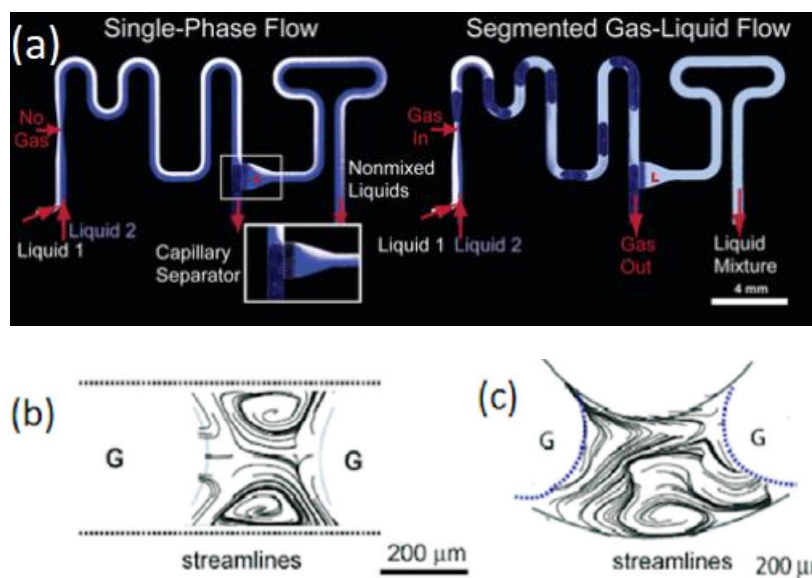


**Figure 2-6.** (a) Fluorescence micrographs of mixing between two streams. Mixing by diffusion only, no gas flow inserted (left); Mixing by using a gas stream (right). (b) Streamlines and visualization of recirculation within liquid plugs in straight channels. (c) Streamlines and visualization of recirculation within liquid plugs at the bends of winding channels.

### 2.3.2 Active Micromixers

As described previously, active micromixers rely on an external energy source for mixing enhancement. In active micromixers, external energy source is necessary; due to having movable parts which cause to be harder to fabricate than passive systems. There are a wide variety of active micromixers. They can be categorized as magnetic field driven, sound field driven, pressure field driven, thermal field driven, and electrical field driven based on using external energy sources.

Microstirrers are one of the active methods used in microfluidic micromixers. The method is similar to a magnetic stirring bar in a macroscale mixing operation. The mixing bar is literally a miniaturized version of the mixers found in chemistry laboratories. This type of active mixing enhancement uses a rotating magnetic field, which causes microbar to rotate within a fluid system, enhancing the mixing near of the bar. Multiple microbars can be used simultaneously

to enhance the mixing. The stirring microbars within the system generate circulation loops, which decrease the time needed for mixing. Lu et al. introduced one of the first mixers in the field and studied the effects of fabricated microstirrers on the mixing characteristics of fluid systems [42]. In addition to complexity of the fabrication process, the main problem associated with using microstirrers is that the mixing enhancement effect does not extend very far from the region defined by the diameter of the stirrer.

Another unique way to enhance mixing in microfluidic devices is acoustic stirring created by ultrasonic waves [43-47]. Ultrasounds are introduced into the microchannel by integrated piezoelectric ceramic transducers [43]. The ultrasonic action causes an acoustic stirring of the fluid perpendicular to the flow direction and leads to an enhancement of the mixing within the microfluidic channel. Frommelt *et al.* studied the use of surface acoustic waves (SAWs) to generate time-dependent flow patterns which enhance the mixing in microfluidic micromixer [48]. These SAWs are a type of elastic energy along the surface of the fluid, which can induce acoustic streaming through the fluid when excited. The produced streamlines cause efficient mixing within microfluidics and movement of liquid droplets even at low Reynolds numbers. In this study, acoustic waves across a solid surface are easily generated using interdigital transducers (IDTs) as shown in Figure 2-7(a). the mixing enhancement occurred by using surface acoustic waves at different frequencies (Figure 2-7(b)). Their results showed that an optimal frequency of 0.17 Hz is required to obtain the best mixing when utilizing a dual jet setup.

In a similar work, Ahmed *et al.* combined acoustic waves with a microfeature to create a fast bubble mixer within a microchannel [43]. A horseshoe shape feature was designed within a channel between two fluids, opening in the same direction as the flow direction (Figure 2-7(c)). When the fluids flowed past the horseshoe geometry, an air bubble was trapped inside the horseshoe feature due to the streamlines of the fluids. A piezoelectric transducer was used to excite the trapped bubble using acoustic waves. This caused the bubble to oscillate and send acoustic streaming through the surrounding fluid in a similar fashion to the surface acoustic waves. A homogenous and almost instantaneously mixing will be obtain when the system operates at the correct frequency (Figure 2-7(d)).

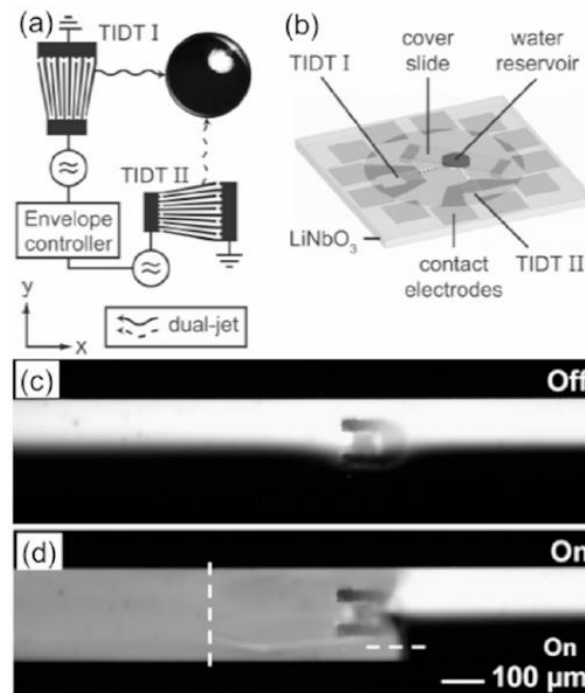


**Figure 2-7.** (a) Two tapered IDT (TIDT) exciting SAWs in x and y directions; (b) Diagram of a SAW mixer; (c) No mixing effect was observed in the absence of acoustic waves; (d) Fast mixing was achieved in the presence of acoustic waves.

One of the simple ways to achieve active mixing is to induce a pressure field disturbance. In this method instead of the traditional approach of bringing two channels together with continuous flow in each channel, the flow in one or both channels is pulsed in order to enhance mixing process at the interface between the two fluids. Generating the pulse is easily achieved by varying the voltage applied across each channel in a time-dependent manner. Since the flow is not constant, streamlines are constantly changing and there are induced changes in the flow patterns of the fluids within the system.

Glasgow et al. showed that within a simple mixing channel the best results occur when both inlets are pulsed out of phase [49]. By utilizing pulsation in both inlets, they achieved a degree of mixing 5 times greater than that without any pulsing. Flow pulsation from only one inlet also increased the degree of mixing, but not like as pulsation in two inlets. Figure 2-8 shows the numerically flow patterns that are observed at a 90° phase difference between the pulsing of both inlets [50]. In this type of micromixers, the induced perturbations inside the system cause the fluids to flow oblique to the natural flow direction. The action is similar to the patterned ridge and slanted well mixers, where the flow induces chaotic mixing within the fluid

if the control parameters are manipulated correctly. Figure 2-9 shows the experimental results obtained by Nie *et al.*, where the periodic forces used to create active mixing enhancement within microchannel [51]. The mixing enhancement achieved using a mixer with one pair of side channels. As is shown, the mixing occurs rapidly once the transverse perturbations give rise to an interfacial distortion.

Generally, implementing this type of periodic forces within microfluidics is very easy and there is no need for additional equipment or change in the fabrication process. It works well even at very low Reynolds numbers, and it is easy to manipulate its effects on the mixing within the system by simply changing the forcing parameters.

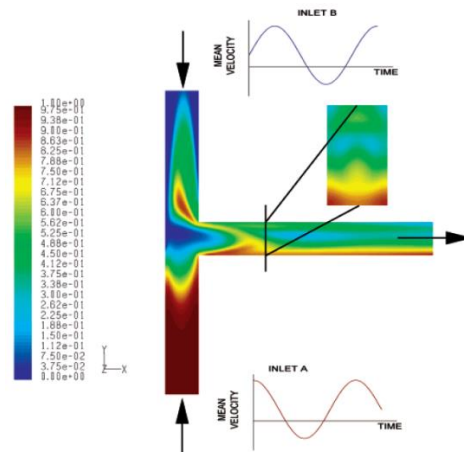


**Figure 2-8.** Pulsation is indicated by the graph next to each inlet, showing the mean velocity as a function of time. The phase difference is  $90^\circ$  between flows at two inlets. Contour plots show concentration of the liquid at half the depth of the channel and at 0.5 mm downstream of the confluence.

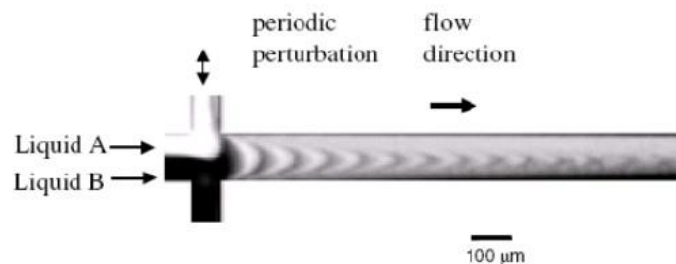


**Figure 2-9.** Experimental results of mixing by perturbed flows generated using one pair of side channels.

Thermal disturbance micromixers are another type of active mixers which rely either on the increase in the diffusion coefficient due to a temperature increase, or on natural convection to enhance the mixing in the microfluidic channel. Tsai et al. developed a device that integrates a

micropump with a thermal bubble, nozzle-diffuser, mixing channel, and a filter as shown in Figure 2-10 [52]. The device has two different inlets for the fluids to be mixed, one of the two flows passes through the chamber with thermal micropump. Subsequently, the two flows of fluid join and pass through the mixing channel having a particular meander structure with a width of 200  $\mu\text{m}$ , and a height of 50  $\mu\text{m}$ . A thermally excitable bubble is first introduced into the system between the two streams at the junction. The bubble is then excited, causing it to oscillate and enhance mixing between the two streams. At the end of the channel a filter consisting of a series of 22 micro-channels is used which is possible to separate the gas bubbles from the liquid. In general, the use of temperature within microfluidic devices seems intuitive, this area is still largely unexplored by microfluidics community. This could be partially due to the fact that temperature gradients can damage samples or change their properties.

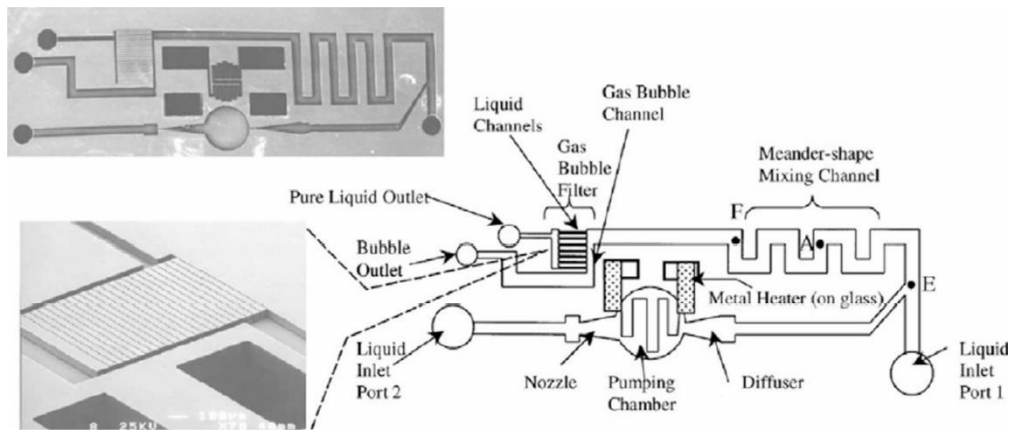


**Figure 2-10.** Schematic drawing representing components of the thermal disturbance micromixer.

Electrokinetic disturbance micromixers take advantage of fluctuating electric field to induce mixing in microfluidic mixers. The fluctuating electric fields cause rapid stretching and folding of the fluids interfaces that are able to disturb the fluid stream in highly laminar flow. This type of operation can be achieved using both DC and AC currents. Electroosmotic pumping holds multiple advantages over other micropumps, such as eliminating the need for moving parts and the creation of constant flows. They are also easy to integrate into microfluidic devices, making them ideal candidates for microfluidic micromixers. Figure 2-11 shows the device introduced by Ould El Moctar *et al.*, which is a T-shaped mixer with electrodes on the side walls [53]. The electrodes generate an electric field orthogonal to the interface plane between the fluids in the

main channel. The results revealed that by applying an appropriate voltage and frequency to the electrodes, optimal mixing can be achieved in a short time (0.1 s) and over a small length of the channel, even with a low Reynolds number of 0.02.

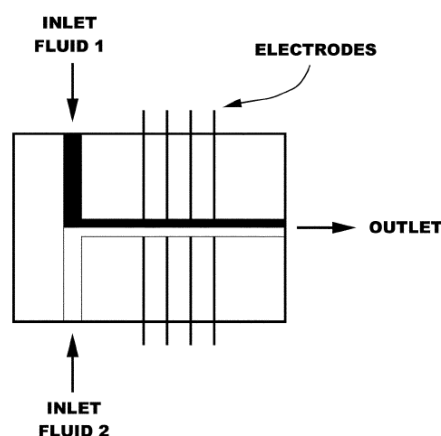


**Figure 2-11.** Configuration of the flow: the microchannel, the electrodes, and the two fluids used.

In addition to those micromixers discussed above, many other types of active mixing enhancement can be used within microfluidic devices [54]. There are also many other types of micromixers which are used the advantages of both passive and active micromixers [55]. Table 2-1 summarizes the advantages and disadvantages of passive and active micromixers with further examples of each method, and provides recommendations for their incorporation within microfluidic devices.

## 2.4 Manufacturing of Microfluidic Devices

In this section, we review current fabrication methods for microfluidic devices and look to the challenges associated with each method, and further explore opportunities with developing technologies including 3D printing as a potential replacement for rapid prototyping through soft-lithography.

The materials and methods used to fabricate microfluidic devices have generally been selected based on their functionality. Early microfluidic systems were produced from silicon even though it was quickly replaced by glass [56]. Over the 1980s, the use of silicon etching procedures, developed for microelectronics industry, allowed the manufacture of the first device containing mechanical micro-elements integrated on a silicon wafer. These new types

**Table 2-1.** Various methods of mixing enhancement in microfluidic devices [13].

Methods	Pros	Cons	Suggestions/Comments	Reference
<b>Passive micromixers</b>				
Stream splitting and recombination	Basic, but more effective than pure diffusive mixing	May require long channels for complex micromixer network	Pay careful attention to the method of recombination; adequate mixing may result without additional elements.	[57, 58]
Slanted wells or patterned grooves	Easy to fabricate (no moving parts)	Requires additional fabrication to adjust the level of mixing	Useful for mixing enhancement when precise control is not required.	[27, 34]
Hydrophobicity or surface modification	Additional mixing enhancement over other passive mixers	May be complicated to define surface modification zones	Combining with other passive mixers to maximize mixing potential	[35, 36]
Multiphase mixing enhancement	Low fabrication cost, good mixing with little sample dilution, and large mixing property change by adjusting flow rates	Requires additional purification step as immiscible carrier liquids or gas must be introduced into the device	Consider for use if introducing an additional fluid into a device is possible without hindering device operation.	[59-61]
<b>Active micromixers</b>				
Microstirrers	Versatile; excellent mixing with precise control	Difficult to fabricate (moving parts); may require multiple stirrers	Useful for applications requiring precise control over the level of mixing; magnetic actuation easier than mechanical actuation. Utilizing magnetic particles may offset some of the fabrication difficulties.	[18, 54, 62-64]
Acoustic waves	Nearly instantaneous mixing; easy to operate	Need a bubble or air interface	Consider acoustic mixers if quick mixing is needed	[48, 65, 66]
Flow pulsation	Easy to implement using micropumps or electric fields	Requires fine-tuning to achieve optimal mixing enhancement	Convenient when pumps are integrated or do not compromise operation	[55, 67]
Thermal enhancement	Simple to integrate into a device	Requires heaters	Consider thermal micromixers where heat does not affect samples/reagents	[68, 69]
Electrokinetic mixing enhancement	Can be utilized effectively at relatively low voltages. Can be very effective over short mixing lengths.	Requires integrated electrodes	Consider when electrodes are integrated into the device. Utilize ac voltages to avoid bubble formation	[70, 71]

of devices called MEMS (Micro-Electro-Mechanical-Systems) gave rise to industrial applications, particularly in the field of pressure sensors and printer heads. However, this material is not easy to handle owing to its hardness which does not make it easy to create active microfluidic components such as valves and pumps. Dangerous chemicals used during the fabrication process also require protective facilities [72]. After the initial focus on silicon, glass was the material selected to build microfluidic chips. This material is generally processed with wet/dry etching methods [72]. However, due to the difficulties with processing silicon and glass at these small dimensions have led to the introduction of polydimethylsiloxane (PDMS) and soft lithography in the late 1990s [73].

In the past two decades, the vast majority of microfluidic have been built using PDMS, especially for research and prototyping purposes [74]. The fabrication process includes the fabrication of the master mold and molding the microfluidic chip which involves substantial human labor and fabrication time can be on the order of days [75, 76]. The process of manufacturing the mold is start by transferring the CAD design to a photomask. Microchannels are “sculpted” on the mold, resulting in replicas that will enable the carving of channels into the future material of microfluidic chips as shown in Figure 2-12. First, the resin is spread on a flat surface (often a silicon wafer) with the desired thickness (which determines the height of

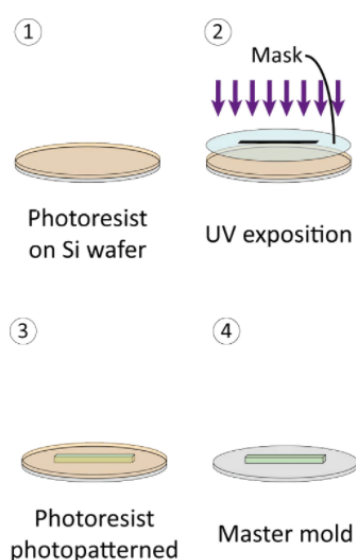


**Figure 2-12.** Schematic showing the required steps for fabrication the mold through soft-lithography.

microfluidic channels). determines the height of microfluidic channels). The resin, protected by the photomask with the microchannel pattern, is then partially exposed to UV light. The microfluidic mold is developed in a solvent that etches the areas of resin that were not exposed to UV light [77].

Figure 2-13 shows the molding steps using PDMS material. A mixture of PDMS (liquid) and cross-linking agent (to cure the PDMS) is poured into the mold and heated at a high temperature. Once the PDMS is hardened, it can be taken off the mold. Fabrication process followed by creating the inputs and outputs and bonding with glass slide to allow the injection of the fluids.

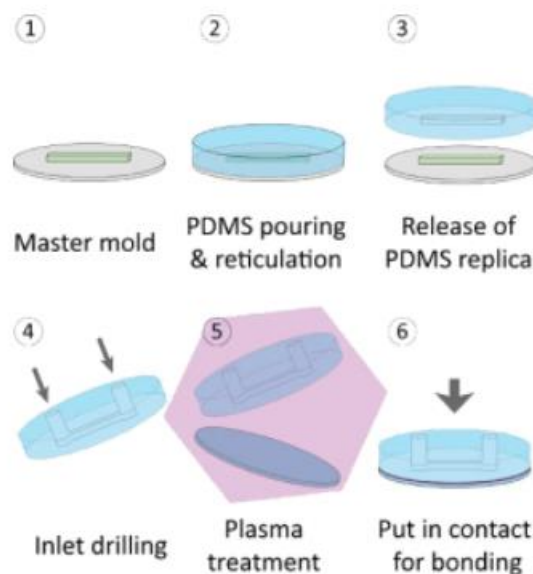


**Figure 2-13.** Schematic diagram of the fabrication process of a microfluidic device using soft-lithography.

PDMS is a transparent, biocompatible, gas-permeable, water-impermeable, deformable, and fairly inexpensive elastomer. However, three major challenges have so far hindered the commercialization of PDMS chips [75]:

1) PDMS molding (including curing, assembly, bonding, and inlet punching) is a largely manual process, being hard to fully automate – which means that fabrication is expensive and PDMS-molded devices cannot possibly meet the vision of inexpensive, batch-fabricated MEMS devices;

2) for many years, the user interfaces (inlets/outlets) of PDMS chips have consisted of punched or molded holes that are prone to leakage and are awkward to connect – as opposed to the leak-free, intuitive connectors such as the industry-standard Luer-lock, barbed connectors, etc.

3) the control systems required to run microfluidic valves (ranging from the computer, pressure sources, software, etc.), or even to connect relatively simple chips, involve engineering expertise and equipment not present in most biomedical laboratories.

#### **2.4.1 3D Printed Microfluidic Devices**

Recently, the advent of modern additive manufacturing (AM) techniques has enabled the transfer of most of the fabrication skills to 3D printers, as a potential replacement for rapid prototyping through soft-lithography due to its automated, assembly-free 3D fabrication, rapidly decreasing costs, and fast-improving resolution and throughput [78]. 3D printing does not depend on masks or molds for producing a micropattern; it only needs input from a CAD software to be able to produce a geometrically accurate 3D structure. The suite of 3D printing technologies that are practical and used in fabrication of microfluidic devices are fused filament fabrication (FFF), stereolithography (SLA), multijet modeling (MJM) or Polyjet, two photon lithography, selective laser sintering (SLS), and layered hydrospinning [79]. Among different 3D printing methods, the ones that are most relevant to microfluidic device fabrication are SLA, Polyjet, and FFF [75]. With SLA, a focused light source produces 3-D shapes in a polymer from a photoresin precursor. Generally, higher resolution has been demonstrated with SLA. Studies have shown that current printing resolution with SLA permits channels of down to approximately 20  $\mu\text{m}$  [80]. With Polyjet, an acrylic photopolymer is ejected as nanojets from a large printer head and immediately cured with UV light. With FFF, a thermoplastic polymer is fed into a nozzle and extruded onto a base, layer by layer, to form the desired 3D structure. Due to continual progress in the FFF, printing transparent, flexible, and biocompatible microfluidic devices with channel dimensions consistently under 100  $\mu\text{m}$  and as small as 40  $\mu\text{m}$  is now provided, which is done by the benefit of precisely defined printing materials [81, 82].

### 2.4.1.1 Stereolithography (SLA)

SLA was first introduced by Chuck Hull [83] and became the first commercialized 3D printing technology. The initial invention by Hull utilized only material that could be cured by UV light, but recent advances in laser technology and photochemistry of resins have enabled polymerization of photoresins with high intensity and focused LED light sources in the visible wavelength [84]. The resolution that is achievable by traditional SLA is dependent on the laser spot size and the absorption spectra of the photoresins [85].

Recently, in a developed strategy, the digital light projection (DLP) printers used to expose an entire layer of resin at once. In DLP-based printers, the resolution is determined by the size of the projected pixel. With the advent of inexpensive digital micromirror display (DMD) technology and commercially available projectors, the cost of DLP printers has come down significantly [86]. In SLA, a 3D object is built layer by layer by using selective light exposure to photo polymerize a precursor resin collected in a vat as shown in Figure 2-14. Each layer is projected as an image obtained by digitally sectioning the 3D object into thin slices. Either free surface or constrained surface approaches are used [84]. In the free surface approach (Figure 2-14), a mobile build platform is submerged in a tank of photoactive liquid polymer and resin is photopolymerized by a laser at its topmost surface that interfaces with air. In contrast, the constrained surface approach uses a mobile build platform suspended above the resin tank and the UV source, located under the tank, cures the pattern through the transparent bottom of the tank. Several groups have used SLA printer for fabrication of microfluidic devices [78, 80, 87, 88].

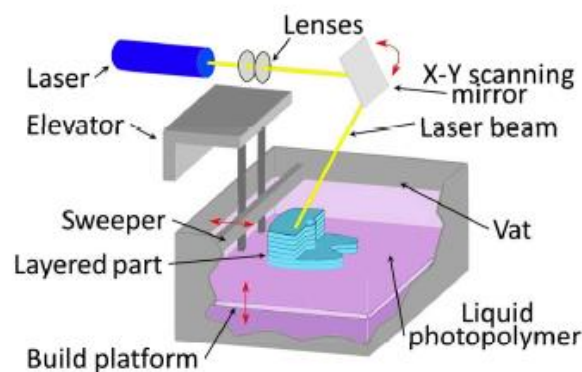


**Figure 2-14.** Schematic of the SLA printer.

### 2.4.1.2 Multi Jet Modeling (MJM) or Polyjet

In Polyjet 3D printers, as shown in Figure 2-15, each layer is built onto a tray via an inkjet head which delivers curable liquid photopolymer that is rapidly polymerized by UV. Patented in 1999 by Objet, a company later acquired by Stratasys, this printing method is also known as Photopolymer Inkjet Printing. Polyjet method is an attractive technology for microfluidic devices, because of its high resolution and multi-material printing capability. However, a sacrificial material that can be reliably cleared from an enclosed channel is key to producing arbitrary microfluidic channel networks in a single step by Polyjet method.

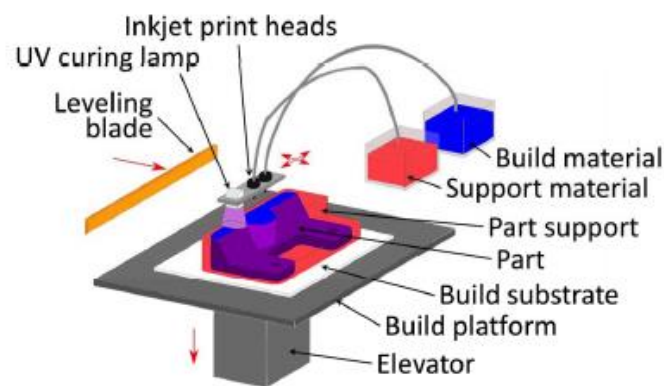


Figure 2-15. Schematic of the Polyjet printer.

### 2.4.1.3 Fused Filament Fabrication (FFF)

FFF printing was patented in 1988 by S. Scott Crump and commercialized by his company, Stratasys [89]. The process is often referred to “fused deposition modelling” (FDM). Generally, FFF-based printers use thermoplastic filaments that is unrolled from the spool as shown in Figure 2-16, the material is pushed toward an extrusion head (including one or more extrusion nozzles) and toward drive wheels, which are necessary to control the flow. The nozzle is heated to semi-cast the material, and the head can be driven both horizontally and vertically by a numerical control mechanism, following a path traced by software [90]. FFF use a wide range of cheap and biocompatible polymers like acrylonitrile butadiene styrene (ABS), poly-lactic acid (PLA), polycarbonate, polyethylene terephthalate (PET), polyamide and polystyrene. However, the main disadvantages are surface roughness, imperfect sealing between layers and toolpaths, need for support material, support removal, and long building times for massive pieces. Moreover, unlike traditional microfluidic manufacturing methods like soft lithography

that requires specialized fabrication skills and facilities, FFF is accessible and customizable to serve biology, chemistry, or pharma research and development needs [90]. Furthermore, open-source technologies enable researchers to improve the design process and reduce production for specific applications.

Microchannel fabrication with FFF has been a challenge because of lower resolution, lack of structural integrity between the layers, and opaque or translucency of the printed microfluidics. Due to continual progress being made in the development of the FFF technique, the printing of transparent microfluidic devices with channel dimensions consistently under 100  $\mu\text{m}$ , formerly exclusive to SLA, can now also be obtained with FFF [81, 82].

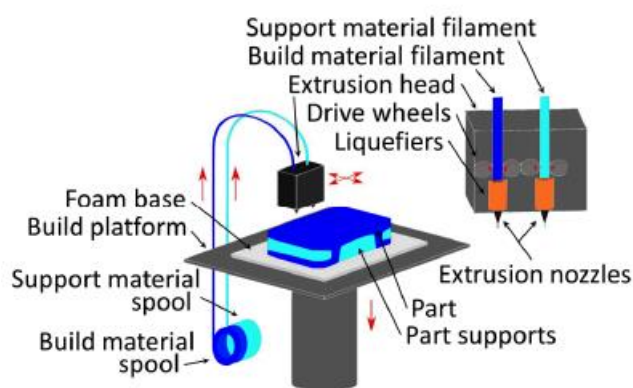


**Figure 2-16.** Schematic of the FFF printer.

#### 2.4.1.4 3D-Printing Applications in Microfluidics

In recent years, numerous research groups have been using 3D-printing techniques for the fabrication of microfluidic components. The first applications to microfluidic devices were these techniques applied for the manufacturing of the master mold in PDMS. Figure 2-17 (a), (b) shows two PDMS chips obtained thanks to molds manufactured precisely in SLA. Comina *et al.* fabricated masters for PDMS micromixers through micro-SLA [91]. During fabrication, the 3D-printed templates were rinsed in ethanol and airbrushed with a PDMS-compatible ink to protect the template surface and also allow the PDMS to cure completely. These coated templates were then used as masters for soft lithography with PDMS (Figure 2-17(a)). Chan *et al.* have developed 3D-printed masters used to fabricate 3D microfluidic PDMS networks in a one-step procedure [92]. The method to create 3D interconnected networks consists of

fabricating the master with crossovers in a parallel, basket-weaving arrangement, followed by soft lithography (Figure 2-17(b)).

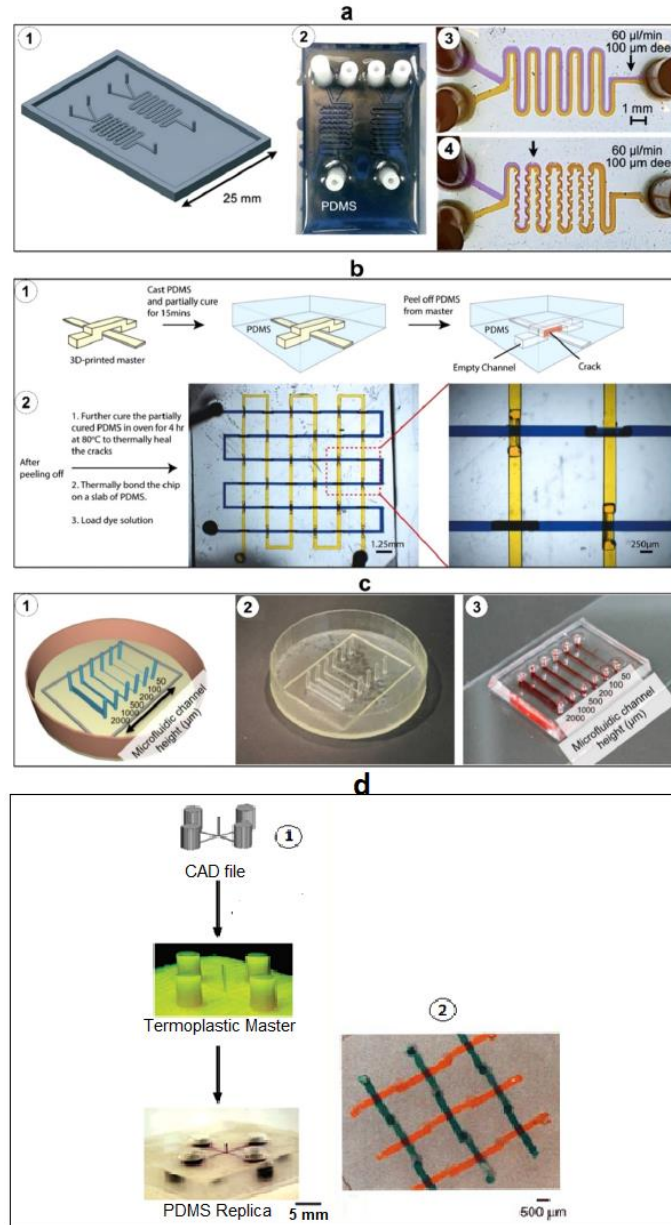


**Figure 2-17.** 3D-printed molds for PDMS microfluidic devices. **(a)** PDMS microfluidic mixer made using a 3D-printed mold; (1) 3D design of the mold for diffusion and chaotic mixers; (2) image of the cured PDMS on the 3D-printed mold; Result of the tests conducted on two mixers using yellow and purple fluids: it is possible to observe diffusion phenomena (3) and chaotic motions (4). **(b)** Basket-woven PDMS crossover feature fabricated using a 3D-printed mold; (1) schematic of the fabrication process for crossover features; (2) image of PDMS crossover features loaded with yellow and blue fluids. **(c)** PDMS channels made using a Polyjet printed mold; (1) design of the microfluidic channels with different heights; (2) 3D-printed mold; (3) PDMS microfluidic device. **(d)** Basket wave PDMS crossover feature fabricated using a FFF-printed mold; (1) schematic of the fabrication process for crossing features; (2) Basket wave for crossing, nonintersecting channels.

Kamei et al. investigated the use of a Polyjet printed mold to be filled by PDMS, which resulting chip was used for examining concentration gradients for biomedical applications [93]. Figure 2-17(c) shows the master and the related PDMS device used for the study of the survival and growth of embryonic stem cells. One of the first examples related to FFF is shown in Figure 2-17(d), where an FFF machine is used for rapid tooling to manufacture microfluidic devices in PDMS, with a reported 250  $\mu\text{m}$  resolution [94]. Since this initial result, the variety of extrudable materials has notably increased, leading to increasing opportunities for research.

With continues progress in 3D printing techniques, these methods are now used for fabricating integrated microfluidic devices. Lee *et al.* have introduced a LoC manufactured in SLA that has a helical microchannel with a trapezoidal cross-section [95]. The purpose of this chip is to capture pathogenic bacteria. The chip contains two inlets, one is dedicated to inserting the sample and the other for injecting clusters of magnetic nanoparticles (Figure 2-18). The latter have the purpose of binding to the pathogens contained in the sample in order to filter it. In particular, tests were carried out on a sample of milk to separate the bacterium *Escherichia Coli*.

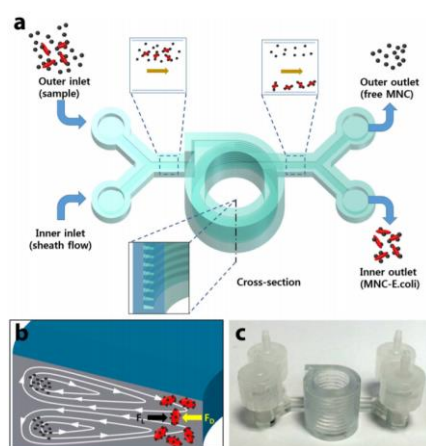


**Figure 2-18.** Microfluidic device made by SLA a) Schematic illustration of the separation process. b) Illustration of Dean vortices in a trapezoidal cross-section of the channel. c) Image of fabricated device.

Other important components in microfluidics are connectors [96], microvalves, and micropumps [97, 98], especially when the subject is wearable sensors. On-chip integrated microvalves and micropumps are critical components to control fluid flow in microfluidic devices and are important elements in automation. The first demonstration of 3D printed valves

was shown in 2015 by Nordin group [97], closely followed by the Folch group [98]. In both cases the valves were 2 and 3mm diameter and 10 mm diameter, respectively. Folch group showed fabrication of 3D-printed microfluidic valves and pumps using a SLA 3D printer with clear biocompatible resin. Each valve has one input and one output and may be operated via a pneumatic control line. The valves (Figure 2-19(a)) may also be combined in parallel or in series to form switches (Figure 2-19(b)) and pumps (Figure 2-19(c)), respectively. Recently, Nordin group demonstrated high resolution 3D printing microchannels (18\*20  $\mu\text{m}$ ) [80] and microfluidics components with a high degree of integration, including 15  $\mu\text{m}$   $\times$  15  $\mu\text{m}$  valves [99]. Their results enable highly functional and compact microfluidic devices for a wide variety of biomolecular applications.

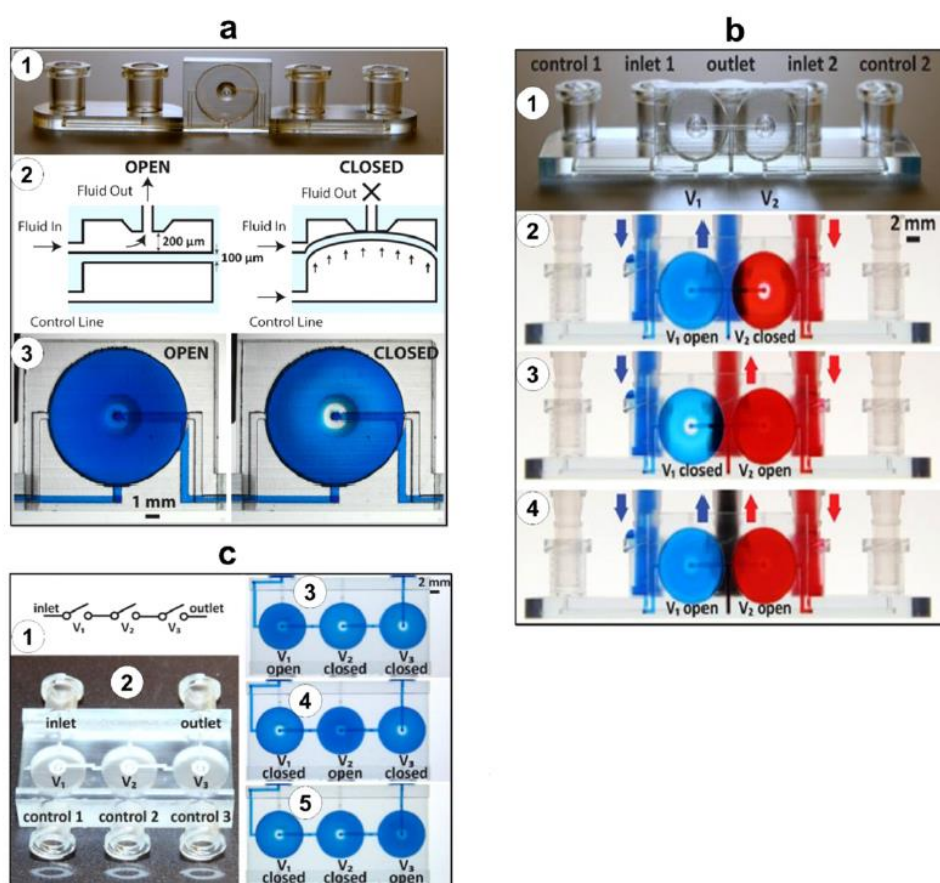


**Figure 2-19.** 3D-printed microfluidic components. (a) Basic 3D-printed valve design; (1) image of the single-valve device; (2) schematics and (3) images of the valve in its open and closed states. (b) 3D-printed two-valve switch (two parallel valves); (1) image of the two-valve switch; (2)–(4) photographs of the switch in three different actuation states. (c) 3D-printed micropump (three valves in series); (1) fluidic circuit diagram of the pump system; (2) image of the pump; (3) image of the pump in three different phases of the actuation sequence.

Reactors are other important devices for chemical syntheses can be manufactured in a few hours, thus producing reliable and robust reactors at low costs and utilizing well-defined materials, a main advantage of FFF in comparison to SLA technologies. Kitson *et al.* described a 3D-printed micro/millifluidic reactionware with a low-cost material and fabrication technique [100]. The authors proposed three micro-scale reactors with one inlet, two inlets (volume of 60  $\mu\text{l}$ ), and three inlets (volume of 270  $\mu\text{l}$ ) (Figure 2-20).

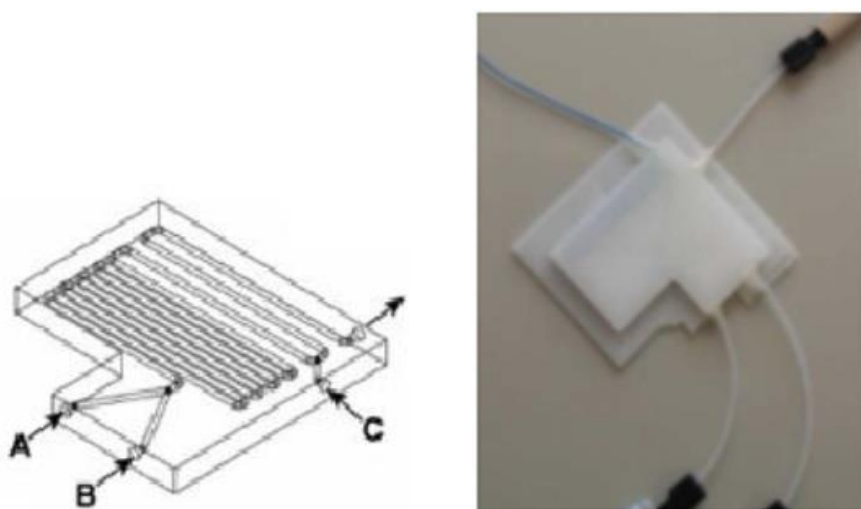


**Figure 2-20.** 3D-printed reactionware; (left) design of a three-inlet reactionware device; (right) image of the 3D-printed three-inlet reactionware used in the polyoxometalate syntheses.

Several factors have limited the use of FDM for microfluidic applications. Resolution is limited by the nozzle diameter and drive system, and structures are often opaque or translucent due to the scattering of light at the interface of the extrusion lines. There are several active groups that are working on the FFF limitations in microfluidics [81, 82, 101]. Gale Group have introduced high pressure, heat resistant, transparent microfluidics with FFF by the benefit of precisely defined printing materials [82]. In these studies, different types of materials were used such as: In-PLA, t-GLASE PETg (polyethylene terephthalate glycol), Nylon-680, PLA Crystal Clear and PETg XT. T-shape serpentine micromixer was created, characterized by  $400 \times 400 \mu\text{m}$  channels with 41 turns (Figure 2-21). In this work, leak free, efficient mixing was readily obtained within the 3D printed serpentine mixer (Figure 2-21). Printing of well defined, debris free channels was simple and easily reproducible.

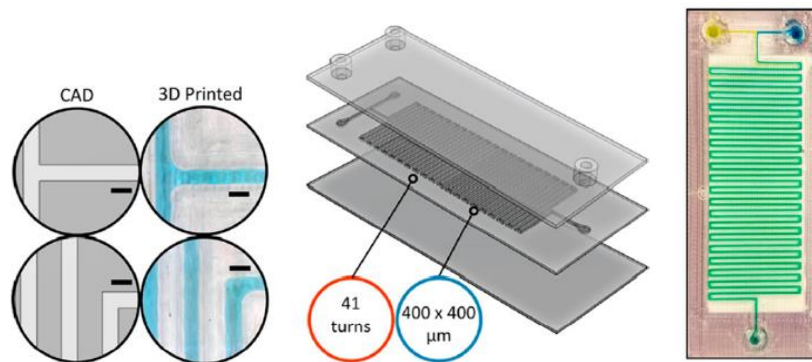


**Figure 2-21.** Left: CAD designed versus 3D printed channels. Middle: One-step 3D printed serpentine mixer. Right: Image of yellow and blue dye mixing within the serpentine device.

By introducing thermoplastic polyurethane (TPU) as a new material for 3D-printed microfluidics, Gale group demonstrated that TPU exhibits same properties that have made PDMS historically attractive. They demonstrated that channels in the true microfluidic regime ( $<100 \mu\text{m}$ ) can be achieved with cheap ( $<\$1000$ ) FFF printers when given the appropriate slicing parameters (Figure 2-22).

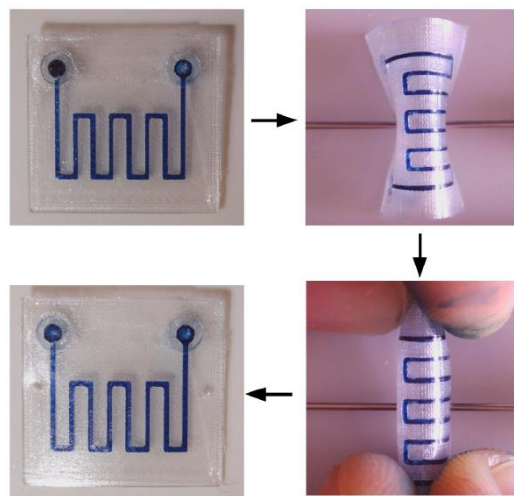


**Figure 2-22.** 3D printed TPU microfluidic device, demonstrating transparency and bending capabilities of 3D printed TPU.

## 2.5 Microfluidics for Lysis and DNA Extraction

Microfluidic devices are attractive tool for various bioengineering applications. Microfluidics as a technology that can manipulate and control fluids at micron or submicron dimensions due to having the characteristics of miniaturization, integration, low energy consumption and rapid

analysis, has become attractive tool in cell biological research. As a present example, COVID-19 tests – which have proven to be central to controlling the pandemic – are a form of miniaturized technology. Many COVID-19 tests can give results within hours without the need to send a sample to a lab, and most of these tests use an approach called microfluidics.

Deoxyribonucleic acid (DNA) and ribonucleic acid (RNA) analysis is important for detecting diseases, mutations, and determining whether a patient carries a genetic disorder or has a certain gene, or even to perform a paternity test using DNA analysis. There are several fundamental techniques used for DNA analysis including detection, amplification (polymerase chain reaction or PCR), and separation. There is a continuous search for more efficient ways to perform these and other key steps in DNA analysis. Nucleic acid extraction is one of the essential steps required in the workflow of genetic analyses. Many steps can now be carried out in microfluidic devices. Microfluidics has the potential to make DNA extraction faster, more efficient, less expensive, and more accurate [1].

The common methods of extraction of DNA include electrophoresis [102], high salt precipitation [103], spin column [104], and magnetic beads [105], etc. one of those common methods is using magnetic beads for binding the nucleic acid molecules which are then separated from other non-targeted substances under the influence of magnetic field. In the manual method all the steps are carry out by operator. However, there are also some commercial devices which automated the process by help of robotic handling. Figure 2-23 show the required steps for DNA extraction using testing tubes. The magnet particles are added to the cell lysate to bind the target molecules. After binding DNA, an external magnetic field attracts the beads to the outer edge of the containing tube, immobilizing them. While the beads are immobilized, the bead-bound DNA is retained during the washing steps. Adding elution buffer, and removing the magnetic field then releases the DNA as a purified sample, ready for quantitation and analysis.

Before the extraction process, there is a need to break the cell membranes; a process which is called cell Lysis. Cells are the fundamental unit of all living organisms. The genetic information for the development and functioning of any organism is encoded in their DNA or RNA sequences that are located inside the cell [106]. Every cell has an outer boundary called

a cell membrane, which serves as a barrier and regulates the transport across the cellular membrane of material between the inside and the outside of the cell. It anchors the cytoskeleton to provide shape for the cell and attaches to other cells to help form tissues. The cell membrane is mainly composed of lipid (50%), protein (42%) and saccharide (2%–8%) [107]. As for the configuration, a phospholipid double-layer, with the hydrophilic "head" regions facing outside and the hydrophobic "tail" regions inside, with embedded glycoproteins composes its general frame, which can be schematized as a two-dimensional fluid, as shown in Figure 2-24.

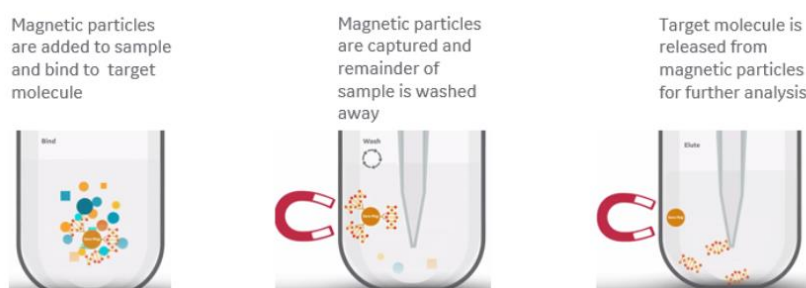


**Figure 2-23.** Overview of magnetic bead-based DNA extraction.

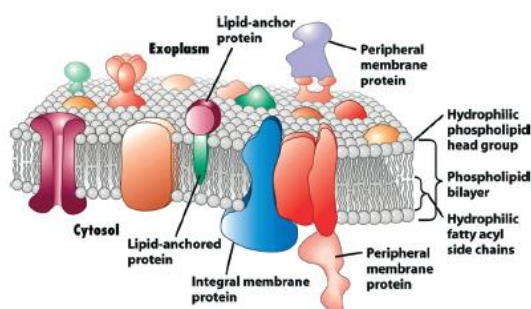


**Figure 2-24.** Schematic model of the cell membrane [108].

The cell lysis plays a crucial role in obtaining intracellular components, whose quality will directly influence the subsequent extraction and analysis. The requirements for a device to perform cell lysis include speed (to prevent further biochemical changes), selectivity (to disrupt cell membranes while protecting organellar membranes), and integration (to combine with other devices). There are few studies in which microfluidic devices are used for cell lysis and DNA extraction operations in one single chip. The most microfluidic devices in this field, focused on extraction process. The conventional cell lysis is performed by large devices which are hard to move and be integrated with subsequent analysis devices.

For cell lysis, microfluidics can not only miniaturize the devices, but also supply a relatively closed environment, which will defend cells against outer pollution. Among different methods for cell lysis, chemical, mechanical, electroporation, laser and thermal methods are more usable inside microfluidics. In the following, we will focus on the different cell lysis methods utilized in microfluidics for cell analysis.

### 2.5.1 Chemical lysis

Chemical methods use a lysis buffer containing surfactants to solubilize lipids and proteins in the membrane, which creates pores within the membrane and eventually leads to full lysis. Chemical lysis can be classified as alkaline and detergent (surfactant) lysis. In the first type, OH-ions are the main component utilized for lysing target cells. The method is suitable for all kinds of cells, the process is however very slow. The second type of chemical lysis utilizes surfactants to disrupt the cell membrane. Detergents are most widely employed for lysing mammalian cells. Figure 2-25 shows a generalized schematic of the chemical lysis. In general, separate inlets (one for the sample flow and one for the detergent agent) with one or two syringe pumps and a common outlet are necessary. A reaction chamber may be useful to visualize and measure the lysis efficiency better. Although chemical lysis is simple to implement and needs only mixing for activation, it also has some drawbacks. For example, the chemical reagent in lysis buffer will inhibit subsequent extraction and amplification, so must be removed or filtered out. Then the additional separation steps will increase the complexity for microfluidic system integration.

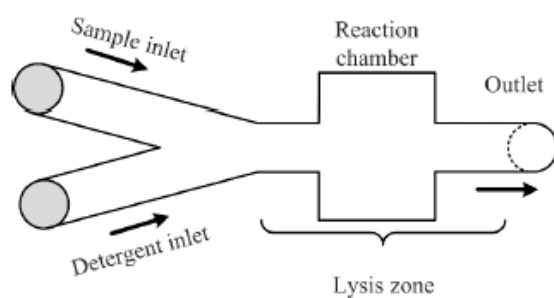


**Figure 2-25.** Schematic representation of a microfluidic device for chemical lysis method.

## 2.5.2 Mechanical lysis

Mechanical lysis is done by tearing or puncturing cell membranes using mechanical forces, which include shear stress, friction forces and compressive stress. It involves directly damaging the cell structure to release the required intracellular components. Normally, sharp nanostructures (nano-knives), ultra-sharp nano-blade arrays, ... are added that can concentrate and amplify friction forces and shearing stresses to penetrate the cell membrane. Figure 2-26 shows a generalized schematic of the method. Here, one inlet with one syringe pump is enough, as there are no other fluids needed for the process, except for the sample.

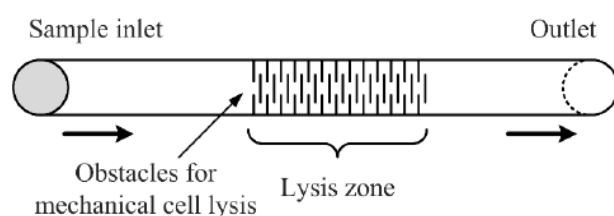


**Figure 2-26.** Schematic representation of a microfluidic device for mechanical lysis method.

It is known that just subjecting cells to shear and frictional forces induced by entering contractions may not be enough to rupture membranes. As shown in Figure 2-27, Dino Di Carlo *et al.* developed a mechanical lysis device integrated with additional sharp nanostructures in the channels, concentrating and amplifying friction forces to penetrate the cell membrane [109]. Mechanical lysis can relatively minimize the protein damage, which frequently occurs in chemical lysis, thermal heating and electrical shock. However, it requires additional instrumentation or operation for activation.

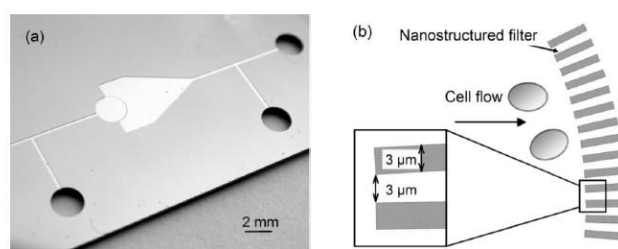


**Figure 2-27.** Schematic of the device with nanoscale barbs and a detailed view of the lysis region. The region consists of a semicircular nanostructured filter with 3 μm wide, 20 μm deep posts, with a sudden expansion after the filter to reduce the speed of the cell debris for observation.

### 2.5.3 Electroporation lysis

Electroporation is a common method for creating transient pores in cell membranes to release genetic material or small molecules. Figure 2-28 shows a generalized schematic of an electroporation microfluidic device for cell lysis. When cells are exposed to an external electric field, there is a potential created across the cell membrane, known as the transmembrane potential (TMP). Once the potential exceeds a certain threshold,  $\sim 0.2\text{--}1.0$  V, pores will form in the cell membrane to release intracellular components. If the electric field is not high enough, the pores will be resealed shortly after removing the electric field, which can minimize the induced cell damage. However, if the electric field is too high, irreversible mechanical breakdown of the cell membrane will happen, which leads to the complete lysis of cells.

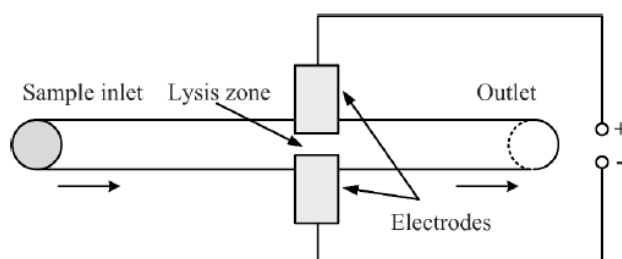


**Figure 2-28.** Schematic representation of a microfluidic device for electrical lysis method.

Normally, the most obvious choice for electroporation is to use a direct current (DC) electric field because the cell membrane will experience the largest TMP while the subcellular organelles will experience none. However, it will produce a voltage exceeding the water electrolysis threshold of  $\sim 1.3$  V, which may inevitably create gas bubbles and extreme pH conditions near the electrodes. For this reason, *Ziv et al.* investigated the use of alternating current (AC) electric field for lysis in order to avoid electrolytic gas bubble formation [110]. They used symmetric AC square waves of different amplitudes and frequencies to study the influence of AC on gas bubble formation, and finally reached the conclusion that at frequencies higher than 0.15 Hz there is no bubble formation at any flow rate. The problem of gas bubbles can also be solved by a microfluidic chip with polyelectrolytic salt bridges [111], as shown in Figure 2-29. A pair of plugs on both sides of the microchannel separate the cell suspension and a hypertonic solution. The ionic flux completes the electric circuit from an external electrode

to the other electrode. The chip was designed to have low impedance so that a large portion of the potential difference was exerted on the cell flux, achieving a sufficiently high electric field gradient by a small DC bias and avoiding which avoids gas bubble formation.

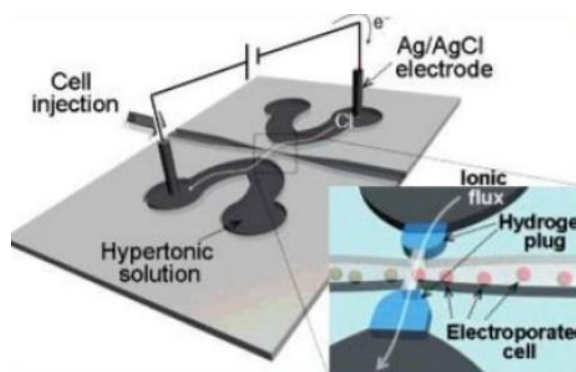


**Figure 2-29.** Schematics of the low-voltage DC micro-electroporation chip. The hydrogel plugs on both sides of the microchannel act as salt bridges to substantially reduce the potential gradient.

Electroporation lysis has a lot of advantages, such as the ultra-high lysing efficiency (the whole lysis process can be completed on a millisecond level), and the selectivity for membranes (the cell membrane is completely lysed, while organellar membranes are undamaged). However, there are also some drawbacks. For example, it demands an exact value of the applied electrical signal, which requires a relatively complex operation process. The short working life of the electrodes also affects the practical applications of this method. Additionally, the electrophoresis separation, which often follows the electroporation lysis, makes continuous injection difficult.

#### 2.5.4 Laser lysis

Laser lysis involves utilization of the fluid motion produced by a focused laser to break the cell membrane. When the laser pulse is focused at the buffer interface of a cell solution, it will produce a localized cavitation bubble. The expansion and collapse of the bubble can generate a shock wave, which helps rupture the cell membrane together with the induced fluid dynamic forces (Figure 2-30). Because of its selectivity, Laser lysis due to its high efficiency (on a microsecond level) has become a good choice for assays that require high temporal resolution, and the localization of the lysis region makes it particularly suitable for analysis of settled cell suspensions. On the contrary, the limitations of this method are also very obvious. For example,

the parallel processing and integration of the optical system is quite complex, and the equipment required, such as a YAG laser and a CCD camera, is expensive.

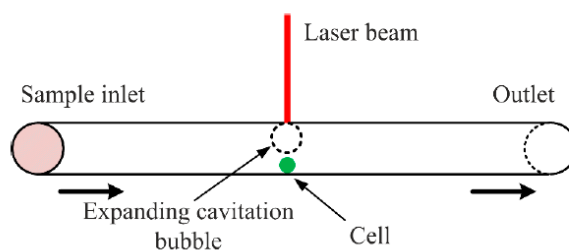


**Figure 2-30.** Schematic representation of the laser lysis in microfluidics.

### 2.5.5 Thermal lysis

Thermal lysis involves the use of high temperature to denature the proteins within cell membranes, thus damaging the cells to access intracellular components. Figure 2-31 shows a schematic generalization of the method. Most conventional thermal lysis methods are performed by ohmic heating, which consumes low power and is easily miniaturized. Lee *et al.* reported an automated microfluidic system for DNA amplification, as shown in Figure 2-32 [112]. It uses micro-heaters and micro-temperature sensors to regulate the temperature inside the lysis chamber and meanwhile gives a real-time measurement. Based on this configuration, cells can be lysed within 2 min at a constant temperature of 95 °C.

In addition to ohmic heating, induction heating can also be used for cell lysis which has advantages of simple fabrication and high lysing percentage. Baek *et al.* [113] presented a microfluidic system to perform wireless thermal lysis, as shown in Figure 2-33. After comparing different materials and frame widths, a nickel structure was selected different

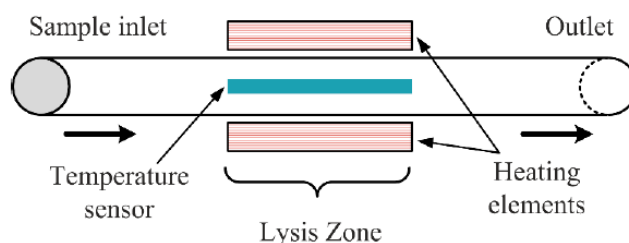


**Figure 2-31.** Schematic representation of a microfluidic device for thermal lysis method.

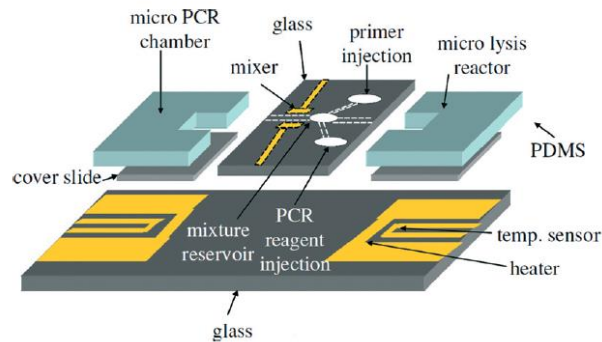


**Figure 2-32.** Schematic representation of the integrated microfluidic system. The microelectrodes deposited on the lower substrate act as driving elements, while the ones on the shielding channel are for mixing of samples.

materials different materials and frame widths, a nickel structure was selected as the heating element because of its faster thermal response and relatively small geometric influence. Using an alternating magnetic field produced by an induction coil, cells can be rapidly lysed by wireless induction heating.

Thermal lysis is one of the earliest used techniques. Its high lysing intensity and simplicity have made it well established in many laboratory settings, including the Southern Blot and polymerase chain reaction (PCR). However, the resulting thermal damage to proteins also seriously restricts its application in immunodetection.

There are also other lysis methods which are hard to categorize. However, it is not easy to say which mechanism is better, since each of them has its own merits. A comparison of these major groups is summarized in Table 2-2 in terms of four different aspects: lysing efficiency (reflected by the lysing time), lysing percentage (reflected by the number of broken cells), technique difficulty (reflected by the fabrication and operation complexity), and cost (reflected by the price of the required instruments). For example, laser lysis is the most suitable for suspension cells, while mechanical lysis can do the least harm to proteins. Thus, one can choose the right method for a specific application according to its characteristics as indicate in Table 2-2. Selection a suitable method for lab on chip application can be also more complex. It should be noted that most of the previously fabricated microfluidic devices for cell lysis are standalone units. To make them practical in point-of-care applications, integrating the cell lysis microfluidic part with other function blocks to make a complete diagnostic system is no doubt

of great importance and will be the trend of lab-on-a-chip research. The challenges raised from integration include the structural complexity and process compatibility.

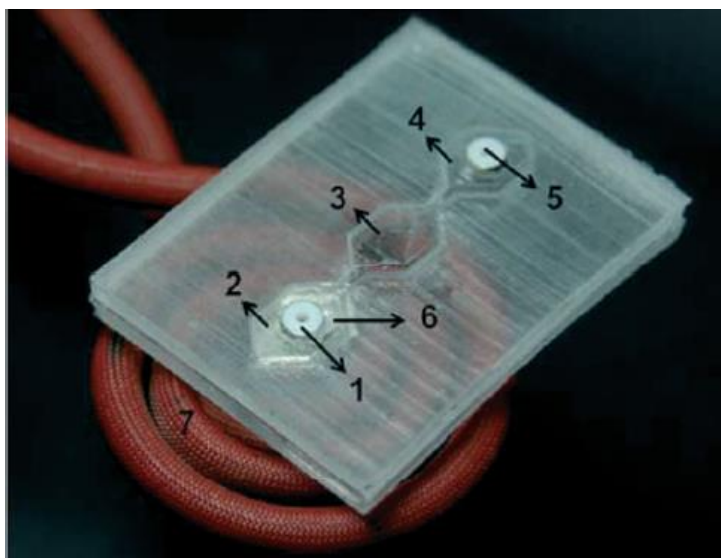


**Figure 2-33.** Photograph of the microfluidic induction heating system. A metal heating unit with a hexagonal shape 6 mm long and 100  $\mu\text{m}$  thick is embedded in the bottom layer of PDMS.

**Table 2-2.** Comparison of different cell lysis methods [107].

Lysis method	Efficiency	Lysing percentage	Technical difficulty	Cost	Brief comments
Chemical	+	++++	+	+	Simple and convenient, reagent residue must be removed.
Mechanical	++	+++	+++	++	Harmless to proteins, additional operation required.
Electroporation	++++	++++	+++	+++	Most widely used, accurate regulation of voltage required.
Laser	+++++	+++	++++	+++++	Highly efficient, complex and expensive system.
Thermal	++	++++	++	++	One of the earliest methods, causes damage to proteins.

# **Chapter 3 :**

# **Materials and Methods**

### **3.1 Introduction**

Fused Filament Fabrication (FFF) is a technique where the filament is heated and deposited layer by layer based on the generated section data from a CAD model. Different studies have demonstrated the effect of FFF printing parameters on mechanical properties of printed parts. In this section, first, we introduce different printing parameters affecting on surface roughness of the microchannels. The materials and methods for studying the effect of these parameters on fluidic behavior in microfluidic micromixers are described. A colorimetric approach is introduced for measuring the performance of the printed devices in mixing two fluids by using images taken from the microchannels. In the next step, a microfluidic chip is designed for the lysis and DNA extraction.

### **3.2 FFF-Printing Parameters Affecting on Fluidic Behavior**

In the literature, several factors have been noted that can be used to model the surface profile and the resulting surface roughness in the printing process, such as the cross-sectional shape of the deposited filaments, line width (raster or road width), infill orientation (raster angle), and layer thickness [114]. Additionally, the overlap distance between adjacent layers and the distance between adjacent filaments, which exist in the vertical and horizontal directions, can act as important parameters for the surface roughness of printed devices. The process parameters are shown graphically in Figure 3-1, and defined as follows:

- (a) Line width (LW) refers to the width of the filament deposited by the extruder and depends on nozzle tip size.
- (b) Infill orientation ( $\theta$ ) refers to the angle of the deposited lines with respect to the X axis on the bottom part layer. The typical allowed infill orientations are from  $0^\circ$  to  $90^\circ$ .
- (c) Layer thickness ( $h_1$ ) is the thickness of layer deposited by nozzle tip and depends on the material and nozzle tip size.
- (d) Air gap (b) refers to the distance between adjacent filaments on the same layer (Figure 3-1b). There is another gap between two adjacent layers in the vertical direction (Figure 3-1a).

There are various studies that studied the effect of these parameters on the mechanical properties and surface quality of the printed part [114-117]. However, there are limited works that have used the effect of the inherent and unique features of FFF process on the fluidic behavior in printed microfluidics. Li *et al.* [118] used the extrusion orientation for enhancing mixing behavior in microfluidic chips made by FFF method. As shown in Figure 3-2, FFF printed chips with an extrusion orientation of  $60^\circ$  relative to the fluid flow showed the highest mixing efficiency at all flow rates. The printed chips with extruded filament perpendicular to the flow ( $90^\circ$ ) showed slightly better mixing than printed chips with extruded filament parallel to the flow direction ( $0^\circ$ ); but the mixing efficiency in both of these directions is less than  $30^\circ$  and  $60^\circ$  angles.

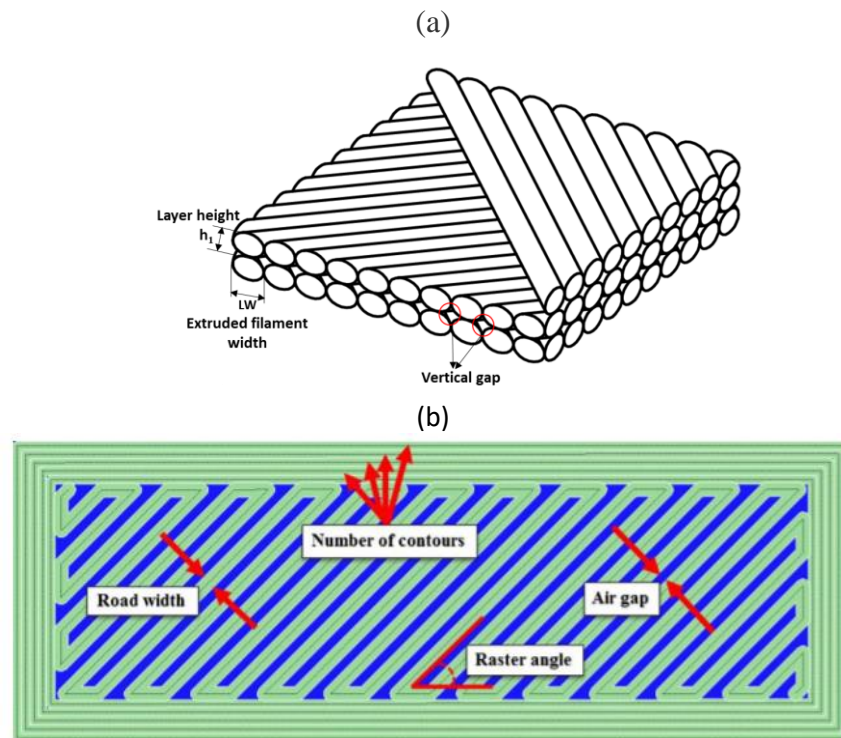


**Figure 3-1.** Schematic showing the main FFF printing parameters

Several studies have demonstrated the effect of adding micro/macro geometrical features on fluidic behavior in microchannels which discussed in chapter 2 [27, 28, 30, 31, 33, 34, 119]. In this research, the inherent characteristics of the FFF method such as presence of surface roughness due to the nature of the process are investigated on the mixing efficiency within microfluidic micromixers. The inherent properties of FFF in creating positive ridges patterns and therefore, enhancing mixing performance are investigated. Thanks to the popularity of

surface patterning for creating of passive micromixers, FFF method can be a simple and effective way to fabricate micromixers. In the following, we will describe in detail the methods and materials used in this study, which are summarized in the following steps:

- Design and fabrication of the micromixers
- Numerical simulation
- Colorimetric analysis

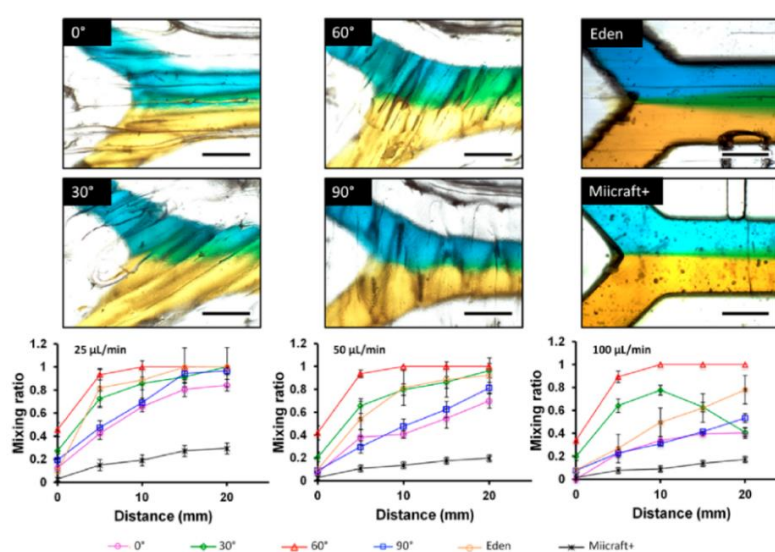


**Figure 3-2.** Performance of mixing in a Y-shape micromixer (main channel  $750 \mu\text{m} \times 500 \mu\text{m}$ ) with different extrusion angles, visualized with yellow and blue food dye at  $25 \mu\text{L min}^{-1}$  for FFF  $0^\circ$ ,  $30^\circ$ ,  $60^\circ$ , and  $90^\circ$ , Polyjet, and SLA, respectively. Plots of distance vs. mixing ratio, demonstrating diffusion through the laminar flow channel at 25, 50, and  $100 \mu\text{L min}^{-1}$  are also shown below the microscopic images [118].

### 3.2.1 Design and Fabrication of the Micromixers

A simple Y-shaped micromixer with two inlets and a single outlet is used for the study of process parameters on fluidic behavior, with schematic shown in Figure 3-3. The device is equipped with two inlets ( $600 \mu\text{m} \times 600 \mu\text{m}$ ), which merge into a single channel. The mixing channel is 52 mm long (from the Y-junction); the width and height of the main channel are  $900 \mu\text{m}$  and  $600 \mu\text{m}$ , respectively. The Schematic diagram of the main channel with the paths of the print head is shown in Figure 3-4b, c. The paths of print head on the bottom channel are the effect of extruded filaments, where the heated filaments deposited layer by layer and form the object based on predefined paths of the print head. The paths of extruded filament are like a set

of obliquely oriented ridges, which named patterned ridges in this study. The cross-section of the extruded filament is nearly elliptic shaped (Figure 3-4a). The geometry of the patterned ridges in the FFF process is determined by the width of infill filament ( $LW$ ), filament height or layer thickness ( $h_1$ ), infill orientation ( $\theta$ ), and distance between adjacent filaments ( $b$ ) which is called air gap (Figure 3-4c). The ridge period ( $\lambda$ ) will be the sum of the extruded width and air gap.

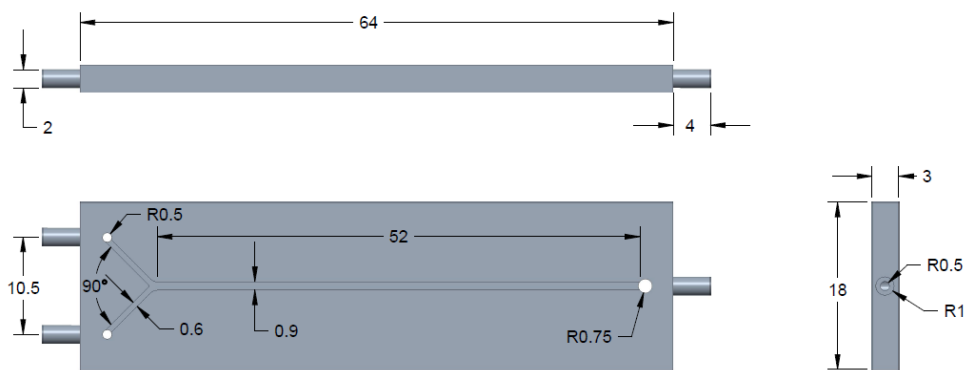


**Figure 3-3.** CAD illustrations of the micromixer design with dimensions in mm.

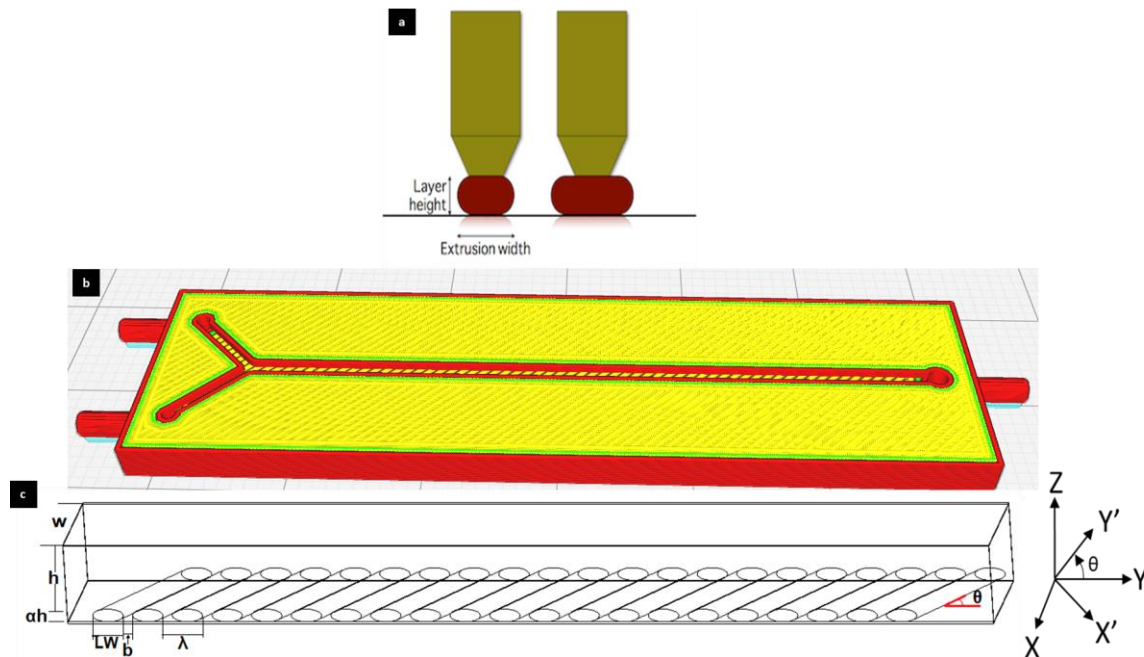


**Figure 3-4.** Printing parameters. (a) The geometry of extruded filament; (b) Show the movement path of printing nozzle; (c) Schematic diagram of fabricated channel with obliquely oriented ridges. The coordinate systems ( $x, y, z$ ) and ( $x', y', z'$ ) define the principal axes of the channel and of the ridges.  $LW$  is the width of extruded filaments, air gap ( $b$ ) is horizontal distance between two adjacent filaments, and  $\lambda$  is ridge period. The angle  $\theta$  denotes the orientation of the ridges relative to the fluid flow in the channel. The ridge height ratio is proportional to the ridge height ( $h_1$ ) to channel height ( $h$ ) ratio.

To study the effect of the different patterned ridges made by FFF on the fluidic behavior, a set of devices are printed with different values of the parameters adjusted in the slicing software. The considered parameters and their values, which are a representative of the fine and rough surfaces in FFF are selected so that no leakage would occur inside the printed devices. Therefore first, for each single parameter, different levels are considered with fixing other parameters; and the printed devices are tested in case of leaking. Then, a design of experiments is done to study the main and interaction effects of the process parameters as well as the effect of printer and material on the mixing process.

The functionality of the micromixers made by FFF method are compared with Polyjet and SLA methods in terms of mixing performance and limitations of the different fabrication platforms. The performance will be assessed in terms of completeness of mixing, channel length, and related fabrication process. For this purpose, a classical Y-shaped serpentine channel is used and fabricated with different 3D printing methods as shown in Figure 3-5. The designed unibody micromixer is a passive micromixer, where the mixing enhancement is achieved by altering the structure or configuration of fluid channels. The main elements of the devices are:

- (i) inlets: the input connectors. The device was equipped with two inlets to allow two different flows to join in the serpentine.
- (ii) (ii) main channel: a serpentine-like channel, 600  $\mu\text{m}$  wide and 600  $\mu\text{m}$  high, consisting of 18 turns.
- (iii) (iii) outlet: the output connector, of the same size as the inlets.

Three different processes are exploited to fabricate unibody micromixers: (i) Polyjet, (ii) SLA, (iii) FFF. Details and parameters of process are reported in Table 3-1. After designing 3D models of the micromixer, the CAD files are converted to STL format and then imported to relevant slicer software (see section 3.2.1.3) for setting the printing parameters and slicing .stl files into G-code.

To evaluate the influence of the printing parameters on mixing performance, different devices are printed with setting various values for the parameters. As previously explained, the geometry of the ridges in the FFF method is determined by the width of infill filament (LW),

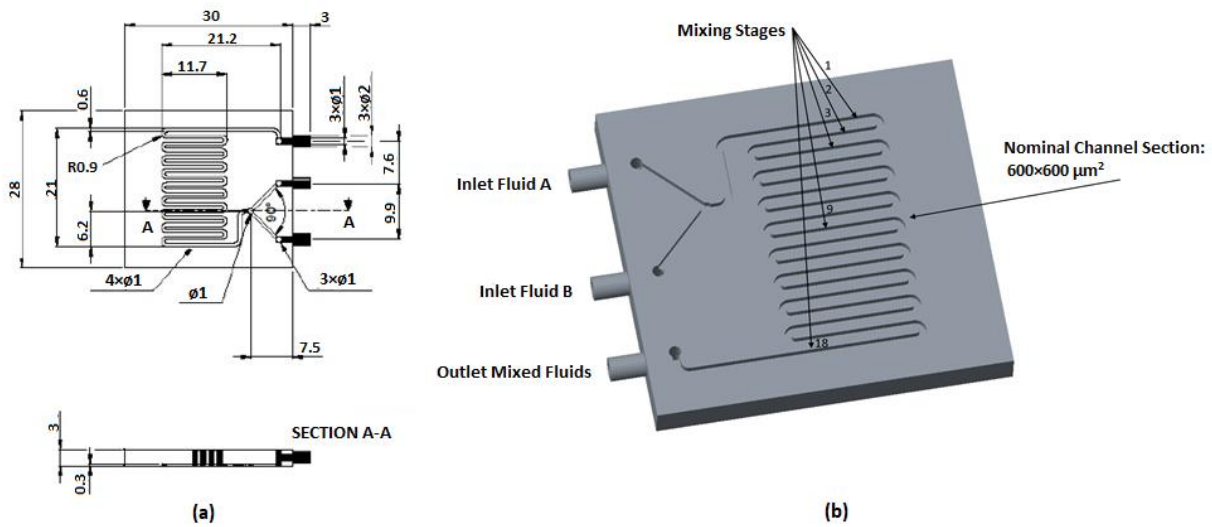


**Figure 3-5.** (a) CAD drawing of the designed micromixer with dimensions in mm; (b) 3D Model of Unibody Passive Micromixer.

**Table 3-1.** Process parameters and materials used for the fabrication of the micromixers.

Printing method	Layer height (mm)	Laser spot size or nozzle diameter or resolution	Filling or etching strategy	Type of material
Polyjet	0.028	600 DPI (X and Y axes) 900 DPI (Z axis)	solid, glossy finishing	Vero White Plus UV Photopolymeric Resin
SLA, Stereolithography	0.025	0.14 (mm)	solid	Clear Form V2 UV Photopolymer Resin
FDM, Fused deposition modelling	0.090	0.40 (mm)	raster	Fabbrix natural PLA

filament height or layer thickness ( $h_1$ ), infill orientation ( $\theta$ ), and air gap ( $b$ ). In this study, the infill orientation adjusted at  $60^\circ$  relative to the fluid flow for all printed devices, which results in better mixing performance [118]. First, four devices with different values for the line width parameter are fabricated by keeping constant other printing parameters in slicer software as below:

- The device with a line width of  $200 \mu\text{m}$
- The device with a line width of  $400 \mu\text{m}$

- The device with a line width of 600  $\mu\text{m}$
- The device with a line width of 800  $\mu\text{m}$

Figure 3-6 shows the print paths of the device with line width of 400  $\mu\text{m}$ . As shown in the image, the CAD model is positioned on the build plate in so that the extruded filaments on the bottom of the channel have an angle of  $60^\circ$  relative to the fluid flow. Different print cores with different nozzle diameters are used. The print core AA 0.25 is used for printing devices with a line width of 200  $\mu\text{m}$ , the print core AA 0.4 for devices with line widths of 400 and 600  $\mu\text{m}$  and, the print core AA 0.8 for device with line width of 800  $\mu\text{m}$ . The horizontal interval between adjacent filaments was set to zero, which means that two adjacent filaments are tangent to each other. However, there is a gap between adjacent filaments after printing, which is because of the shrinkages as well as the resolution of the printers. The average air gap as well as the actual values of ridges are measured for all fabricated devices using a high-resolution scanner (see section 3.2.1.3).

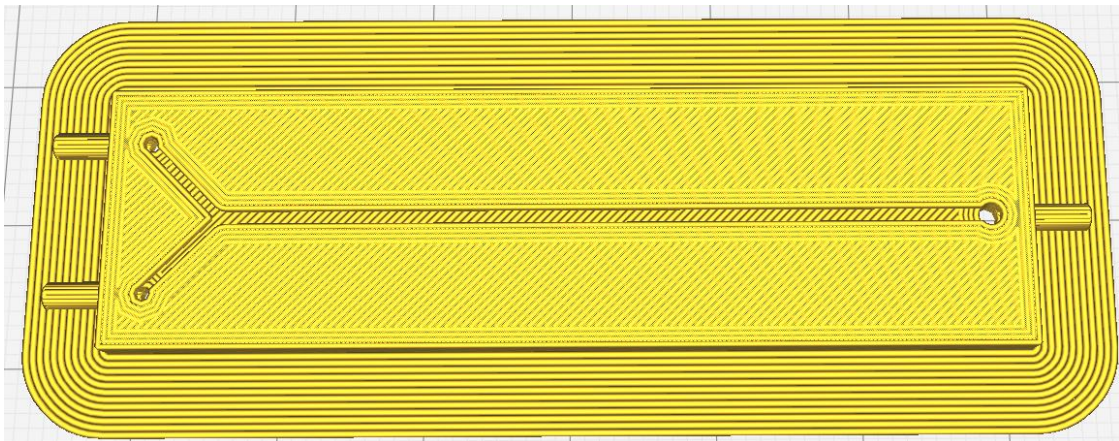


**Figure 3-6.** Schematic showing the movement path of printing nozzle with a line width of 400  $\mu\text{m}$ .

Through the slicer software it is possible to select over 200 printing parameters. In this work, all printing parameters except studied parameters are fixed for all printed devices. The slicer software also proposes different values for each parameter depend on the used material and desired qualities of printed parts. Among the most important parameters are:

- Layer height: the height of extruded filament or each layer (Figure 3-4a); higher values produce faster prints in a lower resolution and lower values produce slower prints in a higher resolution. It is possible to obtain a good quality as regards the geometry of the devices.

- Line width: the width of extruded filament. The higher line width produces faster prints however, the surface roughness increases and there are less details. In this work, it should be noted that with higher values of this parameter, there is more probability of leakage fluids inside devices.
- Outer wall line width: the width of the outermost wall line. By lowering this value, higher levels of detail can be printed. The proposed values by software are adjusted for different print cores used in this work. However, for the devices with line width of 600  $\mu\text{m}$  (nozzle diameter of 0.4 mm), the outer wall line width set 0.4 mm to avoid of problems concerning the occlusion of the inlets as shown in Figure 3-7.

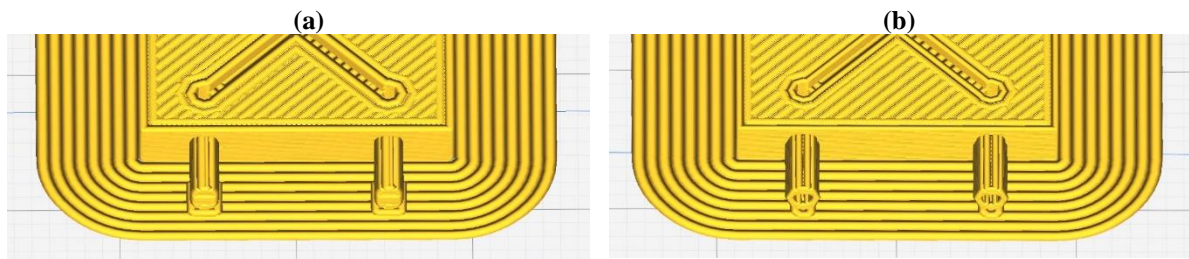


**Figure 3-7.** (a) showing occlusion of the inlets with outer wall line width of 600  $\mu\text{m}$ ; (b) showing the inlets with outer wall line width of 400  $\mu\text{m}$ .

- Ironing: This parameter describes the final surface finish of the printed device. The process includes the passing of hot nozzle without extrusion of material on the last printed layer, in order to obtain a better surface finish. This parameter is enabled for all printed devices but only for the last layer because the fine surface helps for better adhesion between the tape and top surface of the devices when the channels are leave open without roofing (see section 3.2.1.4).
- Infill density: It adjusts the density of infill of the print. It was set to 100 % for all devices to minimize the possibility of fluid leaking.
- Flow: Flow was set to 100 % for all devices. Flow parameter in slicer (which is also called “flow rate”) specifies the rate at which the printer will extrude material. Based on the value for this setting, slicer software automatically calculates how fast to move the extruder motor for certain print speeds or filament diameters.
- Printing temperature: The temperature used for printing. It depends on the type of material. In this work, different materials are used (see section 3.2.1.2). For example, temperature was

set to 200 ° C for the printed devices with natural PLA. The build plate temperature also refers to the temperature used for the heated build plate.

- Print speed: It measures the amount of manufactured material over a given time period. Different values were set for this parameter depend on the used materials and required quality.
- Build plate adhesion: When polymer materials are printed, they firstly expand slightly but contract as they cool down. This parameter is enabled to prevent warping phenomenon in printing and to ensure the good adhesion between the part and build plate.

There are a set of other parameters which can set in slicer software. All process parameters are brought in Appendix A in detail. Once the setting printing parameters has been done, slicer software generates instructions for the 3D printer as a G-code file. Before proceeding with printing, it is necessary to load the desired print core and material for each device. The next step is to calibrate the printer (z-leveling), to ensure reliable adhesion between the print and bed. If the distance between the nozzle and the build plate is too wide, the print will not adhere perfectly to the build plate, while if it is too close to the build plate, it can prevent the material extruding from the nozzle.

Each of the used printers either FFF printers or SLA (see section 3.2.1.3) have a specific procedure for calibration. For example, the FFF Ultimaker printers allow to follow two different methods for the calibration: manual leveling and active leveling. If the level of the build plate is too far off (and active leveling cannot compensate for this), manual leveling can be performed. This is done using a calibration card between the nozzle and build plate at different positions as shown in Figure 3-8. Active leveling is the preferred choice, as there is a reduced chance of human error. During the active leveling, the printer will measure the distance between the tip of the nozzle and the build plate in several locations. These positions are stored in the printer, so it can compensate for inaccuracies of the build plate level during the initial layers of the print.



**Figure 3-8.** Manual calibration of the Ultimaker printers using calibration card.

### 3.2.1.1 Post Printing Steps

The printed microfluidics with different 3D printing techniques require a series of post printing processes before being tested. These activities for FFF printed devices are:

- Removal of the brim: A simple cutter is used to remove the brim around the printed devices (Figure 3-9). Subsequently, using a fine-grained sandpaper for cleaning edges of the devices.
- Removal of the supports: The present supports under the inlets/outlets are removed using a fine-grained sandpaper (Figure 3-10). This step requires particular attention in the areas around the connectors. It is necessary to make the connectors cylindrical. The fluids will leak if this step is not done correctly.



**Figure 3-9.** FFF 3D-printed micromixer with brim after removing from the build plate.

- Cleaning the channels: The devices still contain the residuals of the filament both on the surfaces and the channel. The channels are washed using ethyl alcohol to eliminate residual impurities. Two types of devices are printed with FFF process: the devices with open channels and the devices with roofed channels. The top surface of open channels will close as described in section 3.2.1.4.

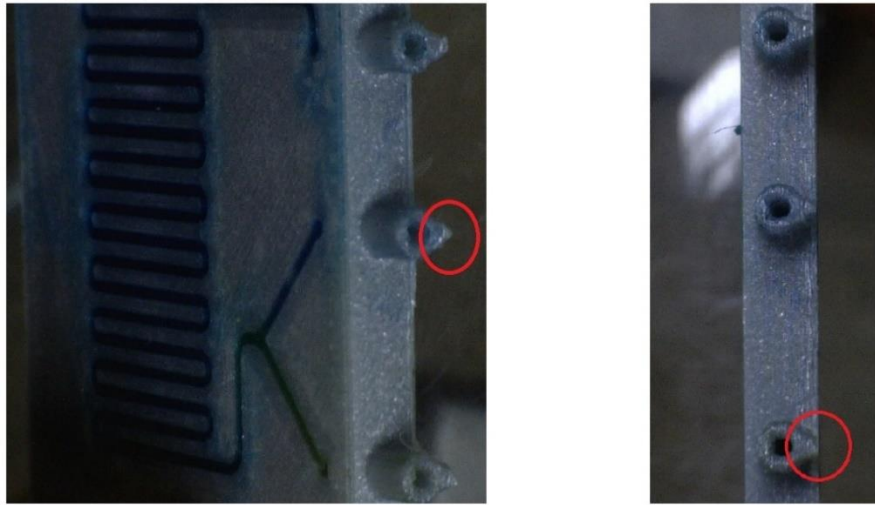


**Figure 3-10.** Supports under the connectors of a FFF printed mixer with gray PLA.

The post printing process for printed devices with Polyjet method is simple. After printing models, allow them to cool in the printer, with the cover closed and then, the support material can be removed. However, this process can be more difficult for printed devices with SLA method. For SLA printed part, the channel is built by photopolymerizing first the layers that build the channel walls and then the layers that constitute the roof, leaving trapped uncured resin in the channels. This uncured resin is removed before the part is brought to ambient light; exposing the print to ambient light at this point can cause photopolymerization of the uncured resin inside the channel. Immediately after printing, a pressure source (e.g., a compressor) is used to remove the uncured resin, and a series of washes with water and Isopropyl Alcohol (IPA) to remove unreacted monomers. At this point, the print has very little to no stickiness left on its surface. Next, gently the printing supports are removed with a cutter. It is easier to detach the supports closer to the tips, since the supports are pointed. The last step is using a UV-post curing lamp or direct sunlight to complete the final curing process.

### **3.2.1.2 Materials and Chemicals**

In this study, three different 3D printing methods are used for fabrication of microfluidics micromixers as well as DNA extraction chip. The used materials for FFF printers are: two natural polylactic acid (PLA) 2.85 mm diameter filaments (i) transparent PLA, (ii) translucent PLA, and (iii) high temperature PLA (HT-PLA), all were purchased from Fabbrix, Italy. PLA is the most commonly used biocompatible polymer in drug delivery systems, tissue

engineering, and temporary and long-term implantable devices [120]. In addition to biocompatibility, transparency of the printed device is a vital point in microfluidics. Transparency allows fluid interactions to be clearly visible through the detection system. The standard PLA has poor heat resistance therefore, printed devices are not suitable for applications that need to be exposed to temperatures beyond the glass transition (60-65 °C). The printed devices with high-temperature PLA can safely be exposed to temperatures of up to 115 °C without suffering deformation after a post-printing annealing step.

Clear form V2 and MiiCraft BV-007A resins are used for Formlabs Form 2 and MiiCraft 50Y SLA printers, respectively. Vero white plus resin is used for printed microfluidics with Stratasys Objet30 Polyjet printer.

Aqueous solutions are used to evaluate the performance of printed micromixers. For this, two categories of tests are done based on the type of used solutions. The tests in which water-based solutions stained with yellow and blue food color (purchased from local shop) are used for mixing performance. Different colors help to distinguish one solution from another one as well as tracking the point with complete mixing. However, the diffusion coefficient (D) for these solutions is not known. As already highlighted, the diffusion coefficient is a factor that influences the mixing process of aqueous solutions and therefore its value is fundamental for conducting numerical simulations. The second set of used solutions are Methylene blue (Euromex, Netherlands) and deionized (DI) water streams, where Methylene blue (solute) dissolved in DI water injects from one inlet and DI water from the other inlet. Methylene blue is a salt used as a dye and as a medication. The intravenous form of methylene blue is approved by the FDA for the treatment of pediatric and adult patients with acquired methemoglobinemia.

The amount of solutions are prepared using an accurate electronic balance, where 0.13 gr of the Methylene blue dissolved in 20.01 gr of DI water as shown in Figure 3-11. The diffusion coefficient of the resulting solution is calculated based on the work by Miložič [121]. The molar concentration of Methylene blue dissolved in DI water is calculated as below:

$$c = \frac{m_{MB}}{MM_{MB} V} = 20.312 \text{ mol/m}^3$$

Where,  $m_{MB}$  is the mass of Methylene blue,  $MM_{MB}$  is the molecular mass of Methylene Blue, and  $V$  is the volume of the solution in  $m^3$ .



**Figure 3-11.** Preparation a mixture of DI water and Methylene blue.

### **3.2.1.3 Instrumentation**

#### ***3D printers***

All microfluidic devices are designed using PTC Creo (Student Edition). The designed CAD models are exported in STL format and then imported into the relevant slicer software. Different slicing software are used depend on the used technology and printer. For FFF printers, the open-source Ultimaker Cura 4.4.0 software used for setting printing parameters and for slicing .stl files into G-code. The majority of microfluidics devices in this research are fabricated using two FFF printers : the Ultimaker 3 and the Ultimaker S5 (Ultimaker, Utrecht, Netherlands) (Figure 3-12). These two printers are similar from same company with different resolution and build volume. The build volumes are  $215 \times 215 \times 200$  mm and  $330 \times 240 \times 300$  mm for the Ultimaker 3 and the Ultimaker S5, respectively. The declared layer resolution is 20-200 microns in the Ultimaker 3, and 60-150 and 20-200 microns in the Ultimaker S5 for 0.25 mm and 0.4 mm nozzles, respectively. The accuracy (XYZ) is 12.5, 12.5, and 2.5, and 6.9, 6.9, and 2.5 microns for the Ultimaker 3 and Ultimaker S5 printers, respectively.



**Figure 3-12.** FFF printers. Left: Ultimaker 3; Right: Ultimaker S5.

Two stereolithography printers are used in this research to compare SLA printed chips with the FFF chips. The Formlabs Form 2 uses an ultraviolet (UV) laser to cure the resin between the print head and the bottom of the print tray (Figure 3-13). The build size (XYZ) of Form 2 is 145×145×175 mm, with a laser spot size of 140 microns. The print resolution in Z axis can be 25 - 50 -100 microns. The MiiCraft Ultra 50 printer is used to print DNA extraction chip (Figure 3-13). The MiiCraft printer is a DLP base printer that use a digital projector to cure the liquid resin. The used LED projector with a wavelength of 365 nm and the XY resolution of 30  $\mu\text{m}$  makes the MiiCraft Ultra 50 as a powerful tool for manufacturing of microchannels. The build size (XYZ) of the MiiCraft Ultra 50 is 57×32×120 mm.



**Figure 3-13.** SLA printers. Left: Formlabs Form 2; Right: MiiCraft Ultra 50.

The Polyjet printing is another 3D printing method which is compared with FFF method. The Stratasys Objet30 printer is used for fabrication of microfluidic micromixers (Figure 3-14). It works like inkjet document printing, but instead of jetting drops of ink onto paper, the print head jets microscopic layers of liquid photopolymer onto a build tray and instantly cures them with UV light. The XY resolution is 600×600 dpi, with a minimum layer thickness of 28 microns. The maximum build size (XYZ) of the printer is 294×192×148.6 mm.



**Figure 3-14.** Stratasys Objet30 Polyjet printer.

### ***Measuring and image acquisition instruments***

3D high precision Conoscan 4000 is used to analyze the surface topography on the bottom of the printed channels by FFF (Optimet, North Andover, USA, Figure 3-15). The Conoscan 4000 uses Optimet's conoscopic holography sensors with interchangeable objective lenses from 100mm down to 25mm HD lens with up to micron precision. The Optimet co-linear technology allows measuring deep holes and grooves. The Conoscan 4000 integrated with a sophisticated scanning platform made up of three motorized axes (X, Y, and height Z) and is provided with user friendly, robust scanner software. The actual parameters of the patterned ridges made by FFF are measured using objective Lens 25 mm, with a precision of 2  $\mu\text{m}$  (z-axis) and a laser spot size of 12  $\mu\text{m}$ .

Nikon Eclipse MA200 microscope is used to take high resolution and high contrast images from the printed microchannels (Nikon Corporation, Tokyo, Japan, Figure 3-15). While, the

fluid within the microchannels is captured using a charge-coupled device (CCD) camera (Canon EOS 4000D, Tokyo, Japan) with a macro lens (Canon EF 100 mm f/2.8 Macro USM, Tokyo, Japan) (Figure 3-16).



**Figure 3-15.** Left: High Precision Conoscan; Right: Nikon Eclipse MA200 microscope.



**Figure 3-16.** Canon camera with a macro lens used for capturing images from top of channels.

#### **3.2.1.4 Experimental setup**

Prior to start the tests, the devices are cleaned with water and ethanol 80%, and dried using warm air. Compressed air jets are used to eliminate any drops of water trapped inside the channels. For printed devices that the channels leave open without the roofing, a transparent double-sided tape (3M Ruban Adhesif Scotch®) is used to close the open sides of the microfluidic micromixers (Figure 3-17). Prior applying the tape, the top and bottom surfaces are smoothed using abrasive finishing paper to ensure an effective seal.

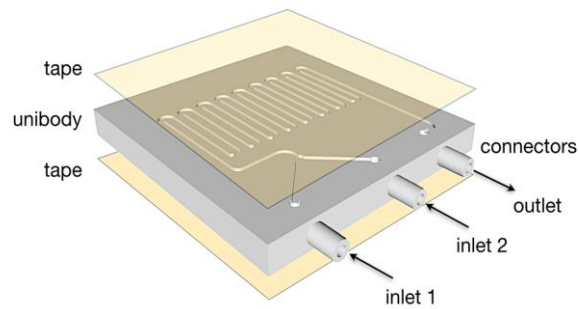


**Figure 3-17.** Transparent double-sided tape is applied to the top and bottom of the device.

Different solutions are injected using syringe pumps (Braintree, MA, USA, Mod. BS-300) equipped with 5 mL disposable syringes shown in Figure 3-18. The syringes pumps provide precise reproducible flow rates. The syringe pumps provide a maximum pumping rate of 1500 ml/hr with a 60 ml syringe. The microfluidic devices are connected to syringes using silicon tubes. An ad hoc setup is configured to characterize the devices as shown in Figure 3-19. The structure consisting of a plywood frame that supports two transparent plexiglass sheets. A bottom plate and double-sided adhesive tape are used to fix the devices in place. The camera was placed on the top plate for detection. A white cell phone screen was positioned below the lower plate to provide homogenous back-illumination (Figure 3-19).



**Figure 3-18.** BS-300 Braintree syringe pumps for injecting solutions with disposable syringes.

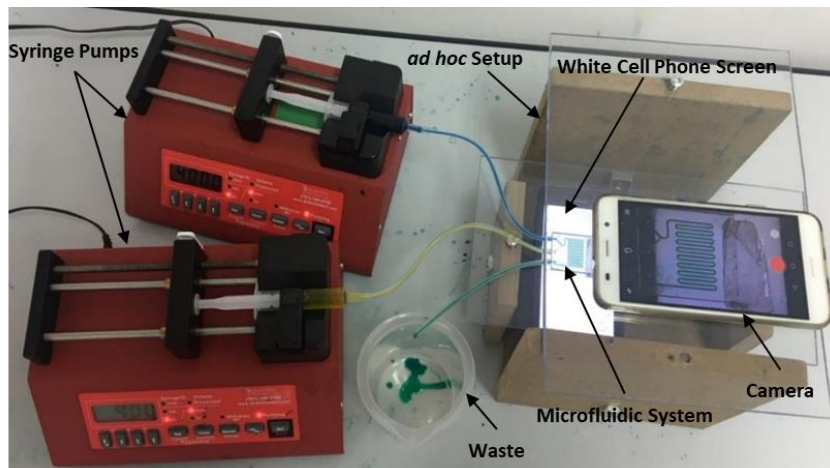


**Figure 3-19.** Experimental setup and detection system for testing microfluidic systems.

The silicon tubes may contain bubbles and therefore, should be check before injecting the fluids to the device. Forming a bubble may also happen if the fluids do not inject into the main channel simultaneously (Figure 3-20a). It is necessary to eliminate the bubbles before starting the tests by setting a low flow rate for the pumps to ensure that the operator can control the entry of the fluids. once the fluids entered the main channel at same time then, the test can continue at the desired flow rate (Figure 3-20b). At the end of each test, the devices are cleaned and prepared for other tests as described in first paragraph of section 3.2.1.4.

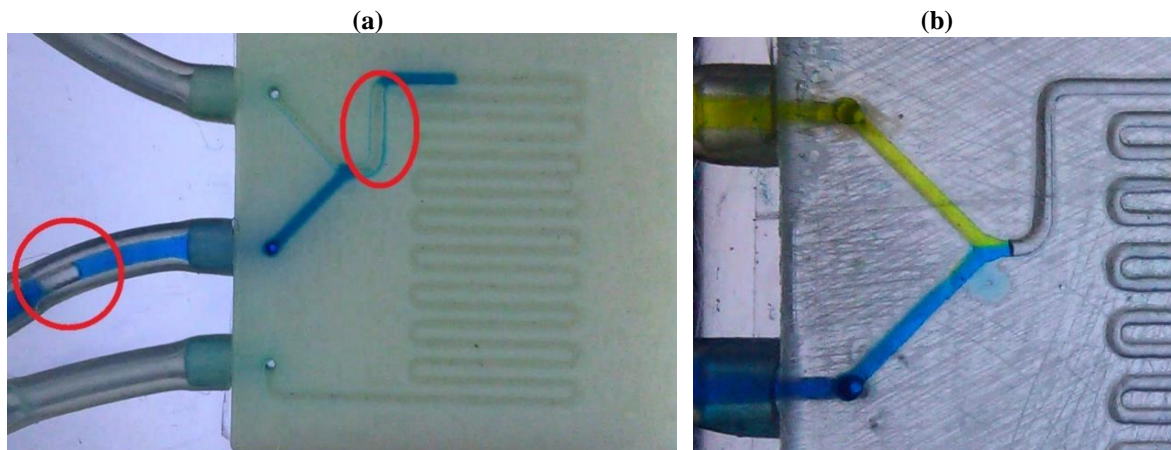


**Figure 3-20.** Experimental setup and detection system for testing microfluidic systems.

### 3.2.2 Numerical Simulation

Mixing simulations are performed with COMSOL Multiphysics software (COMSOL Inc., Stockholm, Sweden) to compare the fluid behavior of different channel designs. With

COMSOL Multiphysics it is possible to study a series of physical phenomena, such as structural, thermal, fluid dynamics, acoustic, chemical problems, as well as the combined effect of several physics. For this study, the input data are geometrical model and physical parameters. As previously mentioned, in FFF process due to the resolution of the process and present shrinkages, the actual dimensions may be different from CAD model. In this study, the computational domain is designed using extracted geometrical information by the Conoscan scanner. The actual parameters of ridges are extracted, and new geometries imported to the software. The Navier-Stokes and convection-diffusion equations are solved using a finite-element approach. The fluid is considered incompressible with the same properties of water (density: 998 [ $kg/m^3$ ], viscosity: 1 [ $mPa \cdot s$ ]). The molar concentration of Methylene blue dissolved in DI water was set to 20.312 [ $mol/m^3$ ] regarding the used mass amount of each. The diffusion coefficient was set to  $4.3362 \cdot 10^{-10}$  [ $m^2/s$ ] following the model presented by Siddiqi-Lucas for prediction diffusion coefficient in aqueous solutions with a maximum estimated error of 13% [121]. Steady-flow simulations are performed, imposing the flowrate at the two inlets and standard outflow conditions at the outlet. Body forces are neglected. The laminar model is used with the flow rates set to 5, 10, 20, 40, 80, and 150  $\mu L/min$ , respectively. In order to obtain converged results and avoid numerical diffusion, a high-quality structured-unstructured mesh was created (hybrid mesh), starting by placing a given number of equally spaced nodes on the top surface and the two lateral sides of the mixing channel (Figure 3-21). The numerical diffusion minimized by combining a high order discretization and using both streamline and crosswind consistent stabilization methods [122, 123]. Mesh resolution is increased near the ridges due to the increased velocity and molar concentration gradients. After a grid-convergence study, the final mesh size was about 1298506, 973544, and 911646 cells for channel 1, 2, and 3 respectively (see chapter 4 for 3 different channels). MSE is calculated as shown in following equation:

$$MSE = \frac{\sum_i^n (\bar{c}_i - \bar{c})^2}{n m}$$

Where,  $\bar{c}_i$  denotes the mean along the i-th column,  $\bar{c}$  is the average of means, and n and m are number of columns and rows in each region of interest (ROI), respectively.

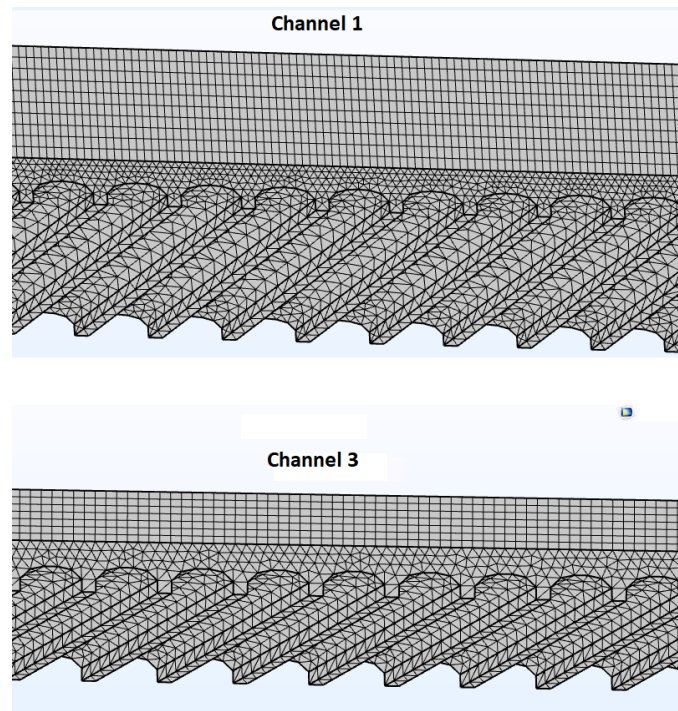


**Figure 3-21.** High quality structured–unstructured mesh used for the numerical simulation. Channel 1 is a channel with height of 600  $\mu\text{m}$ , the height for the channel 3 is 300  $\mu\text{m}$ .

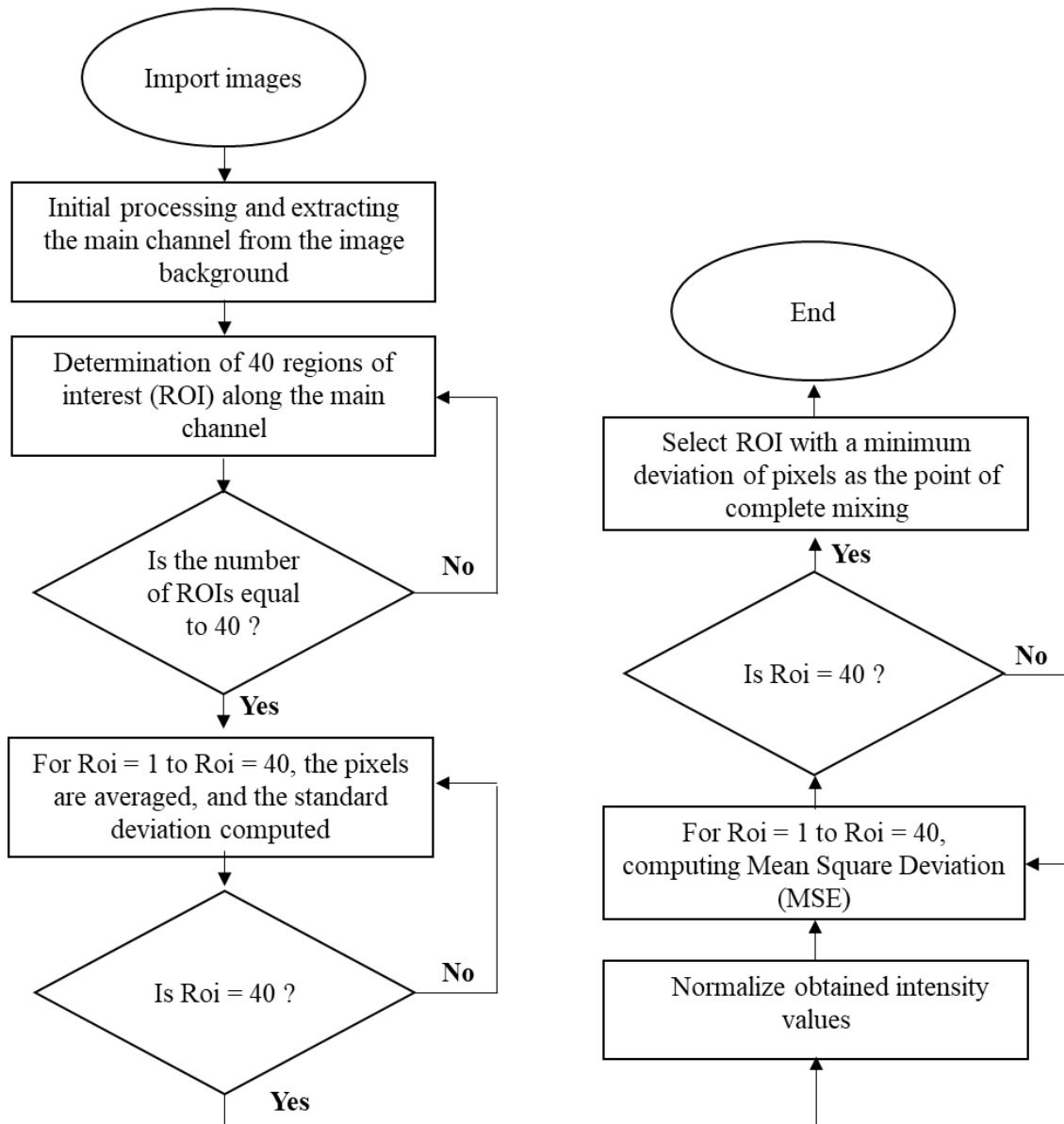
### 3.2.3 Colorimetric Analysis

Microscopes are normally used for the visualization of fluids interaction and analysis of mixing. In this work, an alternative method for is created for the acquisition and analysis of the mixing within the micromixers. The procedure involves the use of a CCD camera equipped with a macro lens for image acquisition and a bespoke MATLAB algorithm.

The performance of the printed devices in mixing the two fluids evaluate by analyzing images taken from the microchannels. The flowchart of the colorimetric analysis is shown in Figure 3-22. Figure 3-23a shows a sample of the captured image with the detection system. The first step in the colorimetric analysis is the extraction of the main channel from the image background to determine a set of regions of interest (ROIs) along the microchannel to address the performance of mixing. The pixel coordinates of microchannel are different from one device to other one even with fixing the camera. To solve this problem and determine a specified number of ROIs, the below steps are implemented:

- a) Import images and initial processing

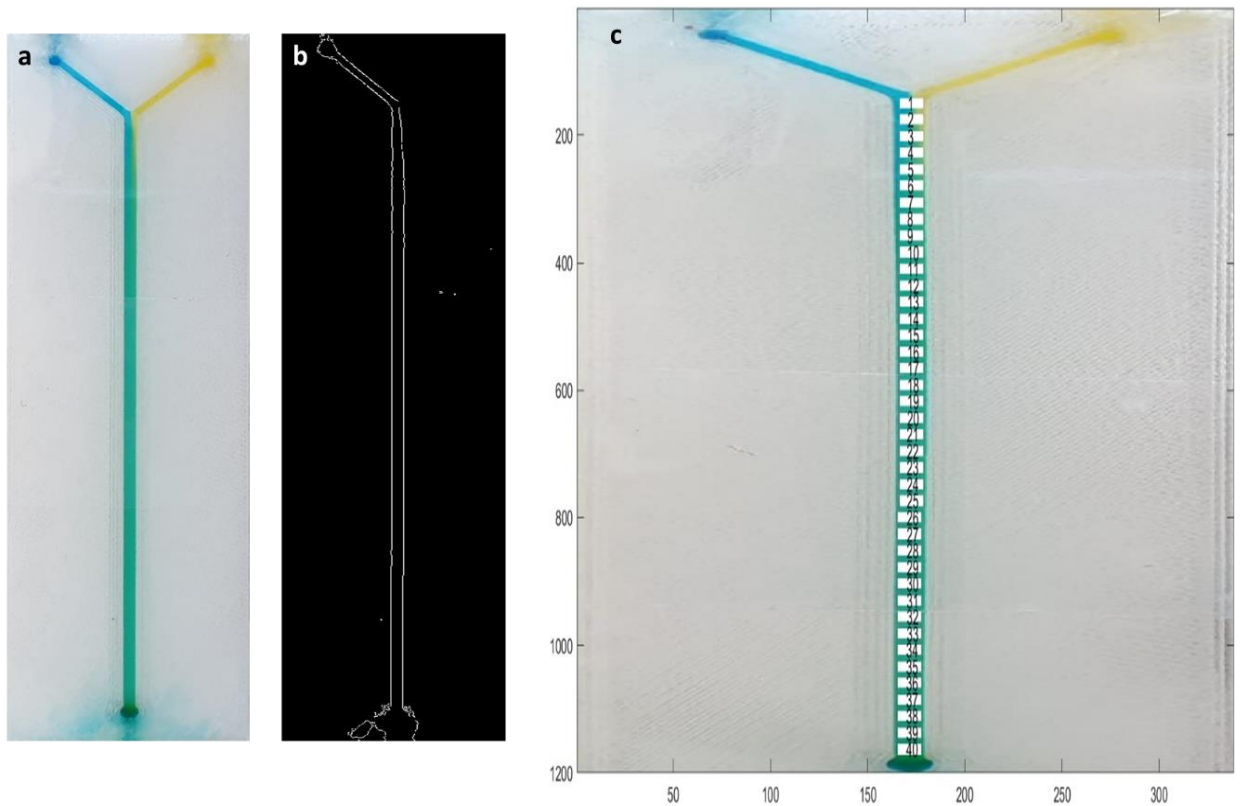
- b) Separating micro-mixer with channel from the background of images
- c) Grayscale of images
- d) Binary of the images
- e) Edge detection
- f) Removal or reduction noise



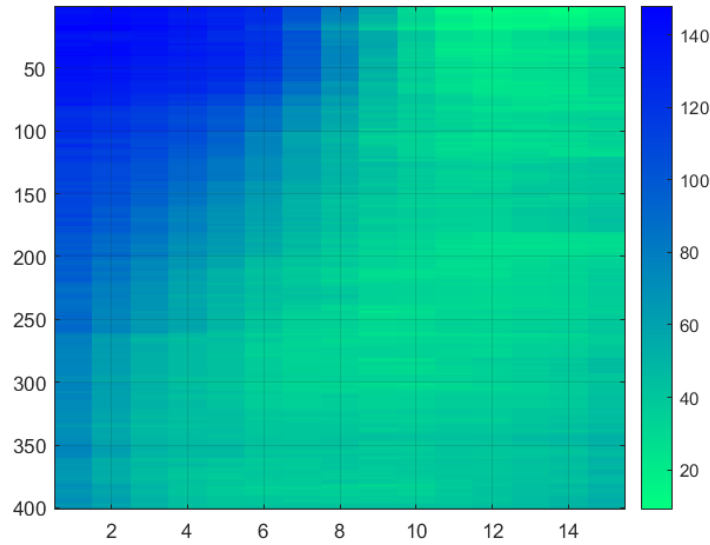
**Figure 3-22.** Data flowchart of the colorimetric analysis.

Figure 3-23b shows the extracted microchannel at a grayscale level. The next step is considering a set of 40 rectangular ROIs (it can be different, higher ROIs results higher

accuracy in finding the point with maximum mixing) at regular intervals perpendicular to the main channel to obtain the change in color intensity across the channel (Figure 3-23c). Pixels inside the different ROIs have three different values for red, green, and blue intensity. Figure 3-24 shows the red intensity data for different ROIs as an image. The resulting image is an  $m$ -by- $n$  grid of pixels where  $m$  is the width of a single ROIs and  $n$  is the sum of the height of all ROIs. For every ROI covering the width of the channel, the obtained intensity values are normalized to the intensity of the dyed streams before mixing, the pixels are averaged, and the standard deviation is calculated for every position along  $w$  (width of single ROI).



**Figure 3-23.**(a) Captured image from the top of the device; (b) detection of the main channel from the input image; (c) different ROIs along the main channel at regular intervals.



**Figure 3-24.** Displaying red intensity in different ROIs as an image.

Figure 3-25 describes the normalized color intensity across the channel for 40 ROIs at different flow rates, illustrating the homogenization of the color intensity at the outlet, where the blue stream dissolved in the yellow stream, becoming a homogeneous green color. To find the length of the channel in which complete mixing is achieved, the mean squared deviation was calculated as follows:

$$\text{MSE} = \frac{\sum_{i=1}^n (I_i - \bar{I})^2}{n}$$

where  $I_i$  denotes the intensity of the  $i$ -th pixel in every ROI;  $n$  is the total number of pixels in ROI; and  $\bar{I}$  is mean intensity, calculates as follows:

$$\bar{I} = \frac{\sum_{i=1}^n I_i}{n}$$

The ROI with a minimum deviation of pixels is selected as the point with complete mixing, where at least 90% of the fluids are mixed (Figure 3-26).

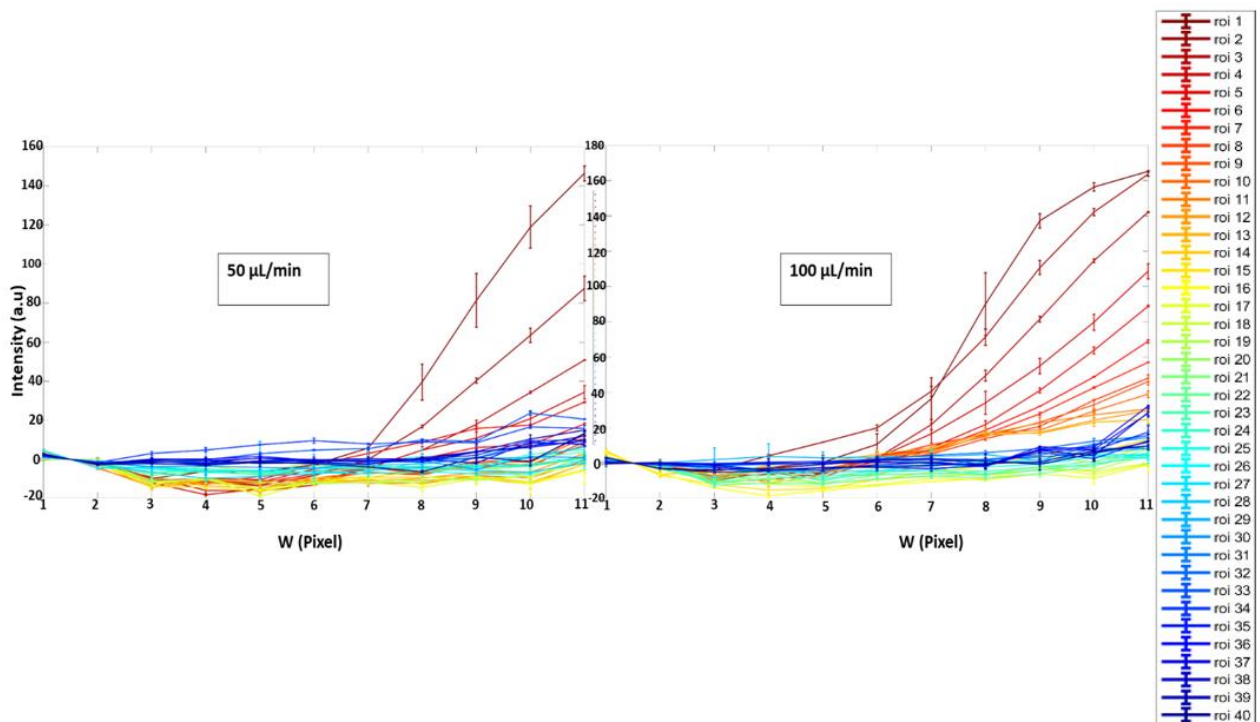


**Figure 3-25.** Mixing trend diagrams at flow rates of 50 and 100  $\mu\text{L}/\text{min}$ . At the beginning of the main channel, as the fluids are not yet mixed, the curves have two peaks. The curve corresponding to the ROI with complete mixing is a straight line.

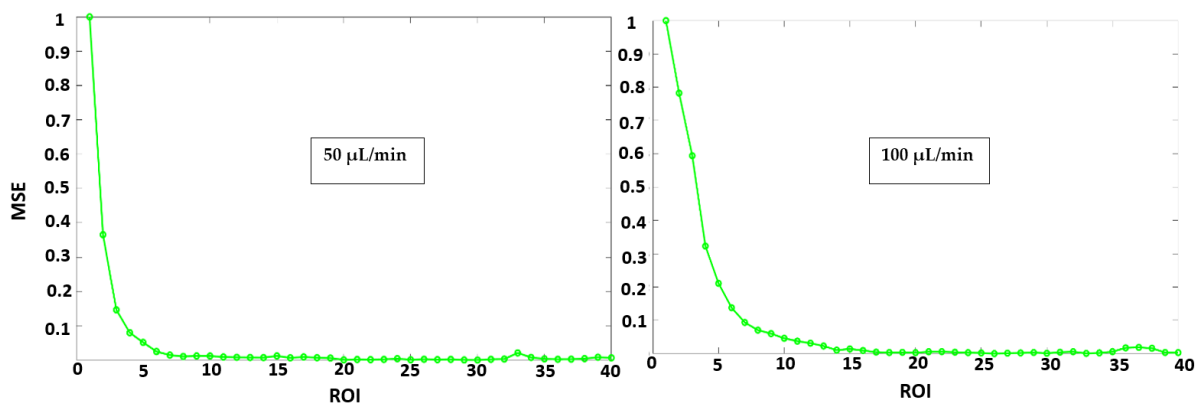


**Figure 3-26.** Normalized mean square errors (MSEs) versus different ROIs at flow rates of 50 and 100  $\mu\text{L}/\text{min}$ . Complete mixing is achieved after ROI number 7 and 16 at flow rates of 50 and 100  $\mu\text{L}/\text{min}$ , respectively.

### 3.3 Design Lysis and DNA Extraction Chip

In this section, a microfluidic chip for lysis and DNA extraction will be designed, developed, and characterized. There are several common methods for extraction DNA as explained in chapter 2. One of the methods is using magnetic beads for separation targeted DNA from other non-targeted substances under the influence of magnetic field, which is used in this work.

Before the extraction process, it needs to break the cell membranes; a process which is called cell Lysis (Figure 3-27). The cell lysis plays an important role in obtaining intracellular components, whose quality will directly influence the subsequent extraction and analysis. There are few studies in the area where the microfluidic devices are used for cell lysis. The difficulty comes from the problems in mixing two or more fluids in small microchannels as well as the time required for incubation.

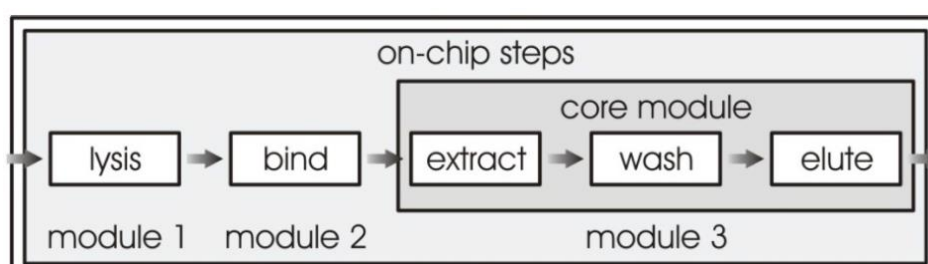


**Figure 3-27.** Block diagram of the steps of DNA extraction implemented on microfluidics [107].

In this study, the below protocol is considered as a base for design of chip; that is the used protocol for manual DNA extraction proposed by Masmec Biomed company [124].

Step 1: The sample (50  $\mu$ l) mix with the lysis solution (50  $\mu$ l) and incubate for 600 s with shaking.

Step 2: The beads (20  $\mu$ l or 7  $\mu$ l) and the binding solution (100  $\mu$ l) added to the previous solution. The overall mixture must remain stirred for about 300 s.

Step 3: Using a magnet to attract the DNA-carrying beads, removal the liquid part (waste), adding washing solution A (265  $\mu$ l) and mixing.

Step 4: Using a magnet to attract the DNA-carrying beads, removal the liquid part (waste), adding washing solution B (265  $\mu$ l) and mixing again.

Step 5: Using a magnet to attract the DNA-carrying beads, removal the liquid part (waste), adding washing solution C (185  $\mu$ l) and mixing.

Step 6: Using a magnet to attract the DNA-carrying beads, removal of the liquid part (waste).

Step 7: Drying at 65 ° C for 240 s.

Step 8: Elution.

The chip design includes three main processes: Lysis process, Binding process, and Extraction process. The initial proposed chip design including three main modules for lysis and DNA extraction is shown in Figure 3-28. The sample and other required solutions including lysis buffer, magnetic beads buffer, washing buffer, and elute buffer are injected through five inlets. After passing through three different steps, purified DNA collected in outlet 1, and the other impurities in outlets number 2 and 3. Microfluidic chip is designed using PTC Creo (Student Edition). The following is a detailed description of the three main steps: Lysis process, Binding process, and Extraction process.

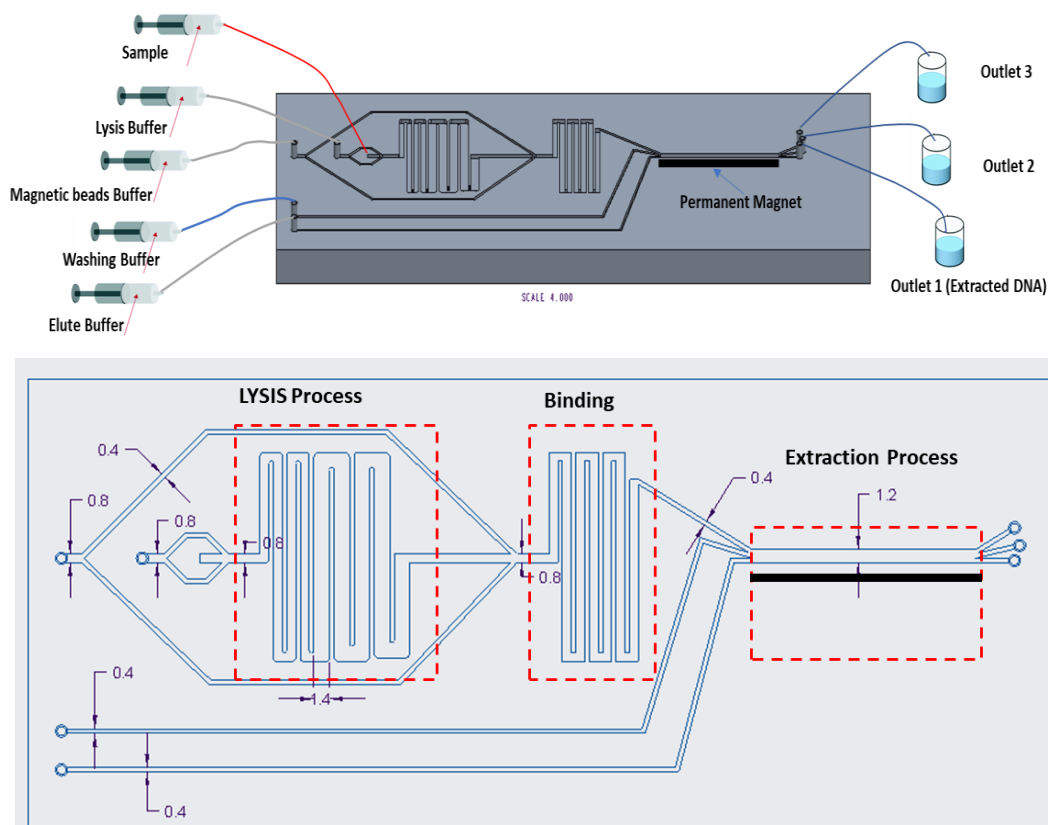


**Figure 3-28.** CAD model of the initial chip for the lysis and DNA extraction with dimensions in mm.

### 3.3.1 Lysis Process

The different lysis methods for breaking the cell membranes discussed in chapter 2. The chemical lysis is the simplest method for lysis process, where a lysis solution is used for breaking the cell membranes of samples; however, chemical lysis is a method with a low efficiency. In this study, a combination of the chemical and thermal lysis methods is proposed for lysing which increase the efficiency of the lysis process. Applying these two methods for microfluidics is not complex, where a thermal shock applied to the cells after mixing with lysis buffer by using a heater resistor attached to the bottom of the chip. For continuous lysis process, a channel structure is required that allows merging, mixing, and incubation of sample with lysis buffer. Hence, a channel as shown in Figure 3-29a is proposed for merging the solutions. The sample injected from the middle inlet and the lysis buffer from two other sides. This configuration can increase the contact area between the sample and lysis buffer at the beginning of the main channel and therefore, enhancing mixing process. The laminar flow in microfluidics demands long length of the channel for complete mixing. To overcome this challenge, a serpentine channel along with oblique-oriented ridges (which is an inherent property of the FFF process) on bottom of the channels will print to enhance mixing (Figure 3-29b) [125, 126].

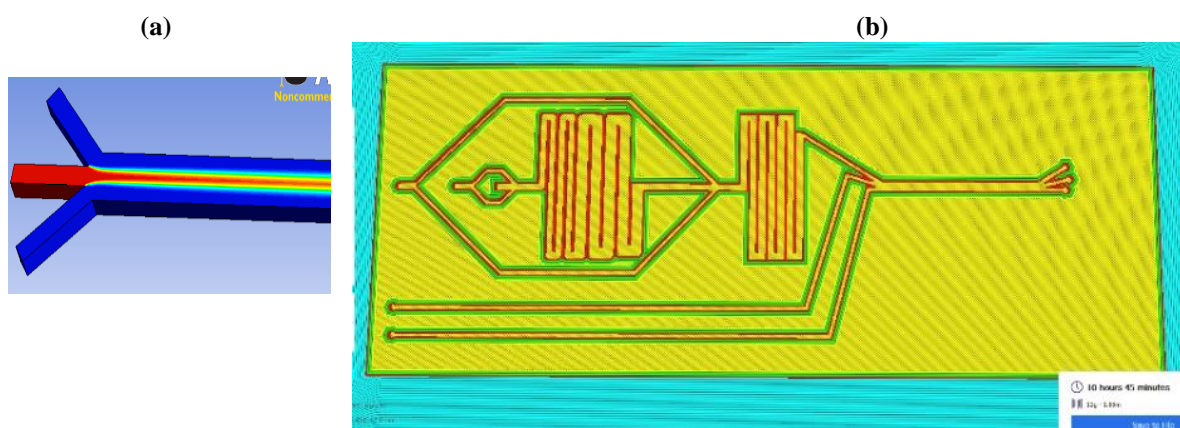


**Figure 3-29.** Structure of the inlet (a), and channel (b) in lysis process.

Other important parameters for lysis are incubation temperature and incubation time. These parameters should be considered regarding the type of samples. In this study, the incubation is considered with a temperature of  $60^{\circ}$  and a time of 600 s. According to the used kit, a channel

structure is designed which can provide incubation time of 600 s, at a flow rate of 10 microliters/minutes. It is possible to provide different incubation time depend on the sample by altering the input fluid velocity. In general, the lysis channel has the following characteristics:

- Three inlets merge into one channel
- Mixing enhancement using serpentine channel and patterned ridges
- Incubation

After the channel junction that merge sample with lysis buffer, a 67 mm long channel (width: 0.8 mm) provided for mixing (passage time 192 s). This length is sufficient for the mixing lysis buffer and sample. Downstream of the mixing channel, an incubation channel is implemented with an increased channel width of 1.4 mm to lower the mean flow velocity to  $1.98 \times 10^{-4}$  m/s, resulting in a passage time through the 80 mm long incubation channel of 408 s. The required thermal shock will provide using a heating resistor attached to the bottom of the chip; the proposed temperature is  $60^\circ$  based on the used protocol. The outlet of the incubation channel allowed for further analysis of lysate in the next step. Here, is the calculation for lysis channel:

$$L_{mix} = Vt_{mix} = lPe$$

Where,  $L_{mix}$  is the required channel length for mixing,  $t_{mix}$  is the mixing time, and Pe is the Peclet number.

$$Re = \frac{D_{eq} \times V}{\nu}$$

Where, Re is Reynolds number,  $\nu$  is flow velocity, D is the pipe diameter or hydraulic diameter,  $\vartheta$  is the cinematic viscosity (water cinematic viscosity = 1,002 cSt).

Mixing channel:  $w_1 = 800$  micrometers,  $h_1 = 600$  micrometers,  $L_1 = 67$  mm,  $V_1 = 3.48 \times 10^{-4}$  m/s,  $t_1 = 192$  s

Incubation:  $w_2 = 1400$  micrometers,  $h_2 = 600$  micrometers,  $L_2 = 80$  mm,  $V_2 = 1.98 \times 10^{-4}$  m/s,  $t_2 = 408$  s.

### **3.3.2 Binding process**

The binding structure requires three inlets, one for the cell lysate and two others for the binding buffer (Figure 3-28). A junction like lysis step is used for merging the lysate and binding solution (Figure 3-29a). This can help for increasing efficiency of binding process and therefore binding the DNA to the magnetic beads. Furthermore, the binding structure should provide the possibility to incubate the lysate with the magnet beads for a specific amount of time to enable the binding of the DNA to the beads. A serpentine channel with width of 0.8 mm and height 0.6 mm is used for the binding channel. The required incubation time is realized by implementing a downstream serpentine channel (Figure 3-28).

### **3.3.3 Extraction process**

Extraction part of chip has three inlets with three outlets. The resulting solution in the previous steps injected from one inlet, washing and eluate buffers from two other inlets. A permanent magnet is positioned at 2 mm from channel wall (Figure 3-28). Three outlets are used for collecting DNA and other molecules and impurities. Here, are three main steps for extraction DNA:

Step 1: DNA-carrying beads with other impurities injected from one inlet, washing and elute solutions from other two inlets.

Step 2: Purification/washing. DNA-carrying beads pass across the interfaces of different buffers via magnetic force provided by external permanent magnet and other molecules / waste are removed by washing buffer (ethanol 80%).

Step 3: Elution. Lastly, DNA is eluted from the DNA-carrying beads.

The approach removes the need for vacuum or centrifugation, which minimizes stress or shearing forces on the target molecules, requires fewer steps and reagents than other DNA extraction protocols, and is amenable to automation.

### 3.3.4 Fabrication

In this study, in order to evaluate the performance of each different part of the chip, the initial design is divided into two different chips as shown in Figure 3-30. The new designs will help to investigate the efficiency of lysis, binding, and extraction processes separately. This includes the optimum dimensions for the channels, incubation, working flowrates, position of permanent magnet rather than the channel wall, etc.

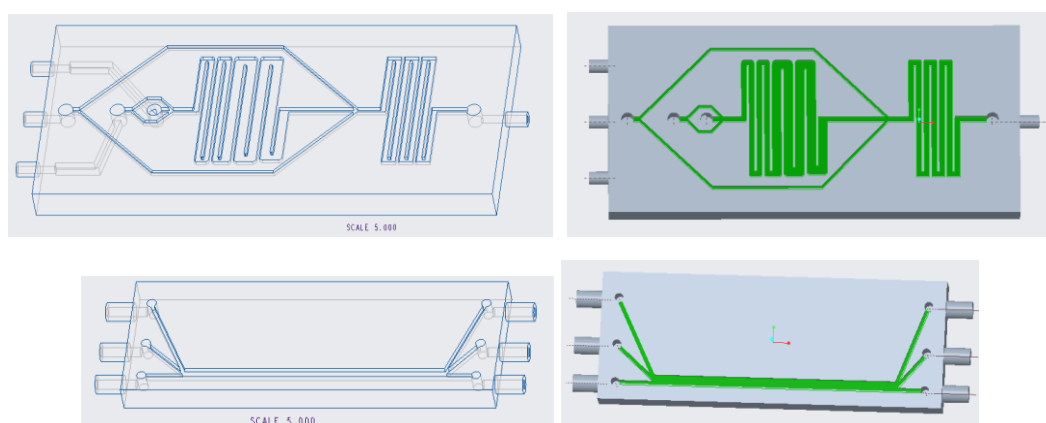


**Figure 3-30.** Top: 3D CAD model of lysis and binding chip; Bottom: 3D CAD model of extraction chip.

The designed CAD models are exported in STL format and then imported into the slicer software. The open-source Ultimaker Cura 4.4.0 software is used for setting printing parameters and slicing .stl files into G-code. The devices are printed using Ultimaker 3 printer. FFF printers are least expensive, with regard to both purchase and operate, and have the largest selection in material choice—some of which are biocompatible (PLA, COC), electrically conductive, and have specific chemical resistance (COC, for example, which is resistant to hydrolysis, acids, alkalis, as well as polar solvents such as methanol). Natural transparent PLA and high temperature PLA (HT-PLA) are used for fabrication of chips with FFF method, and Thermoplastic Polyurethane (TPU) is used for the chip holder. Two set of devices are fabricated with FFF method; the devices in which the top surface of channels leaves open without the roofing (transparent double-sided tape is used to close the open side), and devices that channels are closed with polymethyl methacrylate (PMMA) material. PMMA sheets are obtained from local shop with nominal thickness of 1mm. The extraction chip also printed using a DLP printer (MiiCraft Ultra 50). Fluke PTi120 thermal camera ([www.fluke.com](http://www.fluke.com)) used

for controlling the temperature at top surface of the channel (Figure 3-31). The purity of DNA/RNA are checked using a Thermo Scientific™ NanoDrop™ (Figure 3-32, Waltham, Massachusetts, United States). The reagents of two different kits are used for extraction DNA/RNA from plant and saliva samples. The NucleoMag Blood 200  $\mu$ L kit [127] was used for saliva sample, and NucleoMag Plant kit [128] for DNA/ RNA extraction from plants.



**Figure 3-31.** Fluke PTi120 thermal camera.



**Figure 3-32.** Thermo Scientific™ NanoDrop™ .

# **Chapter 4 :**

## **Results and Discussion**

## 4.1 Introduction

In this chapter, the results of the study are summarized. Thanks to popularity of surface patterning for the creation of micromixers and mixing enhancement within microfluidics, FFF process may be a simple and effective way for making micromixers. Experimental and numerical studies are employed to show the effects of the extruded width (LW), distance between adjacent filaments (b), and filament height ( $h_1$ ) are investigated on the mixing performance and enhancing mixing in the fabricated devices. The effect of material, 3D printer, and flow rate on the mixing process in microfluidic devices are addressed. The performance of FFF printed devices are compared with SLA and Polyjet devices. In the last part of the chapter, the fabricated chip for lysis and DNA extraction processes are introduced and tested with the solutions.

## 4.2 The Effect of Extruded Width on Mixing

In chapter 3, a set of printing parameters were introduced that effect on the fluidic behavior inside FFF-printed devices. These parameters are including: the cross-sectional shape of the deposited filaments which refers to the width of extruded filament and layer thickness, infill orientation, and the gaps in the vertical and horizontal directions. A simple Y-shaped microchannel was designed as shown in Figure 4-1 and fabricated using FFF method to study the effect of extruded filament on fluid behavior and in general, using the limitations of FFF for enhancing mixing. The simple Y- shaped microchannel help to investigate the mixing that occurred only by using the limitations of the FFF process.

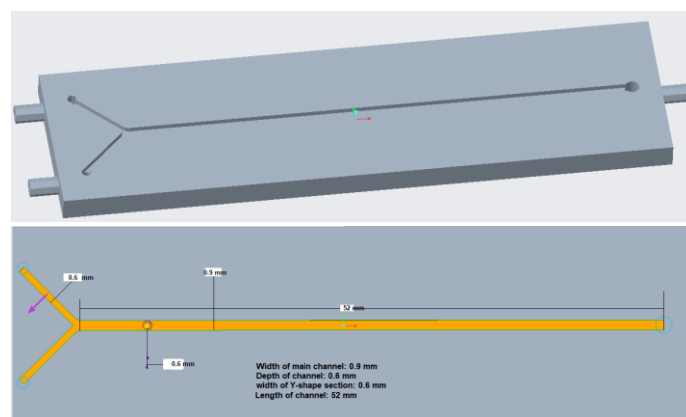


**Figure 4-1.** 3D CAD model of simple Y-shaped micromixer with dimensions in mm.

First, four devices with setting different values in slicer software for the line width (width of the extruded filament) were fabricated by starting from 200  $\mu\text{m}$  up to 800  $\mu\text{m}$ , with equally spaced line widths. The other parameters kept constant, and the layer height of the extruded filament was 100  $\mu\text{m}$  for all the micromixers. The micromixers were fabricated using Ultimaker 3 printer. The four devices were as below:

- 1) The device with a line width of 200  $\mu\text{m}$ , and layer height of 100  $\mu\text{m}$
- 2) The device with a line width of 400  $\mu\text{m}$ , and layer height of 100  $\mu\text{m}$
- 3) The device with a line width of 600  $\mu\text{m}$ , and layer height of 100  $\mu\text{m}$
- 4) The device with a line width of 800  $\mu\text{m}$ , and layer height of 100  $\mu\text{m}$

After printing, the performance of devices in mixing two fluids were tested at flow rates of 10  $\mu\text{L}/\text{min}$ , 50  $\mu\text{L}/\text{min}$ , 200  $\mu\text{L}/\text{min}$ , and 400  $\mu\text{L}/\text{min}$ . Two different water solutions stained with yellow and blue dye were injected using syringe pumps. Two different fluids have different colors: one is blue and the other yellow. This is important for the colorimetric analysis; when the colors in the images are changing, it means that the fluids are mixing. The tests were conducted by setting the equal flow rate in both syringe pumps, waiting to allow the fluids to reach together at junction, and pass through the main channel. To analyze the mixing, the images taken by detection system for each different device and flow rates used for the colorimetric analysis through Matlab. Figure 2-4 shows the photographs taken by detection system at different flow rates for device number 4 (line width of 800  $\mu\text{m}$ ).

For the device with a line width greater than 800  $\mu\text{m}$ , the leakage occurred at flow rates higher than 200  $\mu\text{L}/\text{min}$  as shown in Figure 4-2. This means that the gap between two extruded filaments in the horizontal direction is high which can cause leakage at higher flow rates. However, the leakage not observed for other printed devices at high flow rates and therefore, these devices are considered for further studies.

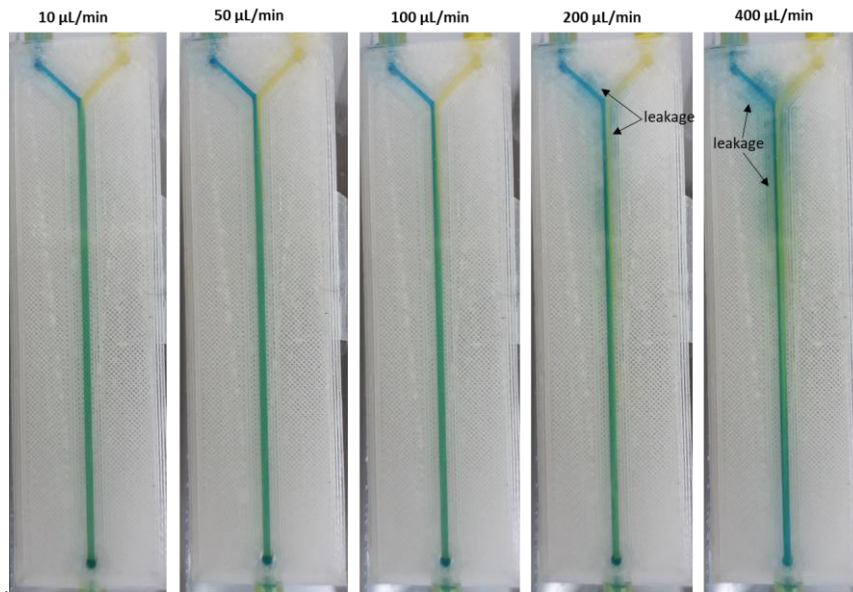


**Figure 4-2.** Captured images at different flow rates from the top of the device with a line width of 800  $\mu\text{m}$ .

The actual dimensions of the fabricated channels are different from the designed CAD model in FFF process. In this study, the fabricated microchannels are scanned using a high precision Conoscan scanner to measure the actual parameters of ridges on the bottom of microchannels. Figure 3-4 shows the measured dimensions for each single printing path and the distance between deposition passes. The results are reported in Tables 4-1, 4-2, and 4-3 for three devices.

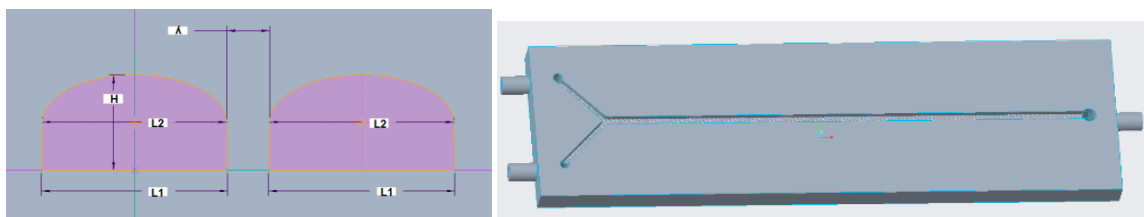


**Figure 4-3.** Left: Schematic showing the cross section of the extruded filaments on the bottom of channels; Right: 3D model of device 1 (line width: 200  $\mu\text{m}$ ) with actual parameters for the ridges.

**Table 4-1.** Measured values for the fabricated microchannel with a nominal line width of 200  $\mu\text{m}$ .

Nozzle diameter: 0.25 mm, Layer height: 0.1 mm				
Parameters	L1	L2	H	$\lambda$
Values ( $\mu\text{m}$ )	196	194	100	45

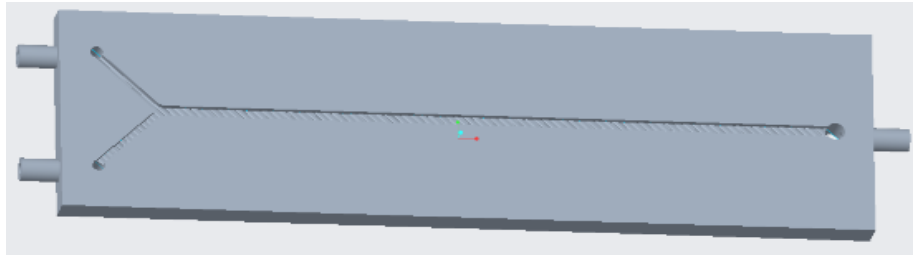


**Figure 4-4.** 3D model of device 2 (line width: 400  $\mu\text{m}$ ) with actual parameters for the ridges.

**Table 4-2.** Measured values for the fabricated microchannel with a nominal line width of 400  $\mu\text{m}$ .

Nozzle diameter: 0.4 mm, Layer height: 0.1 mm				
Parameters	L1	L2	H	$\lambda$
Values ( $\mu\text{m}$ )	392	388	100	100

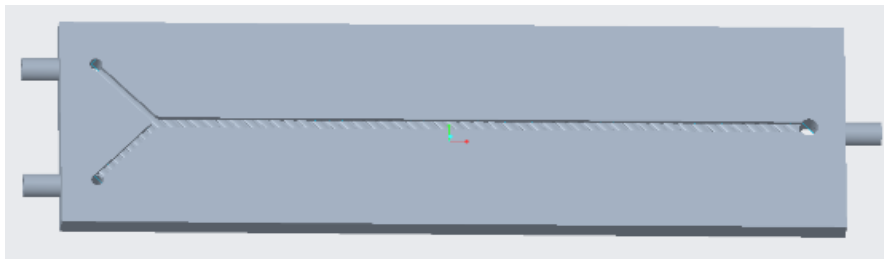


**Figure 4-5.** 3D model of device 3 (line width: 600  $\mu\text{m}$ ) with actual parameters for the ridges.

**Table 4-3.** Measured values for the fabricated microchannel with a nominal line width of 600  $\mu\text{m}$ .

Nozzle diameter: 0.4 mm, Layer height: 0.1 mm				
Parameters	L1	L2	H	$\lambda$
Values ( $\mu\text{m}$ )	588	582	100	200

To compare the efficiency of the mixing for three micromixers, the captured images were analyzed using colorimetric analysis algorithm explained in section 3.2.3. A set of 20 regions of interests (ROIs) are considered at regular intervals along the length of the microchannels and the length of the required channel for complete mixing are investigated for each device. To determine the point with the maximum mixing, mean square errors (MSE) were calculated for each ROI. The ROI with minimum MSE among different ROIs select as the point with

maximum mixing. For example, Figure 4-6 shows the calculated MSE for 20 different ROIs in printed micromixer with a line width of 200  $\mu\text{m}$  and flow rate of 200  $\mu\text{L}/\text{min}$ . The ROI number 17 considered the point with complete mixing. In other words, after this point, 90% of the fluids are mixed and there is a uniform flow with green color.

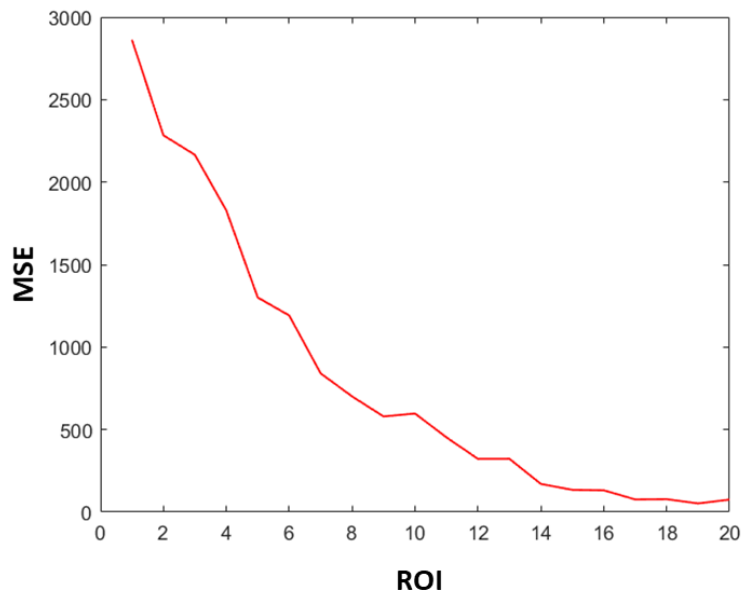


**Figure 4-6.** Calculated Mean Square Error (MSE) for each ROI in printed device with a line width of 200  $\mu\text{m}$ .

The following figures are the results of colorimetric analysis for printed devices at different flow rates.

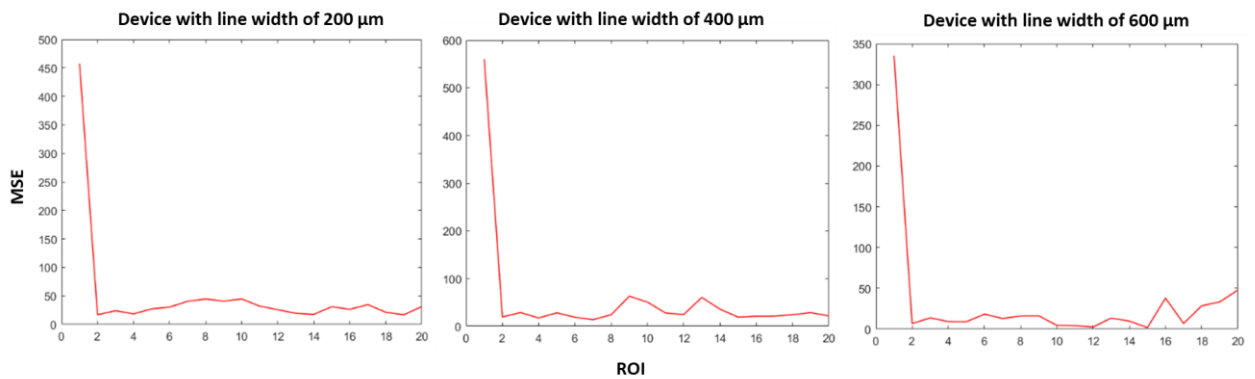


**Figure 4-7.** Calculated Mean Square Error (MSE) for three printed devices at flow rate of 10  $\mu\text{L}/\text{min}$ .

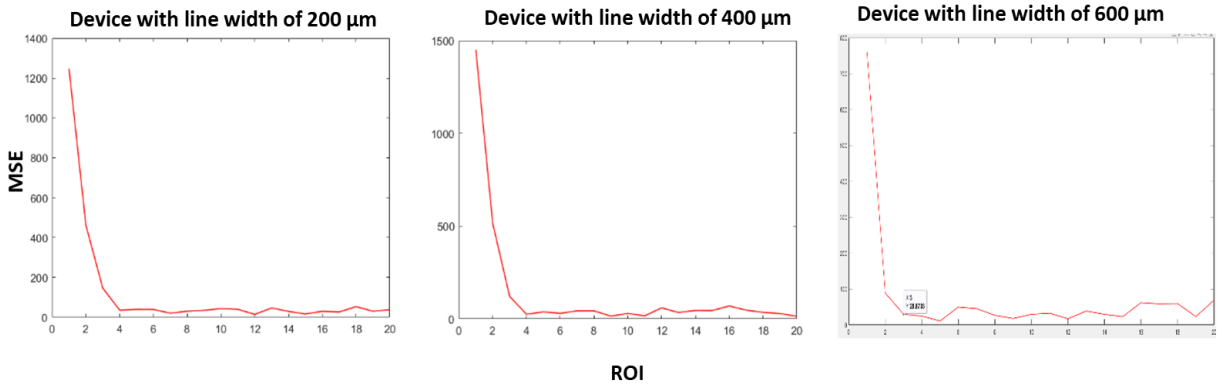


**Figure 4-8.** Calculated Mean Square Error (MSE) for three printed devices at flow rate of 50  $\mu\text{L}/\text{min}$ .

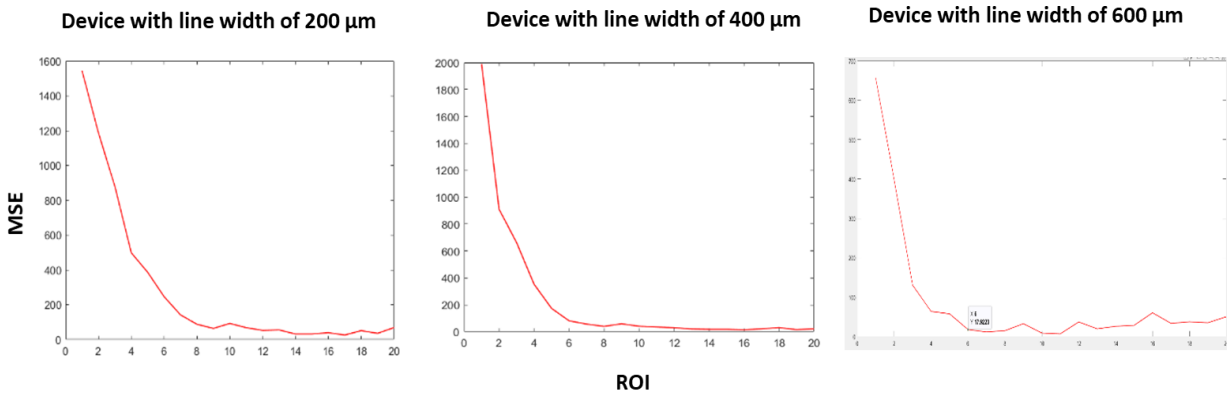


**Figure 4-9.** Calculated Mean Square Error (MSE) for three printed devices at flow rate of 100  $\mu\text{L}/\text{min}$ .

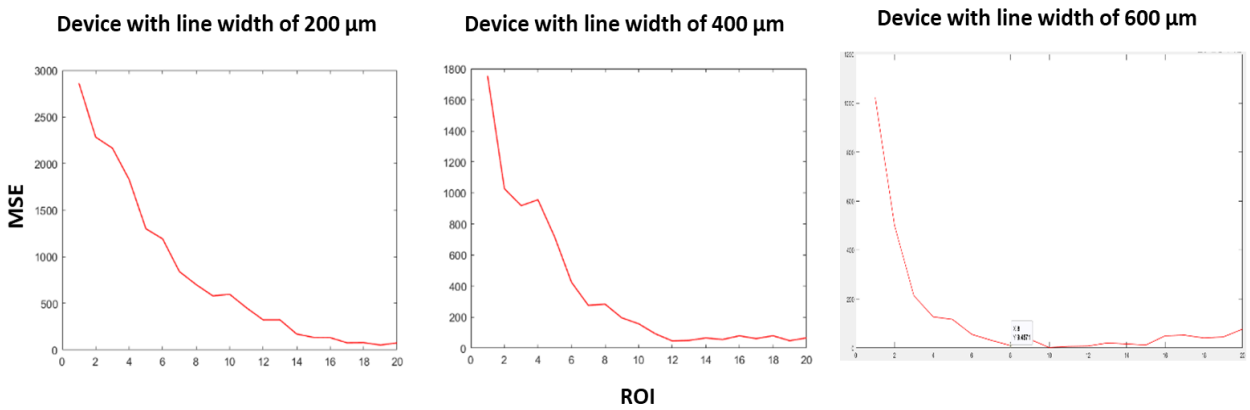


**Figure 4-10.** Calculated Mean Square Error (MSE) for three printed devices at flow rate of 200  $\mu\text{L}/\text{min}$ .

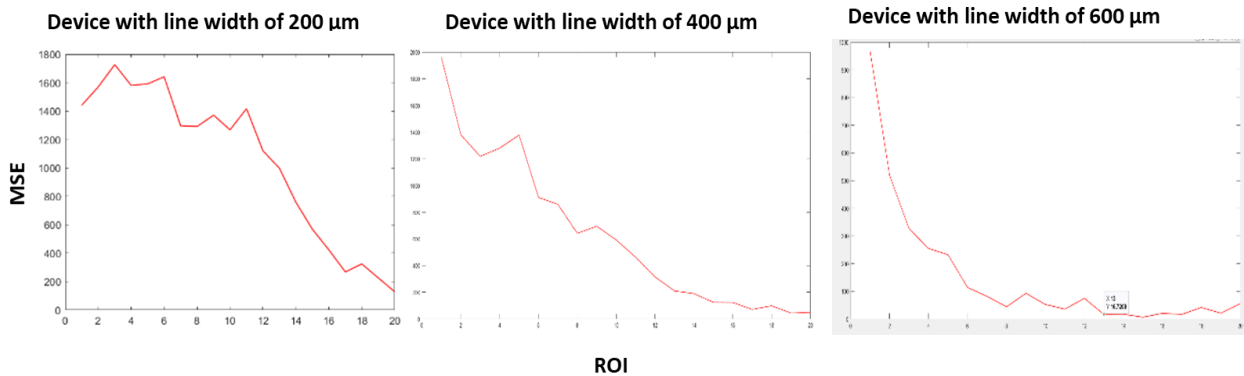


**Figure 4-11.** Calculated Mean Square Error (MSE) for three printed devices at flow rate of 400  $\mu\text{L}/\text{min}$ .

The above results are summarized in Table 4-4, with relevant Reynolds number and the velocity in the main channel. The results show that by increasing the flow rate in each micromixer, the required length to achieve complete mixing needs to be increased. These results are consistent with other studies [101, 125]. By increasing the line width from 200  $\mu\text{m}$  to 600  $\mu\text{m}$ , the complete mixing occurs faster at the same flow rate. However, these differences are negligible at a low flow rate (10  $\mu\text{L}/\text{min}$ ); complete mixing occurs immediately after collision of two flows in the first of main channel after Y junction.

It is known that FFF suffers from some critical issues such as lower resolution which is limited by the nozzle diameter and drive system [81]. However, when the subject is using these limitations in a process like mixing inside microfluidics, the effect of other parameters such as printer and materials also should be considered. It should be noted that the resolution of 3D printer can also have a direct impact on the resulting surface roughness. The channel surface of a device printed with a high-resolution printer is smoother than devices printed with a low-resolution printer. On the other hand, the transparency of printed devices is a vital point in the fabrication of microfluidic devices. To investigate the effect of these factors on fabrication of micromixers and analyze the performance of micromixers, the next design of experiments is suggested.

**Table 4-4.** Mixing performance of three printed devices with different extruded width.

Devices Parameters	Micromixer with a line width 200 $\mu\text{m}$					Micromixer with a line width 400 $\mu\text{m}$					Micromixer with a line width 600 $\mu\text{m}$				
	10	50	100	200	400	10	50	100	200	400	10	50	100	200	400
Flow rates at two inlets ( $\mu\text{L}/\text{m}$ )	10	50	100	200	400	10	50	100	200	400	10	50	100	200	400
Velocity in the main channel (m/s)	$0.62 \times 10^{-3}$	$3.08 \times 10^{-3}$	$12.34 \times 10^{-3}$	$24.7 \times 10^{-3}$	$49.4 \times 10^{-3}$	$0.62 \times 10^{-3}$	$3.08 \times 10^{-3}$	$12.34 \times 10^{-3}$	$24.7 \times 10^{-3}$	$49.4 \times 10^{-3}$	$0.62 \times 10^{-3}$	$3.08 \times 10^{-3}$	$12.34 \times 10^{-3}$	$24.7 \times 10^{-3}$	$49.4 \times 10^{-3}$
Re	0.44	2.2	8.87	17.75	35.5	0.44	2.2	8.87	17.75	35.5	0.44	2.2	8.87	17.75	35.5
$L_{\text{mix}}$ (ROI number)	2	4	14	17	Incomplete	2	4	8	12	19	2	3	6	8	13

### 4.3 The Effect of the Material and Printer

#### 4.3.1 Design of Experiments

The designed micromixer in Figure 4-1 was used for the new study. The process variables are line width, machine (3D printer), material transparency, and flow rate; each in two levels (see Table 4-5). The response variable is the required length for the complete mixing. The levels are selected based on the results in the previous study.

**Table 4-5.** Factors and levels.

Factor	Level	
	-1	+1
Line width (LW)	200 $\mu\text{m}$	600 $\mu\text{m}$
Flow rate	50 $\mu\text{L}/\text{min}$	100 $\mu\text{L}/\text{min}$
Material	Transparent PLA	Translucent PLA
Machine	Ultimaker 3	Ultimaker S5

Table 4-6 shows the proposed design for experiments. A full factorial design ( $2^4$ ) with two replications was performed for each combination. To eliminate or reduce the effect of any noise, two replicates used in the design. There is no need for repetition since an algorithm was used for analyzing the mixing performance to reduce labor's errors however, it is needed to have a uniform lighting for detection system in all the tests.

### Full Factorial Design

Factors: 4 Base Design: 4, 16  
 Runs: 32 Replicates: 2  
 Blocks: 1 Center pts (total): 0

Table 4-6. Proposed design of experiments.

StdOrder	RunOrder	CenterPt	Blocks	line width	flow rate	material	machine
1	1	1	1	0.2	50	1	1
11	2	1	1	0.2	100	1	2
7	3	1	1	0.2	100	2	1
27	4	1	1	0.2	100	1	2
14	5	1	1	0.6	50	2	2
8	6	1	1	0.6	100	2	1
31	7	1	1	0.2	100	2	2
4	8	1	1	0.6	100	1	1
19	9	1	1	0.2	100	1	1
22	10	1	1	0.6	50	2	1
9	11	1	1	0.2	50	1	2
12	12	1	1	0.6	100	1	2
32	13	1	1	0.6	100	2	2
26	14	1	1	0.6	50	1	2
17	15	1	1	0.2	50	1	1
29	16	1	1	0.2	50	2	2
10	17	1	1	0.6	50	1	2
20	18	1	1	0.6	100	1	1
23	19	1	1	0.2	100	2	1
24	20	1	1	0.6	100	2	1
13	21	1	1	0.2	50	2	2
25	22	1	1	0.2	50	1	2
2	23	1	1	0.6	50	1	1
21	24	1	1	0.2	50	2	1
6	25	1	1	0.6	50	2	1
28	26	1	1	0.6	100	1	2
18	27	1	1	0.6	50	1	1
15	28	1	1	0.2	100	2	2
3	29	1	1	0.2	100	1	1
5	30	1	1	0.2	50	2	1
16	31	1	1	0.6	100	2	2
30	32	1	1	0.6	50	2	2

\* Transparent PLA=1, Translucent PLA =2, UM 3=1, UM S5=2

In the previous tests, the fabricated devices with a line width greater than 600  $\mu\text{m}$  showed leakage at flow rates higher than 200  $\mu\text{L}/\text{min}$ . Therefore, 200 and 600  $\mu\text{m}$  were selected as the low and high levels of the line width parameter (Figure 4-12). The infill line distance (horizontal gap) for devices printed with a 0.25 mm nozzle and a 0.4 mm nozzle was set to 0.2 mm and 0.6 mm, respectively, meaning that the two adjacent filaments were tangent to each other. The micromixers were printed using two different printers, the Ultimaker 3 and the Ultimaker S5. Two different types of polylactic acid (PLA) filament with a 2.85 mm diameter were used: (i) transparent PLA and (ii) translucent PLA. Flow rates of 50 and 100  $\mu\text{L}/\text{min}$  were selected as the two levels (low to medium fluid velocities) for the flow rate factor. The fixed printing parameters during the tests are reported in Table 4-7. Figure 4-13 shows photographs of two different fabricated channels with line widths of 200 and 600  $\mu\text{m}$  under the microscope.

**Table 4-7.** Fixed printing parameters during the experiments.

Printing Parameter	Nozzle 0.25 mm	Nozzle 0.4 mm
Printing temperature ( $^{\circ}\text{C}$ )	190	200
Printing speed (mm/s)	30	70
Layer height ( $\mu\text{m}$ )	100	100
Filament orientation ( $^{\circ}$ )	60	60
Flow (%)	100	100
Infill line distance (mm)	0.2	0.6
Build temperature	60	60

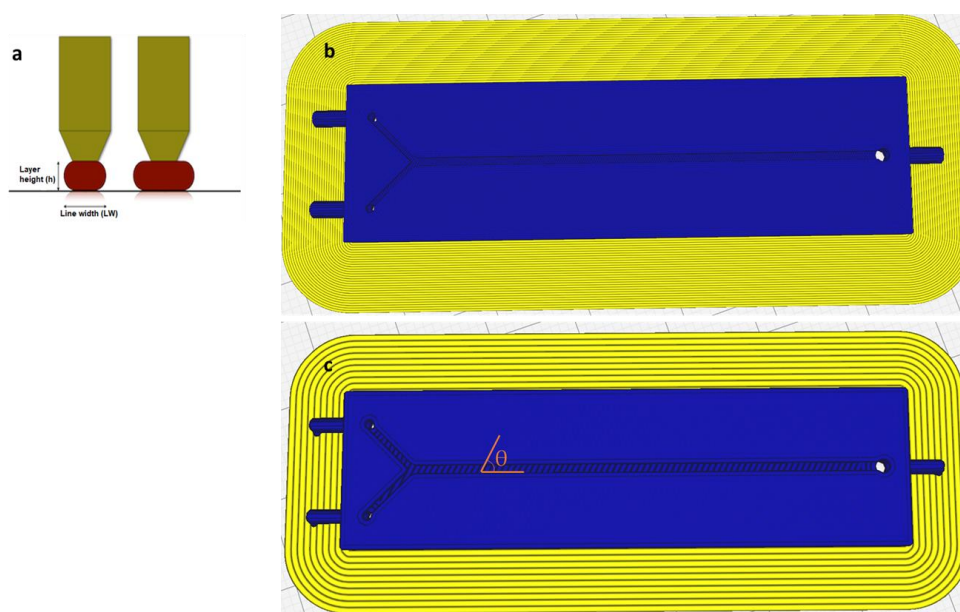


**Figure 4-12.** Printing parameters. (a) The geometry of extruded filament, (b) and (c) show the movement path of printing nozzles with two different infill line widths 200 and 600  $\mu\text{m}$ , respectively. The angle  $\theta$  denotes the orientation of the extruded filament relative.

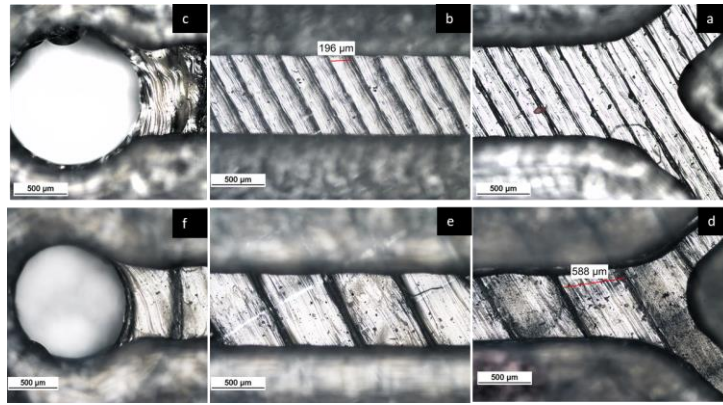


**Figure 4-13.** Photographs of two different fabricated channels. Top- device with nominal line width 200  $\mu\text{m}$ , at first (a), middle (b), and end of channel (c). Bottom- device with nominal line width 600  $\mu\text{m}$ , at first (d), middle (e), and end of channel (f).

### 4.3.2 Experiments and results

Two water streams were introduced into the Y-shaped microfluidic micromixers, with yellow and blue food dyes like previous tests to distinguish one stream from the other. A set of 40 ROIs are considered at regular intervals along the channels. In Table 4-8, the analyzed results of different combinations in full factorial design are summarized. The results are the performance of FFF printed micromixers at two different Reynolds numbers ( $Re = 2.2$  and  $Re = 8.87$  for flow rates 50  $\mu\text{L}/\text{min}$  and 100  $\mu\text{L}/\text{min}$ , respectively). The results show the effect of different factors and levels on the required channel length for achieving complete mixing.

**Table 4-8.** The performance of mixing in each FFF printed micromixer; evaluated by colorimetric analysis.

Run Number	A (Line width)	B (Flow rate)	C (Material)	D (Machine)	Run Label	Length of Mixing (ROI)	
						n1	n2
1	-1	-1	-1	-1	(1)	12	10
2	+1	-1	-1	-1	a	10	7
3	-1	+1	-1	-1	b	22	19
4	+1	+1	-1	-1	ab	18	16
5	-1	-1	+1	-1	c	11	10
6	+1	-1	+1	-1	ac	8	7
7	-1	+1	+1	-1	bc	21	18
8	+1	+1	+1	-1	abc	16	13
9	-1	-1	-1	+1	d	9	10
10	+1	-1	-1	+1	ad	7	9
11	-1	+1	-1	+1	bd	13	16
12	+1	+1	-1	+1	abd	14	13
13	-1	-1	+1	+1	cd	9	10
14	+1	-1	+1	+1	acd	9	10
15	-1	+1	+1	+1	bcd	20	16
16	+1	+1	+1	+1	abcd	15	18

Minitab 17 was used for statistical analysis of the results. Analysis of variance can be considered as the most useful statistical method, which is a good method for evaluating equality of several means. Before the conclusions from the analysis of variance are adopted, the adequacy of the underlying model was checked. The primary diagnostic tool is residual analysis. To check the adequacy of the model, the histogram plot of residuals as well as the normal probability plot of residuals were used. As shown in the Figure 4-14, the histogram of the residuals is similar to the normal distribution and centered around the value of zero. The normal probability plot is illustrated as a straight line, indicating the normality of the data. The plotting data versus order (experiment order) can be also useful in identifying correlation between residuals. The presence of positive and negative sequences indicates a positive correlation between residuals as shown in the Figure 4-14. Finally, by plotting the residuals versus fits, the residuals should be unstructured and should not have any relationship with other variables including the predicted response.

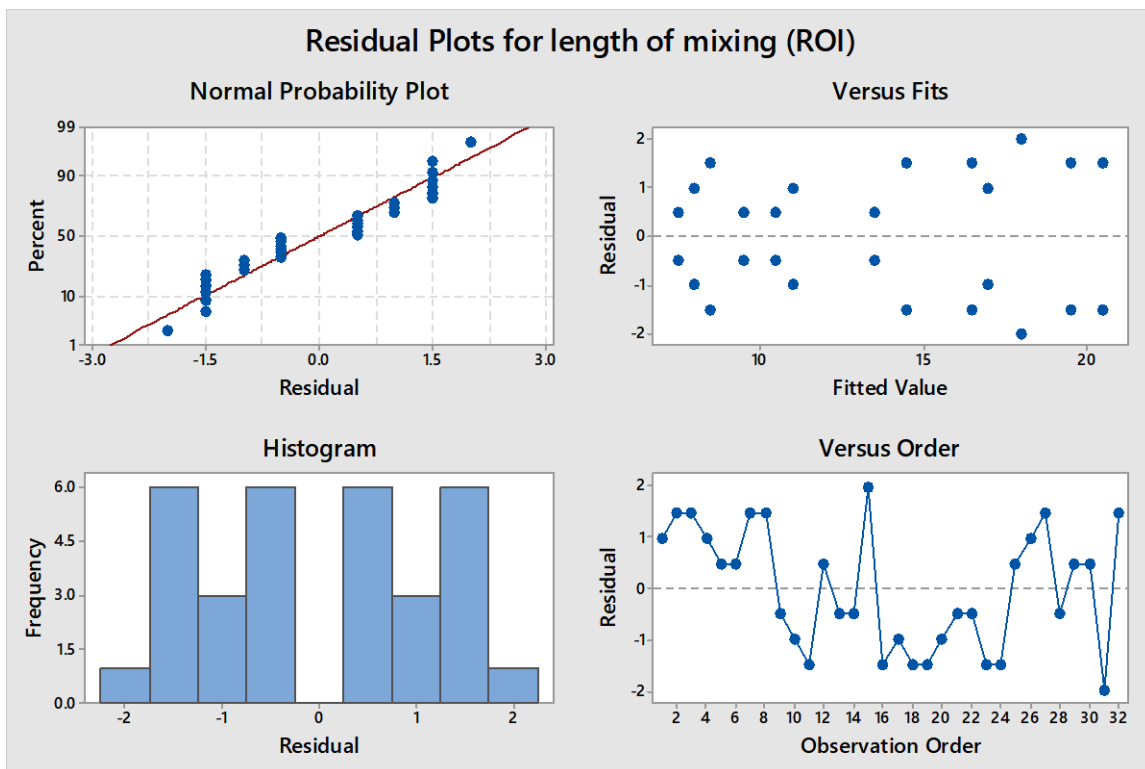


**Figure 4-14.** Residual plots for length of mixing.

The main and interaction effects for the length of mixing are shown in Figure 4-15. Achieving complete mixing over a short time and length of channel is one of the main challenges in microfluidic micromixers.

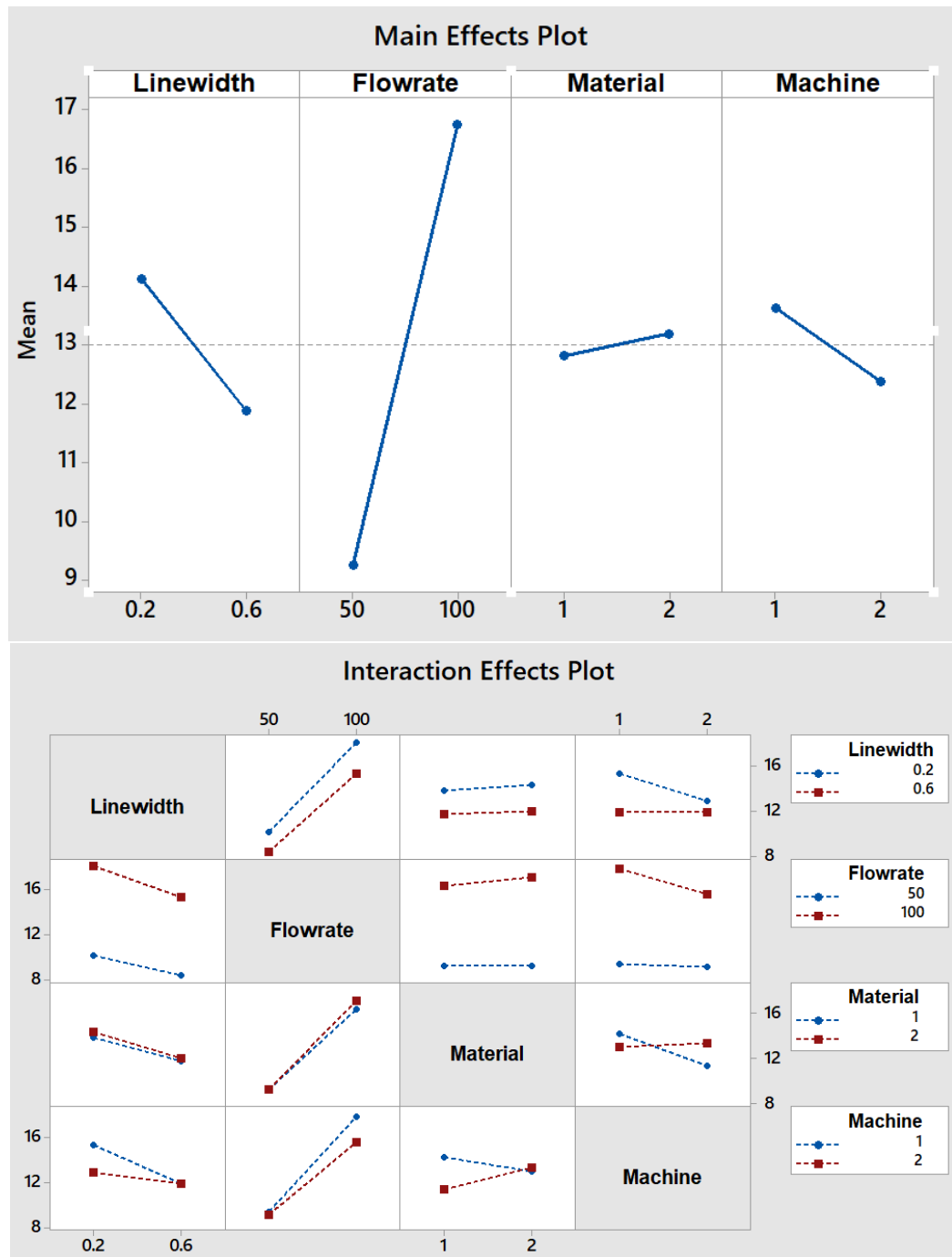


Figure 4-15. Main and interaction effects plots for the length of mixing.

Several results can be drawn from plots of the main and interaction effects:

- 1) The flow rate is the factor with the greatest effect on the length of mixing. With an increase in the flow rate from 50 to 100  $\mu\text{L}/\text{min}$ , the required length for complete mixing was increased in all fabricated micromixers, which is consistent with other studies [101, 125]. As shown in the Pareto chart and Table 4-9, the interaction effects of this factor are insignificant. Figure 4-16 shows the Pareto chart of the standardized effects, while in Table 4, the effects (non-standardized) and respective T values and P values ( $\alpha = 0.05$ ) for each factor and their interaction effects are summarized.

**Table 4-9.** Non- standardized effects, T and P values in factorial design.

Factor / n way interactions	Effect	T-value	P-value
A	-2.25	-3.84	0.001
B	7.50	12.79	0.000
C	0.375	0.64	0.531
D	-1.25	-2.13	0.049
A*B	-0.50	-0.85	0.406
A*C	-0.125	-0.21	0.834
A*D	1.25	2.13	0.049
B*C	0.375	0.64	0.531
B*D	-1.00	-1.71	0.107
C*D	1.625	2.77	0.014
A*B*C	-0.375	-0.64	0.531
A*B*D	0.25	0.43	0.675
A*C*D	0.375	0.64	0.531
B*C*D	0.875	1.49	0.155
A*B*C*D	-0.125	-0.21	0.834

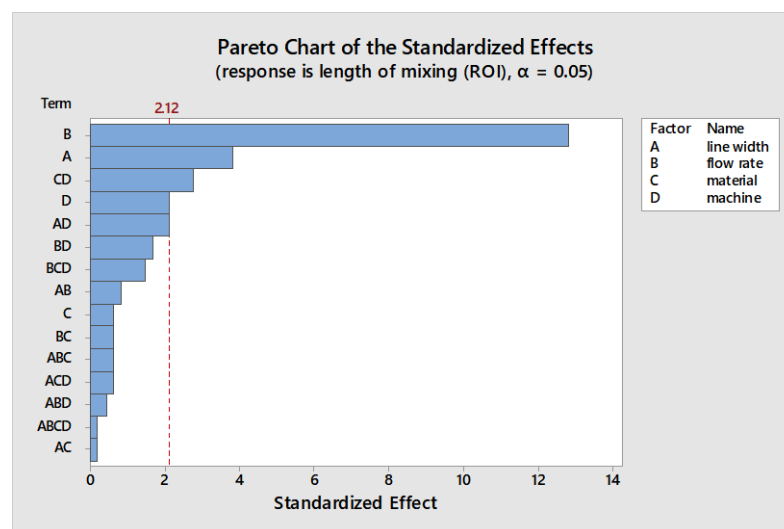


**Figure 4-16.** Pareto chart of standardized effects.

- 2) Fabricated micromixers with an extrusion line width of 600  $\mu\text{m}$  showed a better mixing performance than devices printed with a line width of 200  $\mu\text{m}$ , where the average required length for complete mixing is decreased. However, the interaction effects of line width are negligible (see Figure 4-16 and Table 4-9).
- 3) The effect of material on the length of mixing is negligible due to the equal level of hydrophobicity for the materials used. The surface of PLA is strongly hydrophobic [129], and the use of hydrophobic surfaces is one of the topics of interest topics for mixing enhancement in microfluidic systems [35, 36]. Although, the effect of the material was insignificant on the mixing process, the transparency of printed devices is another vital point in the fabrication of microfluidic devices. Examples of the printed micromixers with translucent and transparent PLA are shown in Figure 4-17. The devices printed with translucent PLA were often opaque, rendering optical analysis challenging. The semi-transparency of the printed device with the transparent PLA allows imaging with back illumination [125].

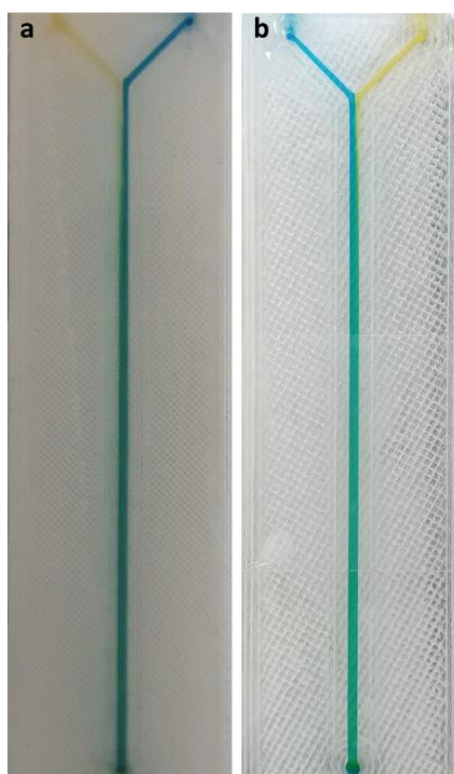


**Figure 4-17.** Full top view of 3D printed microfluidic devices, demonstrating transparency: (a) translucent PLA; (b) transparent PLA.

4) Using different printers can cause different results due to the different accuracy of the printers. The two printers used in this study had a slight effect on the required length of mixing (see Figure 4-15). In general, the printed channels in the FFF process are consistently smaller than the CAD model, due to the spreading of the polymer as it is extruded [101]. For this, the mixers printed with the Ultimaker S5 had a better mixing performance, as its higher accuracy allowed the printing channels to be closer to the designed model. Among the different interaction effects, the effect of C\*D (material\*machine) is significant (see Table 4-9). A probable explanation is related to the ability of the machines to print different materials. While the results for the printed mixers with the translucent PLA were somewhat similar in two printers, the fabricated mixers with the transparent PLA had different performances when printed with two different printers (see interaction effects plot in Figure 4-15).

The following statistical results shows the updated analysis of variance with a regression model for predicting required length of mixing. A model for predicting the required channel length for complete mixing with regard to the extruded line width and flow rate is shown in Figure 4-18.

Coded Coefficients

Term	Effect	Coef	SE Coef	T-Value	P-Value	VIF
Constant		13.000	0.283	45.87	0.000	
line width	-2.250	-1.125	0.283	-3.97	0.001	1.00
flow rate	7.500	3.750	0.283	13.23	0.000	1.00
material	0.375	0.187	0.283	0.66	0.514	1.00
machine	-1.250	-0.625	0.283	-2.21	0.037	1.00
line width*machine	1.250	0.625	0.283	2.21	0.037	1.00
material*machine	1.625	0.812	0.283	2.87	0.008	1.00

Regression Equation in Uncoded Units

$$\text{length of mixing} = 16.37 - 15.00 \text{ line width} + 0.1500 \text{ flow rate} - 4.50 \text{ material} - 8.62 \text{ machine} + 6.25 \text{ line width*machine} + 3.25 \text{ material*machine}$$

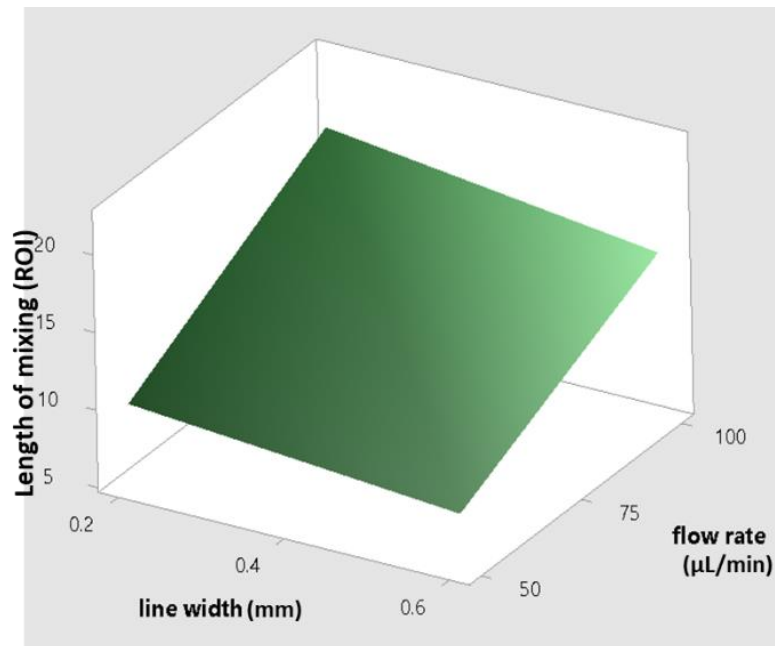


**Figure 4-18.** Surface plot for predicting the length of mixing versus different line width and flow rates.

These results showed that the ridges on the bottom of the channels can affect the fluidic behavior and enhance the “poor” mixing performance which is identified as a challenge in microfluidic micromixers. In this study, the devices with a greater extruded line width (600  $\mu\text{m}$ ) printed with bot machines and materials, showed better mixing efficiency. While, in the devices printed with an extruded line width equal to 200  $\mu\text{m}$ , a longer length of channel is needed for complete mixing. This means that without considering the effects of machine and material, a greater groove or ridge can help for better mixing. Inside a single groove, the lateral displacements expand by increasing the gap between two ridges. Layer height is the other parameter which can control the air gap between two paths. However, an increasing in the layer height above 100  $\mu\text{m}$  increase also the gaps in the vertical direction between the layers. The presence of gaps can cause fluids to leak into the chip at high flow rates. In the following, the experimental and numerical studies were conducted to investigate the effect of the extruded filaments as well as layer thickness on the flow behavior.

## 4.4 Experimental-Numerical Study

### 4.4.1 Fabrication

The 3D CAD model of micromixer showed in Figure 1-4. New devices were printed using the Ultimaker S5 printer with two different nozzles; 0.25 mm nozzle for devices fabricated with infill line width 200  $\mu\text{m}$  and 0.4 mm nozzle for devices with infill line width 600  $\mu\text{m}$ . To study the effect of the different patterned ridges made by FFF on the fluidic behavior, at first two different channels were fabricated with different nominal values adjusted in the slicing software for the ridge parameters (Table 4-10). For each design, two devices (n=2) were fabricated to reduce the errors related 3D printer and testing of micromixers. Fixed printing parameters during the tests are mentioned in appendix A. Figure 4-19 shows photographs of the two fabricated channels.

**Table 4-10.** Nominal values of ridge parameters and the measured values of these parameters after fabrication (actual parameters)

Channel Parameters	Nominal Values		Measured Values	
	Channel 1	Channel 2	Channel 1	Channel 2
	1	2	1	2
LW – line width, $\mu\text{m}$	200	600	$196 \pm 2$	$588 \pm 2$
$h_1$ - filament height, $\mu\text{m}$	100	100	$100 \pm 2$	$100 \pm 2$
b – ridge distance, $\mu\text{m}$	0	0	$45 \pm 2$	$200 \pm 2$



**Figure 4-19.** Two printed channels. Left: channel 1 with a line width of 200  $\mu\text{m}$ ; Right: channel 2 with a line width of 600  $\mu\text{m}$ .

#### 4.4.2 Experimental setup

The ridge parameters and the average air gap between adjacent filaments were measured for all fabricated devices using Conoscan scanner (Table 4-10). For all devices, the infill orientation was adjusted at  $60^\circ$  relative to the fluid flow, which results in better mixing performance [118]. For all the previous tests, the water-based solutions were used where, different dyes were added to water in order to distinguish one stream from the other one. However, for numerical study, the diffusion coefficient ( $D$ ) for these solutions is not known. For this, Methylene blue and deionized (DI) water streams were introduced into the Y-shaped microfluidic mixers where 0.13 gr of Methylene blue dissolved in 20.01 gr of DI water and DI water were prepared as described in chapter 3. Two different streams were injected using two syringe pumps equipped with 5 mL disposable syringes at 5, 10, 20, 40, 80, and 150  $\mu\text{L}/\text{min}$ . Low to medium velocities were tested thanks to the effect of ridges at lower velocities. Figure 4-20 shows two different print paths for the channels (a and b) with images showing the fabricated devices in c and d, respectively.

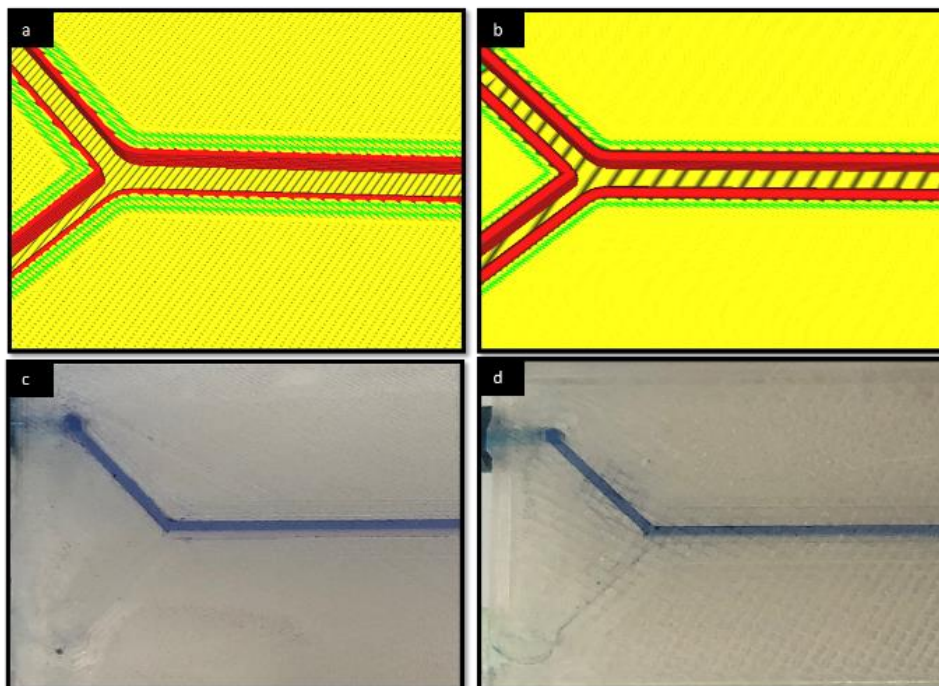


**Figure 4-20.** (a) and (b) are schematic showing the movement path of printing nozzle with two different infill line width (200 and 600  $\mu\text{m}$ ). (c) and (d) are photographs of the fabricated micromixers filled with methylene blue and DI water.

To characterize the mixing behavior in the microfluidic channels, methylene blue dissolved in DI water and DI water streams were injected into each inlet of the Y-shaped microfluidic mixers (Figure 4-21). The fluid behavior of printed devices is evaluated by analyzing captured images taken from different channels at different flow rates. The mixing performance was measured using a colorimetric approach. For the colorimetric analysis a set of 20 rectangular regions of interest (ROIs) was considered at regular intervals perpendicular to the main channel to obtain the change in color intensity across the channel.

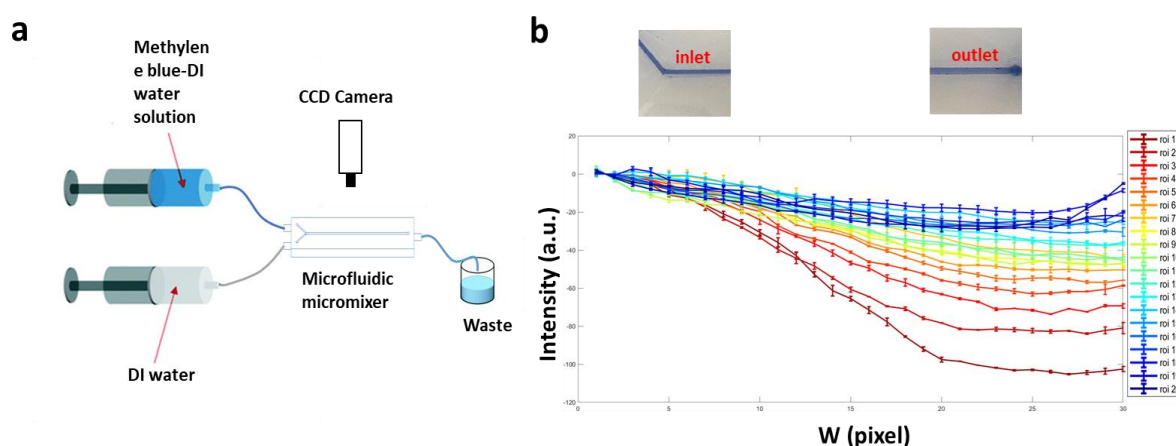


**Figure 4-21.** (a) Experimental setup for measuring mixing performance in microfluidic channel. (b) standard deviation of the intensities at different region of interest. At the first of the main channel since the fluids are not mixed yet, the curves have two peaks. The curves corresponding to the last ROIs tend to be flat and it means two fluids are mixed.

#### 4.4.3 Experimental and numerical results

As shown in Figure 4-22, channel 2 with extrusion width 588  $\mu\text{m}$  and ridge distance equal to 200  $\mu\text{m}$ , showed higher mixing efficiency for all flow rates; MSE decreased (mixing efficiency increased) as a function of channel length (ROI). For a low flow rate of 5  $\mu\text{L}/\text{min}$ , which corresponds to a  $\text{Re}$  of 0.22, both channels showed complete mixing. However, the length of complete mixing was at ROIs 15 (equal to 39 mm, the distance between each ROI is 2.6 mm) and 9 (23.4 mm) for channel 1 and channel 2, respectively. With an increase in flow rate, the required length for complete mixing was increased in both channels, which is consistent with other studies [28, 101, 125]. At 20  $\mu\text{L}/\text{min}$  ( $\text{Re}=0.89$ ), complete mixing was observed at a channel length of 49.4 mm from the Y-junction in channel 2. In contrast, mixing has only been

partially achieved at the outlet of channel 1 (blue curve). The typical difference between the two channels was observed at the beginning of each channel, where mixing efficiency was increased immediately when two streams met after Y-junction in channel 2 (Figure 4-20). This can be explained by considering the transverse movement of fluids induced by obliquely patterned ridges, which are the result of extruded filaments by FFF. The lateral displacements generate a helical flow along the axis of flow and enhance mixing, as described in [27, 30]. The lateral displacement length inside a single groove is determined by its width and depth. When two fluids passed over the first ridge in channel 1, a slight change occurs in the positions of streams relative to the initial positions, which is due to a small gap between two ridges (Figure 4-23). Inside a single groove in SGM mixer, the lateral displacements expand with increasing groove width, but no significant change is detected for values more than 200  $\mu\text{m}$  ( $b \geq 200$ ) [32]. The designed groove width values for two fabricated channels meet the critical value in the SGM mixers.

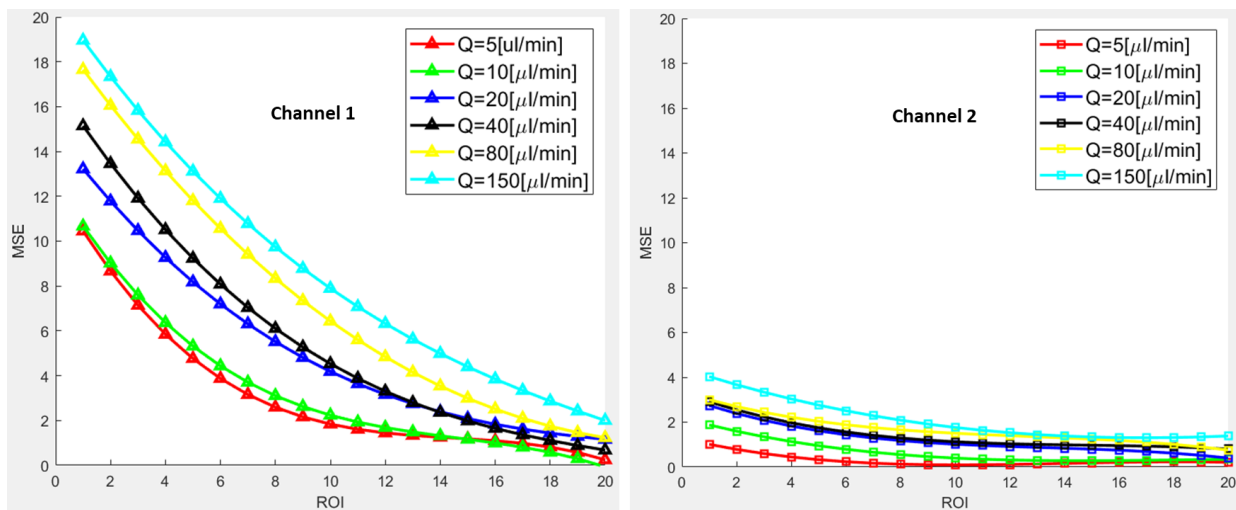


**Figure 4-22.** The extent of fluid mixing for different ridge topographies in channel 1 and channel 2.

These experimental observations were supported by CFD results (COMSOL software) shown in Figure 4-23. The velocity field and concentration distributions of the fluid layers confirm the transverse movement of fluid from one side to the other side of channel 2 (Figure 4-23a, b-bottom). The cross-movement clearly aids in chaotic advection over the ridges and folding the fluid material, which leads to an increased contact area between the solutions to be mixed (Figure 4-23c, bottom); therefore, enhance mixing in the microchannel. However, these cross

movements are negligible in channel 1 (Figure 4-23a, b-top), which can lead to a slight change in the stream's position. Mixing occurred at the boundary of two fluids, where the only mechanism for mixing is diffusion (Figure 4-23c, top).

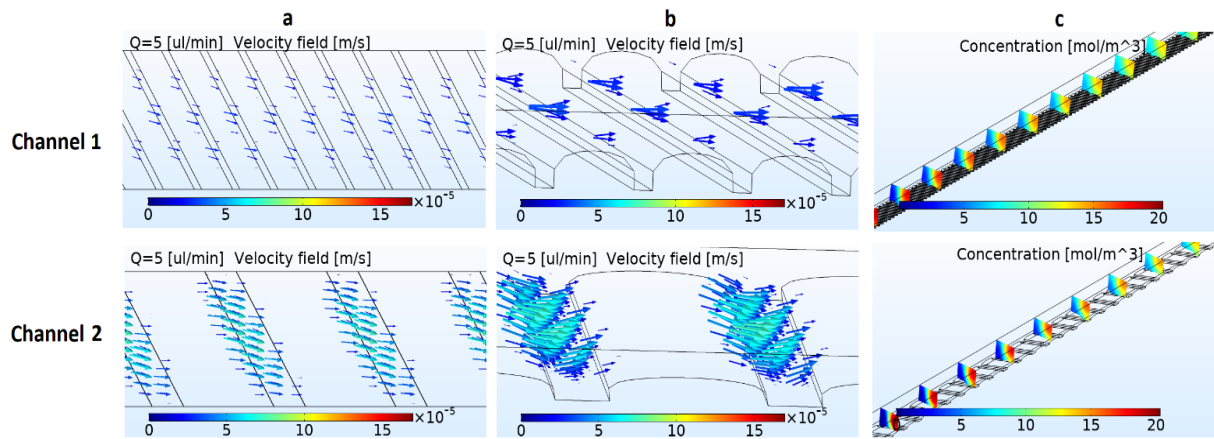


**Figure 4-23.** CFD results by COMSOL to examine the fluid flow in channel 1 (top) and channel 2 (bottom). (a, b) The velocity field in channel 2 (top and isometric views) clearly shows a lateral transform at flow rate of 5  $\mu\text{L}/\text{min}$  by means of transverse movement of fluids. (c) The concentration distributions in a given flow rate of 5  $\mu\text{L}/\text{min}$ .

The amplitude of the ridges ( $\alpha h$ ) in channel 1 compared to the channel height ( $h$ ) was small to enhance mixing. To test the influence of ridge height ratio ( $\alpha = h_1/h$ ) on fluidic behavior, channel 1 with a different height was fabricated. In fact, instead of increasing the height of the ridge, which can cause leakage in the mixers at higher flow rates, the channel height was decreased. Channel 1 with  $\alpha = 0.17$  ( $h_1 = 100 \mu\text{m}$ ,  $h = 600 \mu\text{m}$ ) and channel 3 with  $\alpha = 0.33$  ( $h_1 = 100 \mu\text{m}$ ,  $h = 300 \mu\text{m}$ ) were compared in case of mixing two fluids. For each design, two devices were fabricated. The results obtained are shown in Figure 4-24, where complete mixing has been achieved at a channel length of 36.4 mm (ROI 14) and 39 mm (ROI 15) for  $\alpha = 0.33$  and  $\alpha = 0.17$ , respectively. However, a definite increase in mixing efficiency is observed at the beginning of the channel as  $\alpha$  is increased.

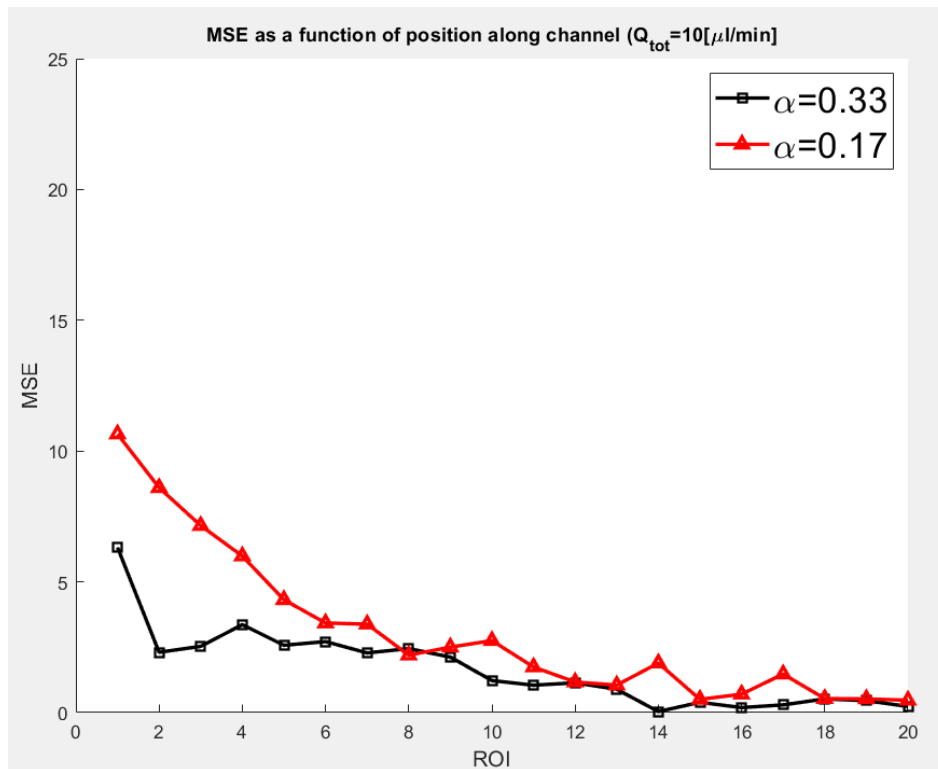


**Figure 4-24.** Influence of the ridge height-to-channel height ratio,  $h_1/h$ , on mixing performance in fabricated mixers by FFF. The total flow rate in the main channel is  $10 \mu\text{L}/\text{min}$ .

The results are consistent with observations in other studies which are used other fabrication methods for creating macro/micro features [30, 32, 130]. The CFD results confirmed such movements as shown in Figure 4-25. A probable explanation is related to the cross movements generated in the mixers with deeper grooves. Figure 4-26 shows the streamlines in channel 3 under the flow rate of  $10 \mu\text{L}/\text{min}$ . For the sake of clarity, the streamlines considered for one inlet. It can be easily seen that the flow direction over the ridges is governed by ridges orientation, where transversal motion near the ridges helps to stretch the fluid from one side to other side of the channel and therefore, increasing the contact area of the fluids (Figure 4-26a). This can be better explained by non-symmetrical molar concentration near the ridges shown in Figure 4-25. In the upper regions far from the ridges, the transversal motion is not observed and mixing happened mainly by diffusion (Figure 4-26b). However, increasing the height ratio ( $\alpha$ ) may be effective for enhancing mixing within a limited range of  $\alpha$ . Yun et al. [32] showed that the optimum values for groove depth ratio can be found in the range of  $0.13 \leq \alpha \leq 0.25$  for SGM mixers. A further increase in  $\alpha$  does not have a significant effect on mixing. It should be noted that a deeper groove can result in a bigger dead volume, which makes mixing

inefficient where solutions can be retained for inordinately long periods in real applications [131].

In this experimental and numerical study, the printed devices with extruded filament width 600  $\mu\text{m}$  and channel height 300  $\mu\text{m}$  ( $\alpha=0.33$ ) showed the best performance of mixing among other studied devices. The presence of typical roughness on the bottom surface of channels makes FFF an exciting tool for applications where mixing two or more fluids in a short time and length of the channel is required. The effect is similar to SGM mixers, with the difference that the patterned ridges in FFF method are an inherent property of the process. In fact, without adding a complexity in fabrication method, FFF printed devices may enhance mixing performance in microfluidics. In comparison to other passive micromixers, no complex geometry or surface patterning were used for fabricated devices, while still avoiding the external energy typical for active mixers.

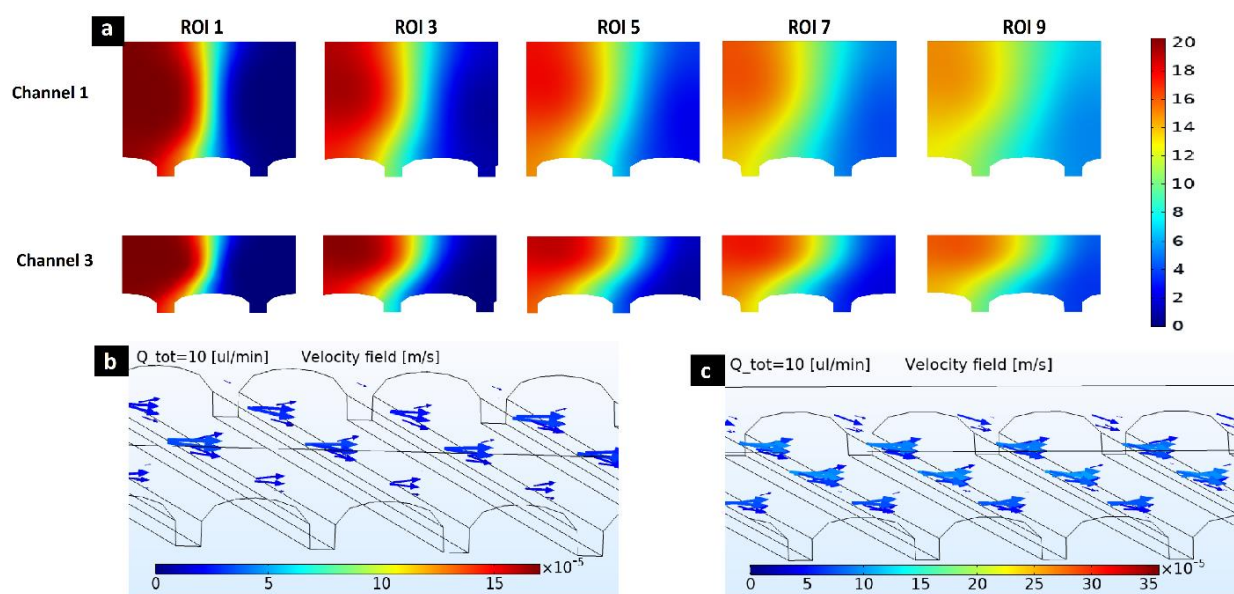


**Figure 4-25.** (a) Evolutions of the concentration distributions at different ridge height ratio by COMSOL. (b) The velocity field for channel 1 at total flow rate of 10  $\mu\text{L}/\text{min}$ . (c) The velocity field for channel 3. It clearly shows a lateral transform at total flow rate of 10  $\mu\text{L}/\text{min}$  in the main channel.

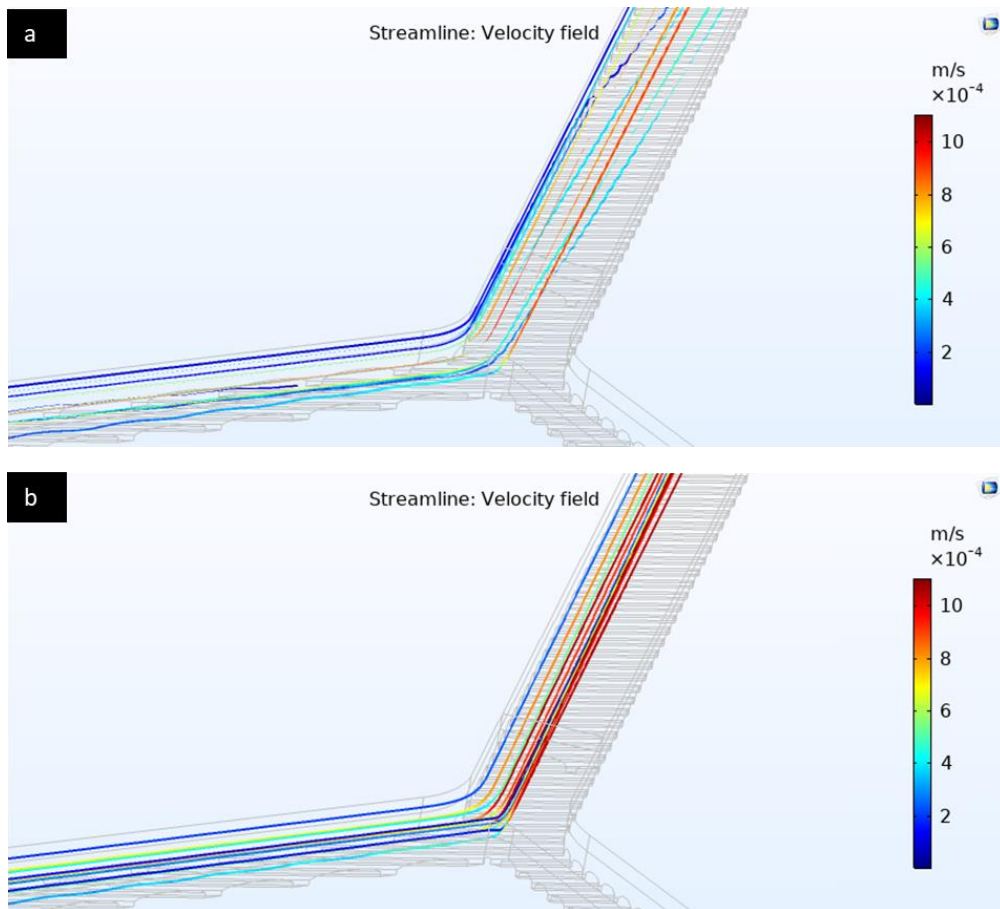
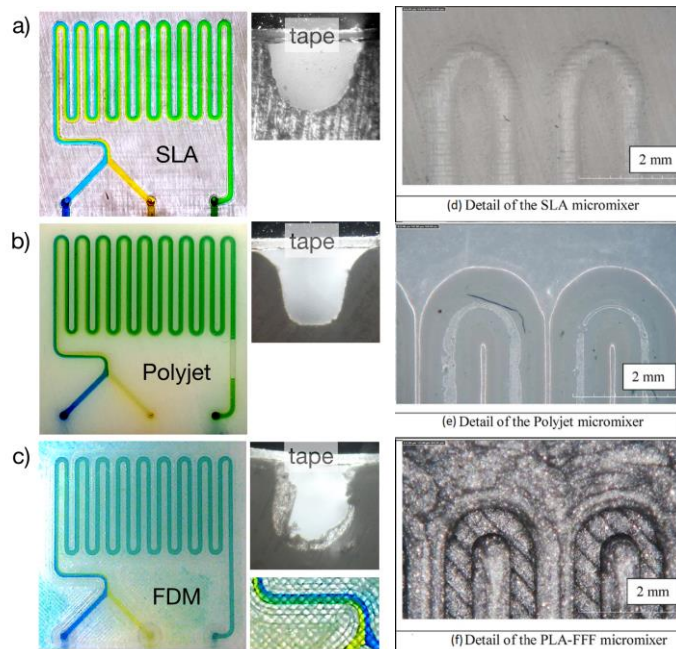


**Figure 4-26.** Flow visualization of the streamlines in channel 3 (flow rate 10  $\mu\text{L}/\text{min}$ ). (a) The streamlines near the ridges. (b). The streamlines in the upper region of the channel far from the ridges.

## 4.5 Comparison of FFF devices with SLA and Polyjet

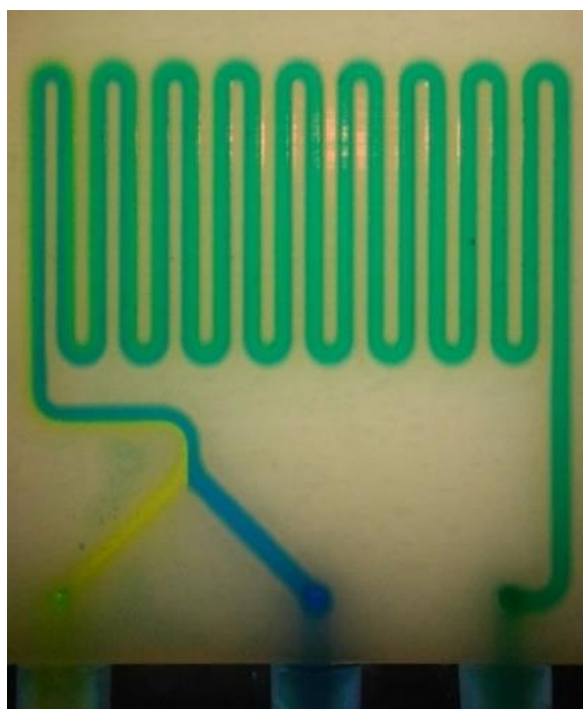
The inherent properties of FFF method were compared with other 3D printing methods in an application like microfluidics micromixers. A classical Y-shaped serpentine channel (Figure 3-5 in chapter 3) fabricated with FFF, SLA, and Polyjet methods. The performance of the fabricated channels was compared in case of mixing two fluids. The methods and printers for manufacturing of micromixers are described in chapter 3 (section 3.2.1). Two different water solutions stained with yellow and blue food color were injected using two syringe pumps (Figure 3-19). Four different flow rates through the main channel were tested: 10  $\mu\text{L}/\text{min}$ , 50  $\mu\text{L}/\text{min}$ , 200  $\mu\text{L}/\text{min}$ , and 400  $\mu\text{L}/\text{min}$ .

Figure 4-27 shows the fabricated micromixers with the three different printing methods. The actual dimensions of three micromixers were measured using two different methods: Photogrammetry and optical profilometry [132]. The limited availability of printable materials and the high cost of the process are the main drawbacks of the Polyjet process. The surface of the SLA micromixer is smoother (Figure 4-27b) compared to FFF, but SLA method requires proprietary resins [133], whereas FFF employs common and well described polymers. The SLA device is more transparent, which facilitates observation and interpretation of the fluidic phenomena. The main advantages of FFF are its relatively low cost and the possibility of using different materials. The FFF micromixer was also imaged with back illumination, whereas the Polyjet was opaque and was imaged under ambient light. The 3D models of micromixers realized through the three fabrication methods present only minor differences between the measured and nominal values of the average channel depth ( $< 20 \mu\text{m}$ ). The cross sections in Figure 4-27 show the fidelity of the 3D printing methods to produce a square cross section. The Polyjet method shows a higher fidelity than the SLA and FFF approaches. In particular, in FFF, due to the spreading of the polymer as it is extruded, the channel can be, in some sections, consistently smaller than CAD model.



**Figure 4-27.** Fabricated micromixers by three different methods of printing. (a,d) micromixer with SLA in cross-section and top view (b,e) micromixer with Polyjet in cross-section and top view (c) micromixer with FFF in cross-section and top view.

All fabricated micromixers showed comparable mixing efficiencies. In this analysis mixing completion and length of the required channel for complete mixing were investigated. For a flow rate of 10  $\mu\text{L}/\text{min}$  in Polyjet mixer, the two flows running through the first section of the chip form a clear boundary, which dissipates after few turns in the serpentine, leading to a homogeneous green color (Figure 4-28). Several flow rates were tested to analyse the influence of the flow rate on length of the required channel and as a result of mixing time (Figure 4-29). When the flow rate is higher (50  $\mu\text{L}/\text{min}$ ) the boundary remains, since the channels length is not enough to allow the diffusion process (Figure 4-29a). For a flow rate of 200  $\mu\text{L}/\text{min}$ , the flow is still laminar and simply stays shorter time in the device to allow diffusional mixing (Figure 4-29b); however, at flow rate of 400  $\mu\text{L}/\text{min}$  the fluid becomes chromatically homogeneous at the end of the channel (Figure 4-29c), which indicates the onset of Dean vortices using serpentine channel at higher Reynolds number [8] (Figure 4-29c).



**Figure 4-28.** Complete mixing obtained with the Polyjet micromixer at a flow rate of 10  $\mu\text{L}/\text{min}$ .

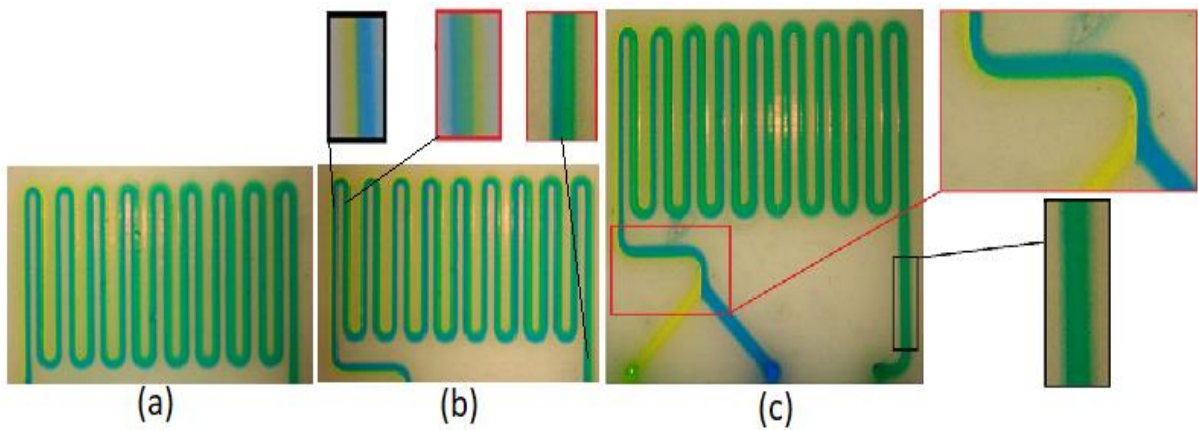


**Figure 4-29.** Mixing obtained in Polyjet micromixer with different flow rates. (a) flow rate of 50  $\mu\text{L}/\text{min}$ ; (b) flow rate of 200  $\mu\text{L}/\text{min}$ ; (c) flow rate of 400  $\mu\text{L}/\text{min}$ .

Performing the same tests on the SLA and FFF micromixers (Figures 4-30 and 4-31) yielded complete mixing for flow rates of 10  $\mu\text{L}/\text{min}$  and 400  $\mu\text{L}/\text{min}$ , similar to the results for the Polyjet mixer. At flow rates of 50  $\mu\text{L}/\text{min}$  and 200  $\mu\text{L}/\text{min}$ , mixing was incomplete and with a clearly visible boundary between the two fluids remaining. However, as the two fluids approach to the outlet, this boundary becomes less distinguishable (Figures 4-30b, c and 4-31b, c).

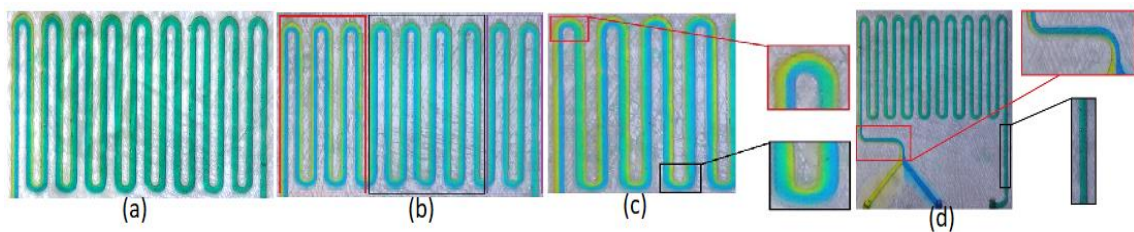


**Figure 4-30.** Mixing obtained in SLA micromixer. (a) flow rate of 10  $\mu\text{L}/\text{min}$ ; (b) flow rate of 50  $\mu\text{L}/\text{min}$ ; (c) flow rate of 200  $\mu\text{L}/\text{min}$ ; (d) flow rate of 400  $\mu\text{L}/\text{min}$ .

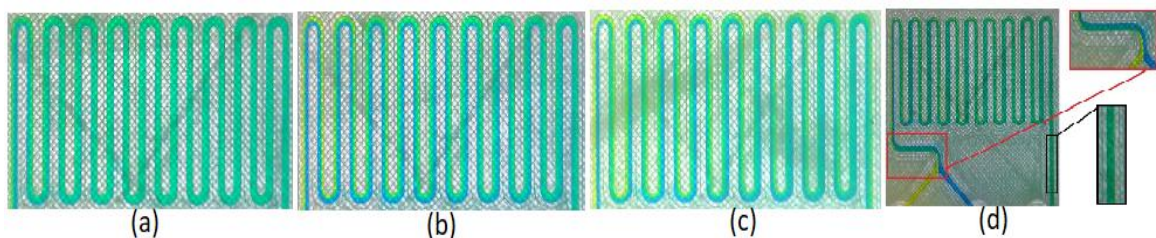


**Figure 4-31.** Mixing obtained in FDM micromixer. (a) flow rate of 10  $\mu\text{L}/\text{min}$ ; (b) flow rate of 50  $\mu\text{L}/\text{min}$ ; (c) flow rate of 200  $\mu\text{L}/\text{min}$ ; (d) flow rate of 400  $\mu\text{L}/\text{min}$ .

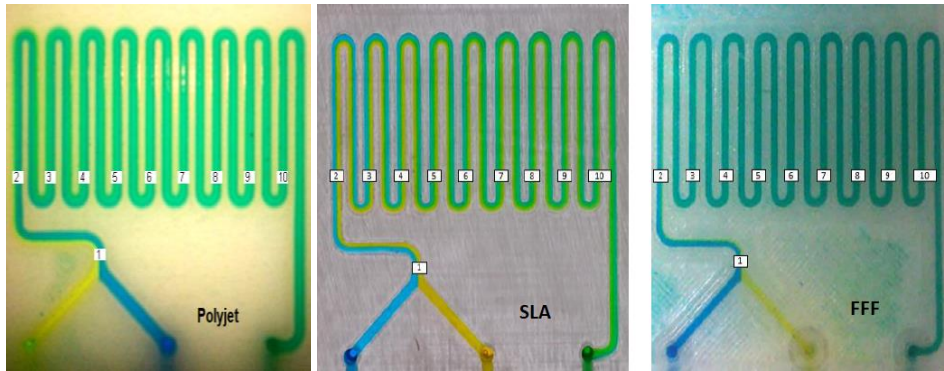


**Figure 4-32.** Regions of interest in the different microchannels.

These results show that by increasing the flow rate, the required channel length to achieve complete mixing needs to be increased as well. To compare the mixing performance, the acquired images in steady regime were analysed. Ten regions of interest (ROIs) were selected along the serpentine (Figure 4-32), and the spatial distribution of the color intensity was recorded using colorimetric analysis algorithm. For each ROI covering the width of the channel ( $w$ , Figure 4-33) the pixels are averaged and the standard deviation calculated for every position along  $w$ . Figure 4-33 describes the blue intensity along the channel, which illustrates the homogenization of the color intensity along the serpentine, when the blue flow diffuses into the yellow flow becoming green.

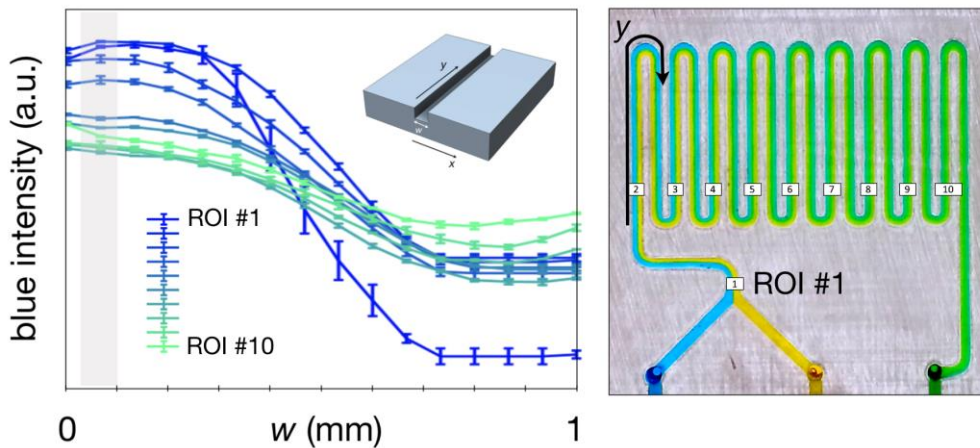


**Figure 4-33.** Diagram of the mixing trend in the microchannel using a blue color scale. X-axis and Y-axis are considered in width and length of channel respectively.

In order to find the channel length that is necessary to achieve complete mixing, the blue intensity decay at the channels' wall is monitored along ROIs (as indicated in Figure 4-33),

leading to a measure of mixing performance. The farther the flow needs to travel to achieve mixing, categorically corresponding to the minimum of the profile, the less effective the platform. Thus, at 10  $\mu\text{l}/\text{min}$ , the analysis shows that FFF is the most effective taking approximately 62% of the distance required for the SLA and Polyjet mixers (Figure 4-34).

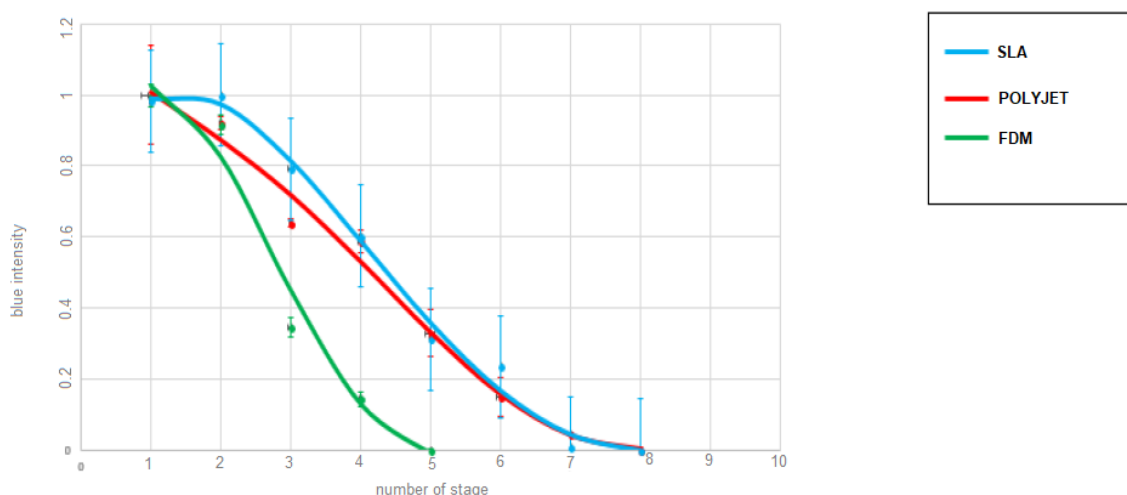


**Figure 4-34.** Required channel length for complete mixing (at a flow rate of 10  $\mu\text{l}/\text{min}$ ) for the different 3D printing methods.

Achieving complete mixing over a short period of time is one of main challenges of micromixers in microfluidic devices. Increasing the flow rates resulted in longer channel lengths to achieve complete mixing. For very high flow rates of 400  $\mu\text{l}/\text{min}$  ( $Re = 14.81$ ) complete mixing occurred in all three mixers, putting in evidence that a higher mixing efficiency is reached even though the flow is laminar in theory. The Y-shape serpentine microchannel used in this study has smaller dimensions compared to simple Y-shaped microchannels [101] and provides the possibility of testing these high flow rates and channel lengths, which is a main advantage of 3D printed fluidics compared with classical soft lithography devices relying of planar photolithographic templates.

Table 4-11 presents a comparison of the three types of micromixers. Although, the channel dimensions and flow rates are different from those used with simple Y-shape mixers in [101], the results are almost identical for these two very different design approaches. The fact the FFF requires a shortest channel length is due to roughness of the FFF channel as studied before. It is a clear example where the apparent limitation of the 3D printing technology is actual beneficial for the configuration of microfluidic devices. The presence of macroscopic

roughness, due to the physic of the process itself, on the FFF channel surface can act as ridges and cause stretching and folding of the flow as described in [134]. Ridges can cause chaotic advection which leads to increased mixing, thus reducing the required channel length to achieve complete mixing [27]. However, it must be highlighted that for higher flow rates the effect of ridges in FFF is negligible and the best performance is obtained by SLA mixer.

**Table 4-11.** Required length for each Y-shape serpentine micromixer fabricated by three methods where a relative intensity was reached, which can be considered complete mixing.

methods	Flow rate=10 [μl/min] Re=0.37	Flow rate=50 [μl/min] Re=1.85	Flow rate=200 [μl/min] Re=7.4	Flow rate=400 [μl/min] Re=14.81
	Length <sup>1</sup> [mm or stage]	Length [mm or stage]	Length [mm or stage]	Length [mm or stage]
Polyjet	150.6 (ROI 8)	-	-	197.6 (ROI 10)
SLA	150.6 (ROI 8)	-	-	150.6 (ROI 8)
FDM	80.6 (ROI 5)	-	-	197.6 (ROI 10)

<sup>1</sup> Obtained values in mm calculated for different ROIs

## 4.6 Chip Fabrication for Lysis and DNA Extraction

The fabricated chips are shown in figure 4-35. The three main steps for extraction DNA from a sample are carry out in two chips. We explained in chapter 3, in order to evaluate the performance of each part, the initial design is divided into two different chips. The first chip is designed for the lysis and binding processes. The second chip is designed to extract DNA from other molecules and impurities. The chips are fabricated using the Ultimaker 3 and with natural PLA. The top surfaces of the chip leave open and closed with double sided tape after fabrication. For injection the reagents as well as connecting the chips, silicon tubes are used as shown in Figure 4-35.

### 4.6.1 Experimental setup

The experimental setup for the tests shown in Figure 4-36. Prior to test, the devices were cleaned with water and dried using warm air. Compressed air jets were used to eliminate any drops of water trapped inside the channel. The reagents for a plant kit (NucleoMag 96 plant) were used for the experiments as shown in Figure 4-37. DI water stained with red color used

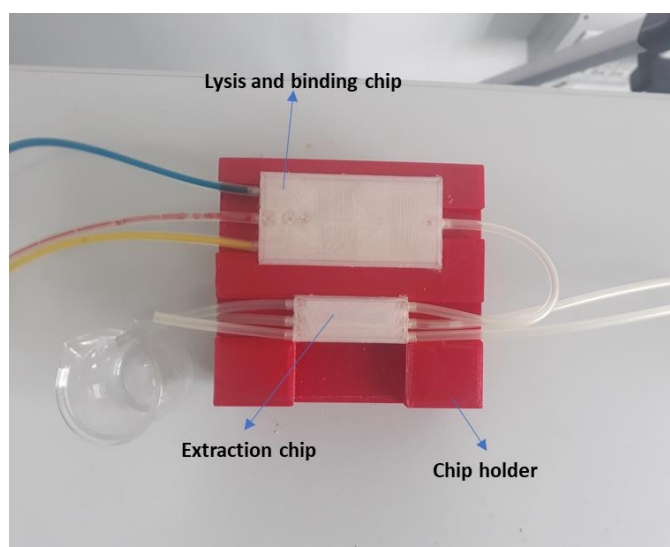


**Figure 4-35.** Fabricated chips with FFF method. The devices are connected together with silicon tubes. chip holder (TPU, flexible material) is used to fix the chips during the tests.

as sample solution. Different solutions were injected to the first chip (Lysis-Binding) using two syringe pumps equipped with 5 mL disposable syringes at equal flow rates (10  $\mu\text{L}/\text{min}$ ). The colored DI water with lysis solution injected using one syringe pump. The two flows meet at junction and running through the first section of the Lysis chip form a clear boundary, which dissipates after few turns in the serpentine mixing channel, leading to a homogeneous light red

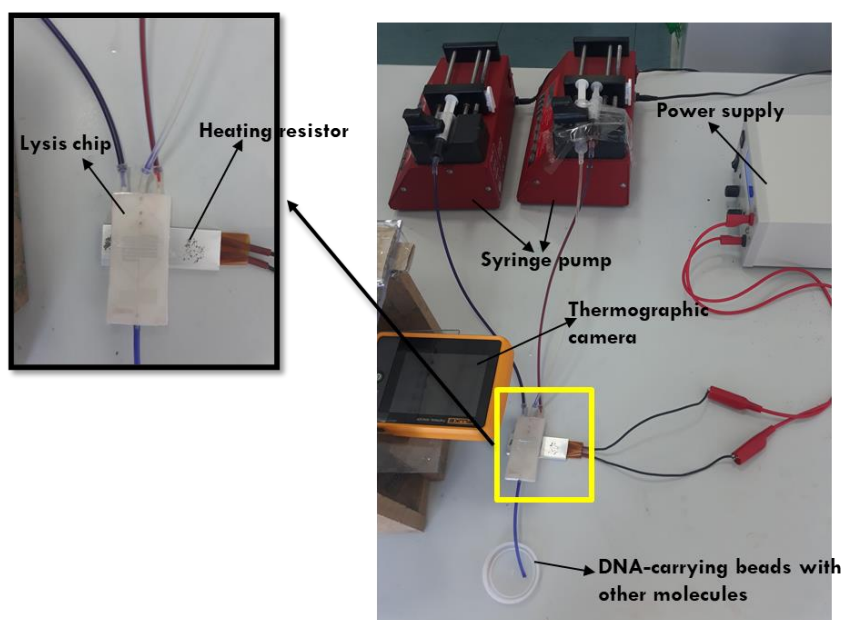


**Figure 4-36.** Experimental setup and detection system for testing chips.



**Figure 4-37.** Different solutions used for the test. DI water stained with red color used as sample solution. color (Figure 4-38). Then, the homogeneous stream entered to the incubation channel, which is wider and allows stream to remain for longer time for incubating and thermal shocks (Figure 4-38). During the test, a heater attached to the bottom of the chip helps to increase the efficiency of lysis process. The temperature of the solutions inside the channel recorded by thermal camera (Figure 4-39). When the heating resistor positioned along the chip, the binding process carry out with a temperature around 50 °C, which helps the process.

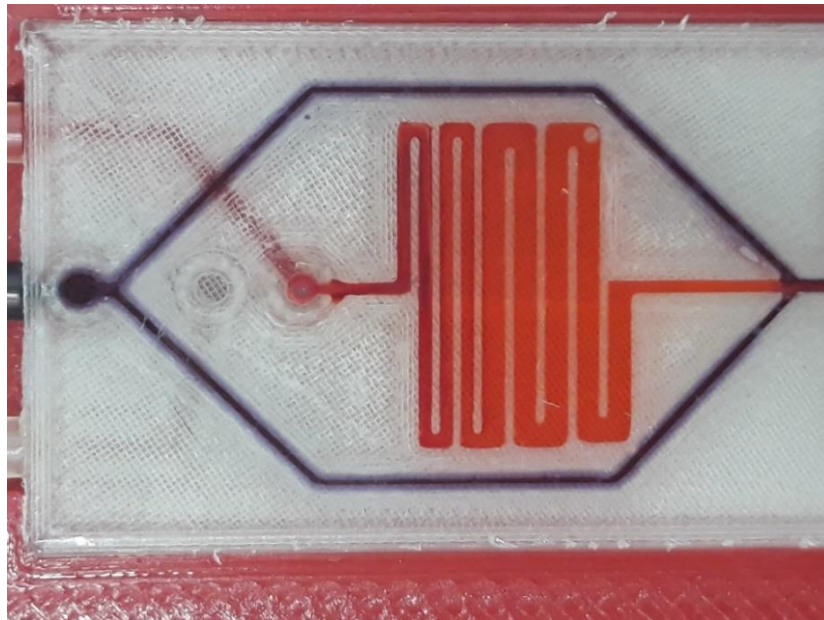


**Figure 4-38.** Schematic of the lysis process inside the Lysis-Binding chip

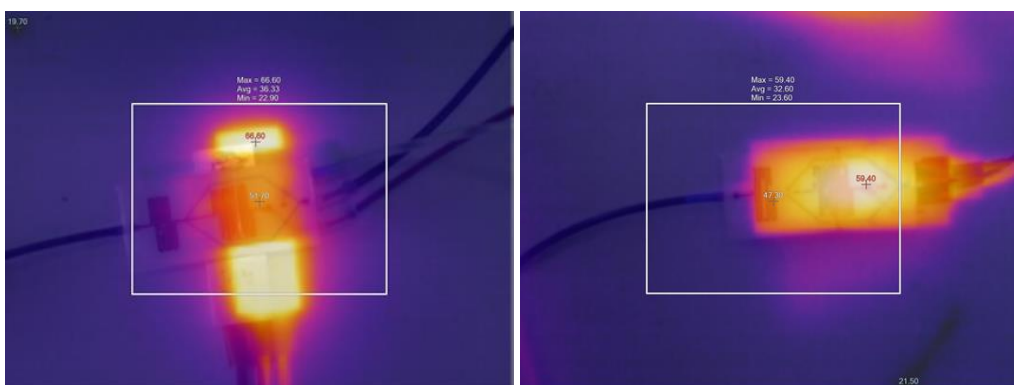


**Figure 4-39.** Control of temperature using a thermal camera. Left: captured image with positioning the heater perpendicular to chip, Right: captured image with positioning the heater along the chip.

After completing lysis process, binding buffer (magnetic beads dissolved in binding buffer, stained with black color) injected to the chip using another syringe pump. The magnet beads solution meets with lysed solution at the junction, and after mixing and incubating inside the binding channel, the resulting solution has a brown color (Figure 4-40).

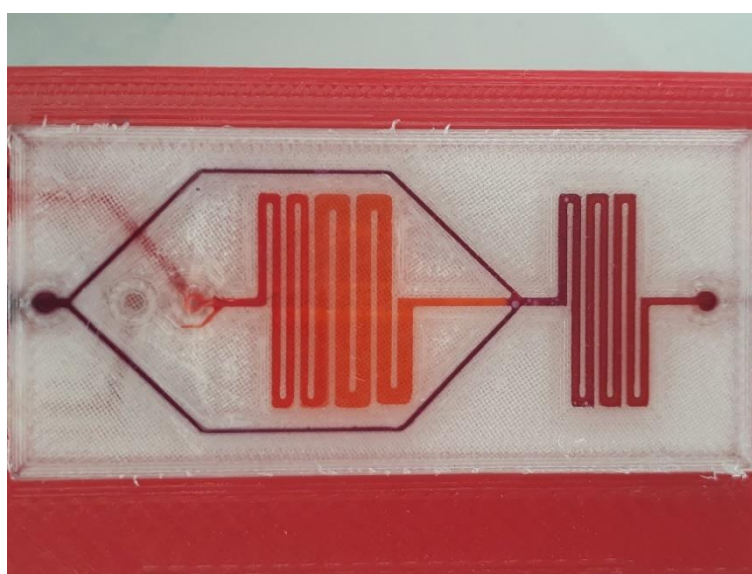


**Figure 4-40.** Binding process. Binding buffer mixed with lysed solution, the resulting solution is with brown color.

In the extraction chip, three solutions were injected in equal flow rates (50  $\mu\text{L}/\text{min}$ ). The magnet beads dissolved in the brown solution pass across the interfaces of washing and elute buffers via magnetic force provided by an external permanent magnet and attach to the bottom wall of extraction chip. Figure 4-41 shows the absorbed beads by the permanent magnet.

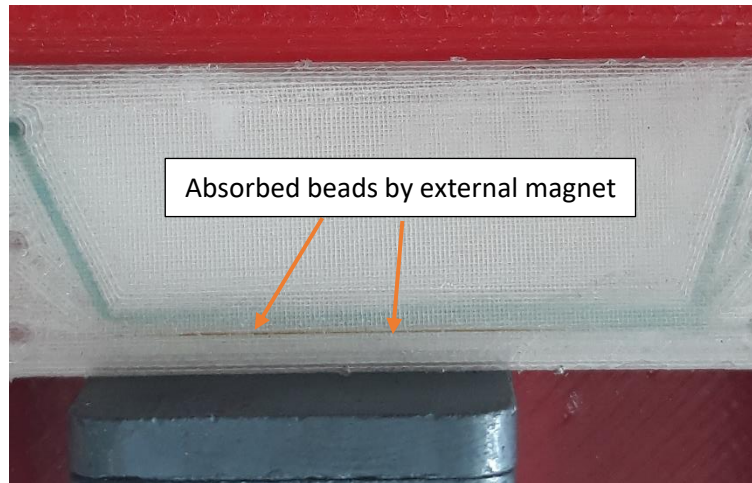


**Figure 4-41.** Extraction chip showing the beads absorbed by an external permanent magnet.

The following results observed during the tests:

1. The designed channels for lysis chip were sufficient for complete mixing.
2. The double-sided tape detached from top surface of chip at temperature around 60 °C.
3. Natural PLA has a glass transition temperature around 60-65 °C, and after a while, a deformation caused to the chip (Figure 4-42).
4. The used silicon tubes connected to inlets became flexible due to the high temperature and detached from the device.

To address the above problems, first the new materials (biocompatible and transparent) are tested. The new material should be selected based on its heat resistance at temperatures around 60 °C. Different materials have tested and finally, high temperature PLA was selected for fabrication of the chip. However, it needed one step annealing to achieve optimal thermal stability. Annealing is done by exposing the printed HT PLA device to a sufficiently high temperature that allows the individual atoms in the plastic to migrate to the nucleating agent and continue the recrystallization process. For this, in a pot that was large enough to submerge the printed chip, we heated water up to around 90 to 95 °C and then placed the printed chip in the pot, cover it with a lid, and left it for up to 10 minutes. The final part can resist at temperatures up to 115 °C. Figure 4-42 shows the natural PLA and HT PLA when exposed to temperature of 60°C.

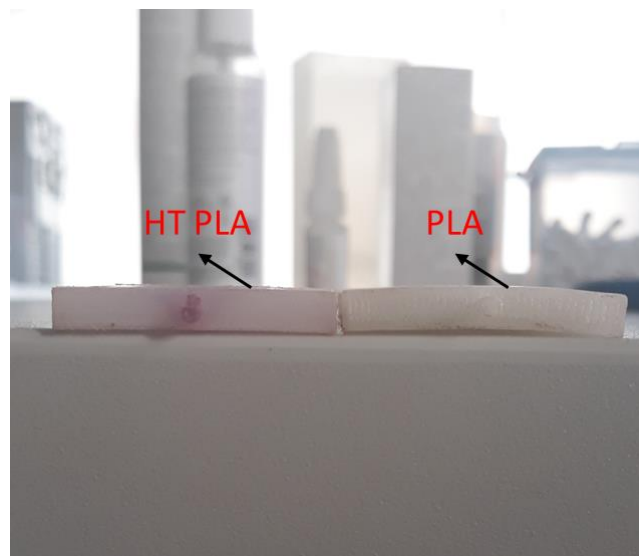


**Figure 4-42.** Natural PLA and HT PLA performance at temperature 60 °C. A deformation was observed for the printed chip with natural PLA.

The problem for the detaching the tape are solved with printing the HT PLA directly on transparent PMMA sheet. PMMA is a low-cost polymer with high transparency to visible light. The glass transition values of commercial grades of PMMA range from 85 to 165 °C; the range is so wide because of the vast number of commercial compositions which are copolymers with co-monomers other than methyl methacrylate. The chemical structure of PMMA polymer is similar to PLA (Figure 4-43), where both present an ester group, leading to a high binding level when these materials are putting in contact. This cause to a good adhesion where no leakage or breakage could occur between the printed part (HT PLA) and the transparent slide (PMMA). PMMA sheets were obtained with a nominal thickness of 1 mm from the local shop.

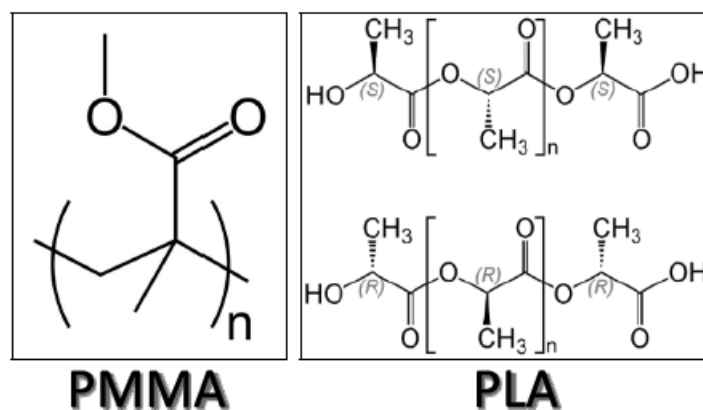


**Figure 4-43.** Chemical Structure of PMMA and PLA polymers.

The printing parameters must be carefully selected to get the first layer of the object in contact with PMMA, leading to leakages or disconnection if the distance is too high or the blockage of the channels if it is too low. The distance between the nozzle and the PMMA sheet very important and effect on the adhesion between two materials and the resolution of the printed channels. It may have a good adhesion by choosing small distance between the nozzle and PMMA substrate, however, the channels will have lower dimensions than the CAD model. Therefore, finding the optimal distance and process parameters is the key to the success of the process.

The procedure for finding the optimal distance and print the devices on top of a PMMA slide is simplified if the 3D-printer has an automated z-axis zero positioning. However, for our printer (Ultimaker 3, not equipped with an automated zero positioning), this can be done in two ways: one way is measuring the actual thickness of the PMMA slide with micrometer. Then, set the printing height to start at this value with setting the optimal height value for the first layer. The second way (which is our case) is fixing the PMMA substrate on the build plate and doing the calibration with considering the PMMA sheet (Figure 4-44). Figure 4-45 showing a schematic of the process of binding PMMA and HT PLA polymers.

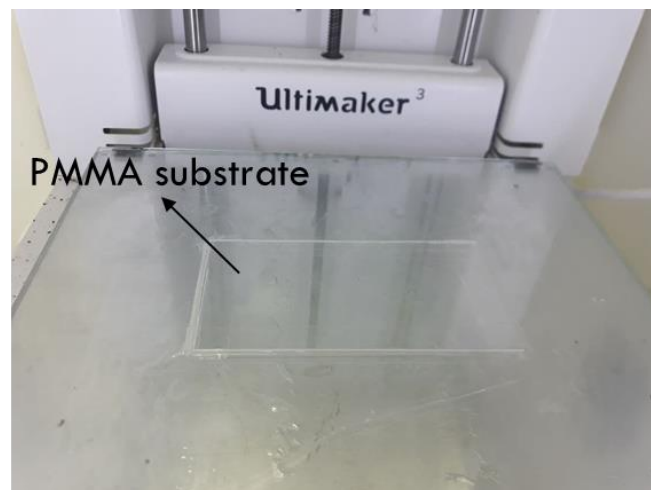


**Figure 4-44.** Fixing PMMA substrate on the build plate with adhesive tape and start printing over it by doing the calibration with PMMA sheet.

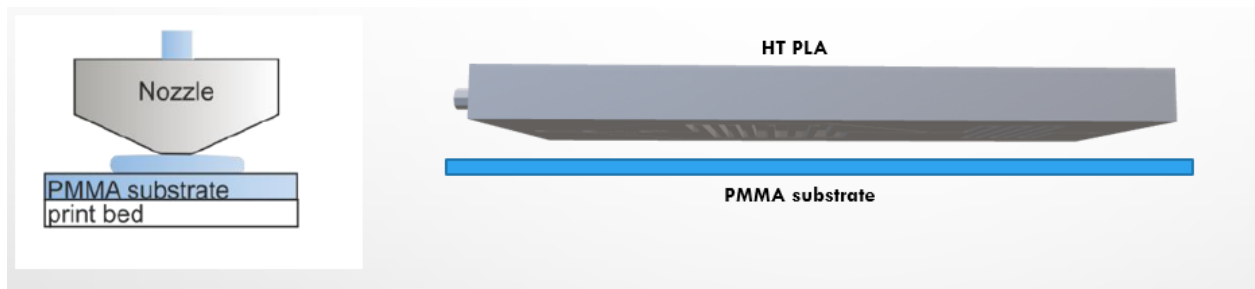


**Figure 4-45.** Representation of the 3D-printing process on top of a PMMA substrate.

Table 4-12 shows the process parameters for the printing HT PLA on the top of PMMA sheet. Generally, in FFF process, the actual dimensions of the channels are different from CAD model and normally they are lower than the designed CAD model [101]. In this study, because of having a good adhesion between two materials, the gap between the nozzle and PMMA sheet may be set to lower values, which leads to lower height of the channels than CAD model (in Z direction). To overcome this problem, three sets of channels with different shapes of the roof (Figure 4-46) are designed and printed with different printing parameters. As shown in Figure 4-46, printing a simple square cross-section results in an excessive sagging of the top layer which will clog the channel if small channel sizes are printed. An improvement was found by adding a triangular shaped roof or curved roof for the channels. Considering all channels, the results of the triangular shaped roof is better than other two models. Figure 4-47 shows the printed chip with bonded PMMA sheet on its top surface.

**Table 4-12.** Optimized parameters settings to print 3D microfluidic devices.

Printing Parameter	Nozzle 0.4 mm
Printing temperature (°C)	245
Print speed (mm/s)	18
Infill printing speed (mm/s)	18
Wall printing speed (mm/s)	8
Layer height (μm)	100
Initial layer height (μm)	200
Filament orientation (°)	60
Flow (%)	100
Infill density	100 %
Build temperature	90

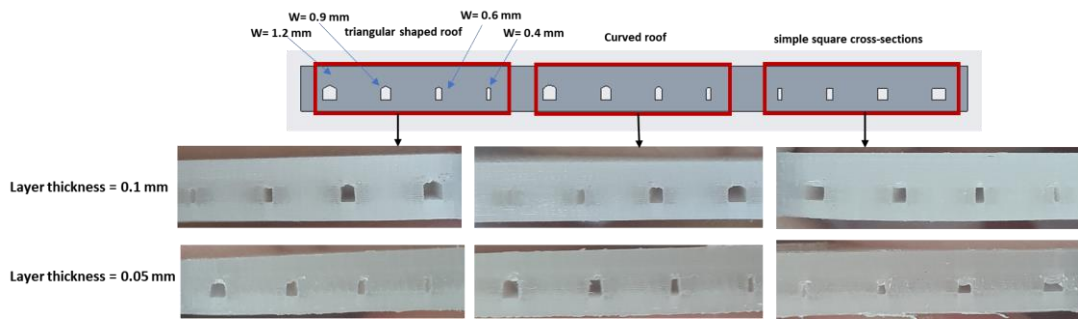


**Figure 4-46.** Printed channels with different shapes of the roof. Top: showing CAD model with cross-sections of different channels size and different roof of the channels; Bottom: Printed same channels with two different layer thicknesses, the channels with triangular shaped roof showed better results (fidelity of cross-sectional) with a layer height of 0.1 mm.

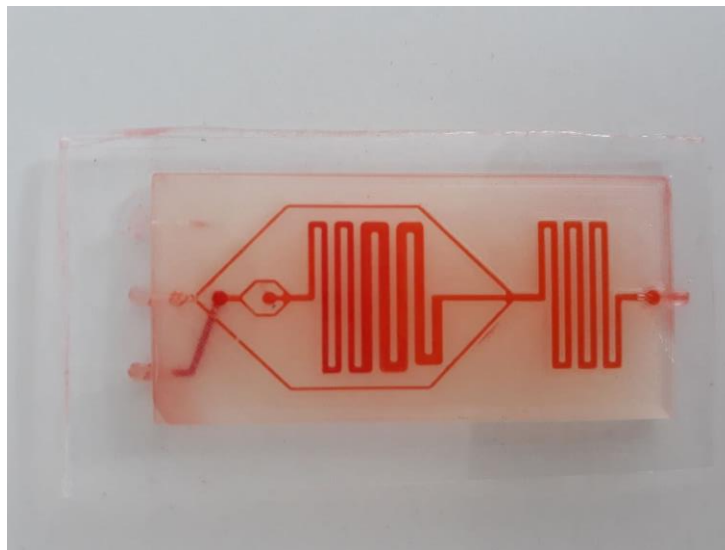


**Figure 4-47.** printed chip with HT PLA and PMMA substrate, a colored dye injected to show the transparency of devices.

To address the problem for the connectors at high temperature, the standard fitting connectors were used for connecting the tubes to the inlets. For this, first the CAD model of the chip modified as shown in Figure 4-48. The holes for creating the threads printed close to inner diameter of connectors using FFF printer. A hand threading tap then used to create the threads based on used fitting connectors (Figure 4-48). Figure 4-48 shows the printed device with silicon tubes connected to the device through the fitting connectors.

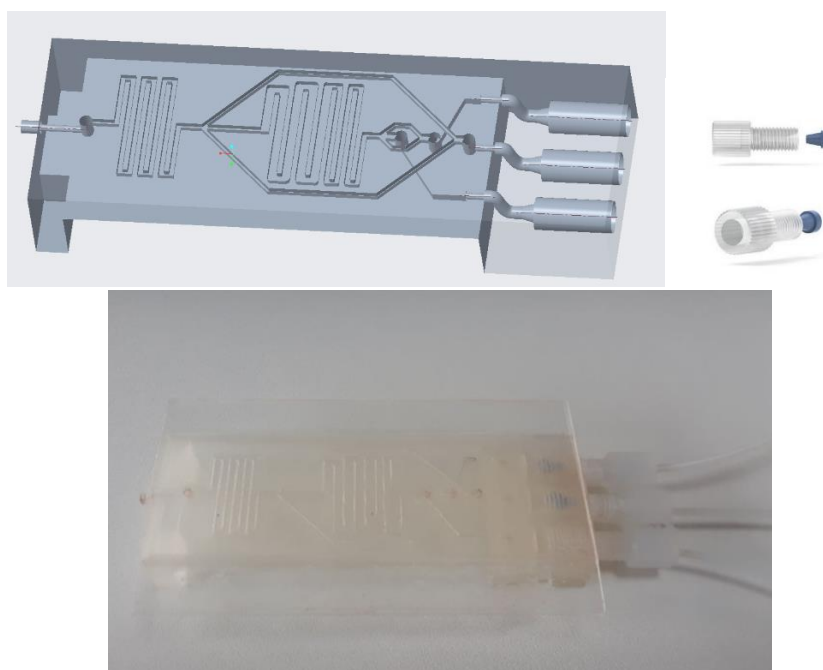


**Figure 4-48.** Modified CAD design standard fitting connectors (top); Printed chip with standard fitting connectors (bottom).

In this study, the extraction chip also printed using a DLP printer. The printed surface created by FFF method can help for mixing however, it has some disadvantages for applications where a separation is required. The fine surface produced by stereolithography method helps for the separation of DNA from other molecules. Figure 4-49 shows the extraction chip printed using DLP printer.

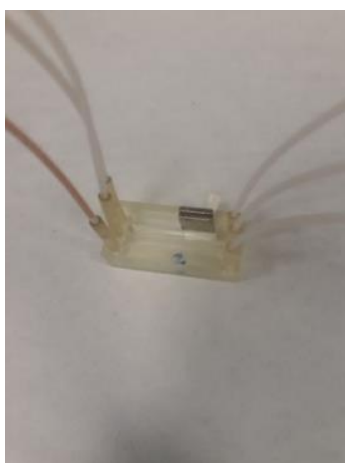


**Figure 4-49.** Extraction chip printed using a DLP printer.

## References

- [1] J. X. J. Zhang and K. Hoshino, "Chapter 3 - Microfluidics and micro total analytical systems," in *Molecular Sensors and Nanodevices (Second Edition)*, J. X. J. Zhang and K. Hoshino, Eds.: Academic Press, 2019, pp. 113-179.
- [2] G. Cai, L. Xue, H. Zhang, and J. Lin, "A Review on Micromixers," *Micromachines*, vol. 8, no. 9, p. 274, 2017.
- [3] M. Rezaei *et al.*, "Point of Care Diagnostics in the Age of COVID-19," *Diagnostics*, vol. 11, no. 1, p. 9, 2021.
- [4] V. Prasad and S. Mailankody, "Research and Development Spending to Bring a Single Cancer Drug to Market and Revenues After Approval," (in eng), *JAMA internal medicine*, vol. 177, no. 11, pp. 1569-1575, 2017.
- [5] J. Sun, A. R. Warden, and X. Ding, "Recent advances in microfluidics for drug screening," *Biomicrofluidics*, vol. 13, no. 6, p. 061503, 2019.
- [6] L. Yin *et al.*, "Efficient Drug Screening and Nephrotoxicity Assessment on Co-culture Microfluidic Kidney Chip," *Scientific Reports*, vol. 10, no. 1, p. 6568, 2020/04/16 2020.
- [7] A. Bohr, S. Colombo, and H. Jensen, "Chapter 15 - Future of microfluidics in research and in the market," in *Microfluidics for Pharmaceutical Applications*, H. A. Santos, D. Liu, and H. Zhang, Eds.: William Andrew Publishing, 2019, pp. 425-465.
- [8] S. Kim and S. J. Lee, "Measurement of Dean flow in a curved micro-tube using micro digital holographic particle tracking velocimetry," *Experiments in Fluids*, vol. 46, no. 2, pp. 255-264, 2009.
- [9] G. S. Jeong, S. Chung, C.-B. Kim, and S.-H. Lee, "Applications of micromixing technology," *Analyst*, vol. 135, no. 3, pp. 460-473, 2010.
- [10] C.-Y. Lee, C.-L. Chang, Y.-N. Wang, and L.-M. Fu, "Microfluidic mixing: a review," *International journal of molecular sciences*, vol. 12, no. 5, pp. 3263-3287, 2011.
- [11] W. R. Dean, "XVI. Note on the motion of fluid in a curved pipe," *The London, Edinburgh, and Dublin Philosophical Magazine and Journal of Science*, vol. 4, no. 20, pp. 208-223, 1927.
- [12] G. Whitesides, "The lab finally comes to the chip!," *Lab on a Chip*, 10.1039/C4LC90072C vol. 14, no. 17, pp. 3125-3126, 2014.
- [13] W. Kevin and Z. H. Fan, "Mixing in microfluidic devices and enhancement methods," *Journal of Micromechanics and Microengineering*, vol. 25, no. 9, p. 094001, 2015.
- [14] L.-H. Lu, K. S. Ryu, and C. Liu, "A Novel Microstirrer and Arrays for Microfluidic Mixing," in *Micro Total Analysis Systems 2001*, Dordrecht, 2001, pp. 28-30: Springer Netherlands.
- [15] N. Nam-Trung and W. Zhigang, "Micromixers—a review," *Journal of Micromechanics and Microengineering*, vol. 15, no. 2, p. R1, 2005.
- [16] V. Hessel, H. Löwe, and F. Schönfeld, "Micromixers—a review on passive and active mixing principles," *Chemical Engineering Science*, vol. 60, no. 8, pp. 2479-2501, 2005/04/01/ 2005.
- [17] L. Capretto, W. Cheng, M. Hill, and X. Zhang, "Micromixing Within Microfluidic Devices," in *Microfluidics: Technologies and Applications*, B. Lin, Ed. Berlin, Heidelberg: Springer Berlin Heidelberg, 2011, pp. 27-68.
- [18] G. A. Mensing, T. M. Pearce, M. D. Graham, and D. J. Beebe, "An externally driven magnetic microstirrer," *Philosophical Transactions of the Royal Society of London. Series A: Mathematical, Physical and Engineering Sciences*, vol. 362, no. 1818, pp. 1059-1068, 2004.

- [19] C.-Y. Lee, W.-T. Wang, C.-C. Liu, and L.-M. Fu, "Passive mixers in microfluidic systems: A review," *Chemical Engineering Journal*, vol. 288, pp. 146-160, 2016/03/15/ 2016.
- [20] A. E. Kamholz, B. H. Weigl, B. A. Finlayson, and P. Yager, "Quantitative Analysis of Molecular Interaction in a Microfluidic Channel: The T-Sensor," *Analytical Chemistry*, vol. 71, no. 23, pp. 5340-5347, 1999/12/01 1999.
- [21] V. Mengeaud, J. Josserand, and H. H. Girault, "Mixing Processes in a Zigzag Microchannel: Finite Element Simulations and Optical Study," *Analytical Chemistry*, vol. 74, no. 16, pp. 4279-4286, 2002/08/01 2002.
- [22] R. H. Liu *et al.*, "Passive mixing in a three-dimensional serpentine microchannel," *Journal of Microelectromechanical Systems*, vol. 9, no. 2, pp. 190-197, 2000.
- [23] D. S. Kim, S. H. Lee, T. H. Kwon, and C. H. Ahn, "A serpentine laminating micromixer combining splitting/recombination and advection," *Lab on a Chip*, vol. 5, no. 7, pp. 739-747, 2005.
- [24] C. Y. Lim, Y. C. Lam, and C. Yang, "Mixing enhancement in microfluidic channel with a constriction under periodic electro-osmotic flow," *Biomicrofluidics*, vol. 4, no. 1, p. 014101, 2010.
- [25] Y. Su, G. Chen, and E. Y. Kenig, "An experimental study on the numbering-up of microchannels for liquid mixing," *Lab on a Chip*, vol. 15, no. 1, pp. 179-187, 2015.
- [26] T. W. Lim *et al.*, "Three-dimensionally crossing manifold micro-mixer for fast mixing in a short channel length," *Lab on a Chip*, vol. 11, no. 1, pp. 100-103, 2011.
- [27] A. D. Stroock, S. K. Dertinger, A. Ajdari, I. Mezić, H. A. Stone, and G. M. Whitesides, "Chaotic mixer for microchannels," *Science*, vol. 295, no. 5555, pp. 647-651, 2002.
- [28] T. J. Johnson, D. Ross, and L. E. Locascio, "Rapid microfluidic mixing," *Analytical chemistry*, vol. 74, no. 1, pp. 45-51, 2002.
- [29] Z. Xia, L. Cattafesta, and Z. H. Fan, "Deconvolution microscopy for flow visualization in microchannels," *Analytical chemistry*, vol. 79, no. 6, pp. 2576-2582, 2007.
- [30] Y. Du, Z. Zhang, C. Yim, M. Lin, and X. Cao, "Evaluation of floor-grooved micromixers using concentration-channel length profiles," *Micromachines*, vol. 1, no. 1, pp. 19-33, 2010.
- [31] T. Rhoades, C. R. Kothapalli, and P. S. Fodor, "Mixing Optimization in Grooved Serpentine Microchannels," *Micromachines*, vol. 11, no. 1, p. 61, 2020.
- [32] S. Yun, G. Lim, K. H. Kang, and Y. K. Suh, "Geometric effects on lateral transport induced by slanted grooves in a microchannel at a low Reynolds number," *Chemical Engineering Science*, vol. 104, pp. 82-92, 2013/12/18/ 2013.
- [33] T. J. Kwak, Y. G. Nam, M. A. Najera, S. W. Lee, J. R. Strickler, and W.-J. Chang, "Convex grooves in staggered herringbone mixer improve mixing efficiency of laminar flow in microchannel," *PloS one*, vol. 11, no. 11, 2016.
- [34] J. Marschewski *et al.*, "Mixing with herringbone-inspired microstructures: overcoming the diffusion limit in co-laminar microfluidic devices," *Lab on a Chip*, vol. 15, no. 8, pp. 1923-1933, 2015.
- [35] J. Ou, G. R. Moss, and J. P. Rothstein, "Enhanced mixing in laminar flows using ultrahydrophobic surfaces," *Physical Review E*, vol. 76, no. 1, p. 016304, 2007.
- [36] J. Ou, B. Perot, and J. P. Rothstein, "Laminar drag reduction in microchannels using ultrahydrophobic surfaces," *Physics of fluids*, vol. 16, no. 12, pp. 4635-4643, 2004.
- [37] S. J. Kim, Y.-A. Song, P. L. Skipper, and J. Han, "Electrohydrodynamic generation and delivery of monodisperse picoliter droplets using a poly (dimethylsiloxane) microchip," *Analytical chemistry*, vol. 78, no. 23, pp. 8011-8019, 2006.

- [38] R. M. Lorenz, J. S. Edgar, G. D. Jeffries, and D. T. Chiu, "Microfluidic and optical systems for the on-demand generation and manipulation of single femtoliter-volume aqueous droplets," *Analytical chemistry*, vol. 78, no. 18, pp. 6433-6439, 2006.
- [39] E. Quevedo, J. Steinbacher, and D. T. McQuade, "Interfacial polymerization within a simplified microfluidic device: capturing capsules," *Journal of the American Chemical Society*, vol. 127, no. 30, pp. 10498-10499, 2005.
- [40] A. Günther, M. Jhunjhunwala, M. Thalmann, M. A. Schmidt, and K. F. Jensen, "Micromixing of miscible liquids in segmented gas-liquid flow," *Langmuir*, vol. 21, no. 4, pp. 1547-1555, 2005.
- [41] J. D. Tice, H. Song, A. D. Lyon, and R. F. Ismagilov, "Formation of droplets and mixing in multiphase microfluidics at low values of the Reynolds and the capillary numbers," *Langmuir*, vol. 19, no. 22, pp. 9127-9133, 2003.
- [42] L.-H. Lu, K. S. Ryu, and C. Liu, "A magnetic microstirrer and array for microfluidic mixing," *Journal of microelectromechanical systems*, vol. 11, no. 5, pp. 462-469, 2002.
- [43] D. Ahmed, X. Mao, J. Shi, B. K. Juluri, and T. J. Huang, "A millisecond micromixer via single-bubble-based acoustic streaming," *Lab on a Chip*, vol. 9, no. 18, pp. 2738-2741, 2009.
- [44] Z. Yang, S. Matsumoto, H. Goto, M. Matsumoto, and R. Maeda, "Ultrasonic micromixer for microfluidic systems," *Sensors and Actuators A: Physical*, vol. 93, no. 3, pp. 266-272, 2001.
- [45] L.-S. Jang, S.-H. Chao, M. R. Holl, and D. R. Meldrum, "Resonant mode-hopping micromixing," *Sensors and Actuators A: Physical*, vol. 138, no. 1, pp. 179-186, 2007.
- [46] R. H. Liu, R. Lenigk, R. L. Druyor-Sanchez, J. Yang, and P. Grodzinski, "Hybridization enhancement using cavitation microstreaming," *Analytical Chemistry*, vol. 75, no. 8, pp. 1911-1917, 2003.
- [47] G. G. Yaralioglu, I. O. Wygant, T. C. Marentis, and B. T. Khuri-Yakub, "Ultrasonic mixing in microfluidic channels using integrated transducers," *Analytical chemistry*, vol. 76, no. 13, pp. 3694-3698, 2004.
- [48] T. Frommelt, M. Kostur, M. Wenzel-Schäfer, P. Talkner, P. Hänggi, and A. Wixforth, "Microfluidic mixing via acoustically driven chaotic advection," *Physical review letters*, vol. 100, no. 3, p. 034502, 2008.
- [49] I. Glasgow and N. Aubry, "Enhancement of microfluidic mixing using time pulsing," *Lab on a Chip*, vol. 3, no. 2, pp. 114-120, 2003.
- [50] I. Glasgow, S. Lieber, and N. Aubry, "Parameters influencing pulsed flow mixing in microchannels," *Analytical chemistry*, vol. 76, no. 16, pp. 4825-4832, 2004.
- [51] X. Niu and Y.-K. Lee, "Efficient spatial-temporal chaotic mixing in microchannels," *Journal of Micromechanics and microengineering*, vol. 13, no. 3, p. 454, 2003.
- [52] J.-H. Tsai and L. Lin, "Active microfluidic mixer and gas bubble filter driven by thermal bubble micropump," *Sensors and Actuators A: Physical*, vol. 97, pp. 665-671, 2002.
- [53] A. O. El Moctar, N. Aubry, and J. Batton, "Electro-hydrodynamic micro-fluidic mixer," *Lab on a Chip*, vol. 3, no. 4, pp. 273-280, 2003.
- [54] D. Nouri, A. Zabihi-Hesari, and M. Passandideh-Fard, "Rapid mixing in micromixers using magnetic field," *Sensors and Actuators A: Physical*, vol. 255, pp. 79-86, 2017/03/01/ 2017.
- [55] M. Abolhasani, A. Oskoei, A. Klinkova, E. Kumacheva, and A. Günther, "Shaken, and stirred: oscillatory segmented flow for controlled size-evolution of colloidal nanomaterials," *Lab on a Chip*, vol. 14, no. 13, pp. 2309-2318, 2014.
- [56] P. N. Nge, C. I. Rogers, and A. T. Woolley, "Advances in microfluidic materials, functions, integration, and applications," *Chemical reviews*, vol. 113, no. 4, pp. 2550-2583, 2013.

- [57] Y. Li, C. Liu, X. Feng, Y. Xu, and B.-F. Liu, "Ultrafast Microfluidic Mixer for Tracking the Early Folding Kinetics of Human Telomere G-Quadruplex," *Analytical Chemistry*, vol. 86, no. 9, pp. 4333-4339, 2014/05/06 2014.
- [58] J. B. You *et al.*, "PDMS-based turbulent microfluidic mixer," *Lab on a Chip*, 10.1039/C5LC00070J vol. 15, no. 7, pp. 1727-1735, 2015.
- [59] H. Song, M. R. Bringer, J. D. Tice, C. J. Gerdts, and R. F. Ismagilov, "Experimental test of scaling of mixing by chaotic advection in droplets moving through microfluidic channels," *Applied Physics Letters*, vol. 83, no. 22, pp. 4664-4666, 2003.
- [60] Z. Che, N.-T. Nguyen, and T. N. Wong, "Analysis of chaotic mixing in plugs moving in meandering microchannels," *Physical Review E*, vol. 84, no. 6, p. 066309, 2011.
- [61] U. Tangen, A. Sharma, P. Wagler, and J. S. McCaskill, "On demand nanoliter-scale microfluidic droplet generation, injection, and mixing using a passive microfluidic device," *Biomicrofluidics*, vol. 9, no. 1, p. 014119, 2015.
- [62] Z.-H. Wei and C.-P. Lee, "Magnetic fluid micromixer with tapered magnets," *Journal of Applied Physics*, vol. 105, no. 7, p. 07B523, 2009.
- [63] M. Hejazian and N.-T. Nguyen, "A rapid magnetofluidic micromixer using diluted ferrofluid," *Micromachines*, vol. 8, no. 2, p. 37, 2017.
- [64] D. Owen, M. Ballard, A. Alexeev, and P. J. Hesketh, "Rapid microfluidic mixing via rotating magnetic microbeads," *Sensors and Actuators A: Physical*, vol. 251, pp. 84-91, 2016/11/01/ 2016.
- [65] N. Nama, P.-H. Huang, T. J. Huang, and F. Costanzo, "Investigation of micromixing by acoustically oscillated sharp-edges," *Biomicrofluidics*, vol. 10, no. 2, p. 024124, 2016.
- [66] S. Orbay, A. Ozcelik, J. Lata, M. Kaynak, M. Wu, and T. J. Huang, "Mixing high-viscosity fluids via acoustically driven bubbles," *Journal of Micromechanics and Microengineering*, vol. 27, no. 1, p. 015008, 2016.
- [67] Y. Abbas, J. Miwa, R. Zengerle, and F. von Stetten, "Active continuous-flow micromixer using an external braille pin actuator array," *Micromachines*, vol. 4, no. 1, pp. 80-89, 2013.
- [68] F. Zhang, H. Chen, B. Chen, and J. Wu, "Alternating current electrothermal micromixer with thin film resistive heaters," *Advances in Mechanical Engineering*, vol. 8, no. 5, p. 1687814016646264, 2016.
- [69] G. Kunti, A. Bhattacharya, and S. Chakraborty, "Rapid mixing with high-throughput in a semi-active semi-passive micromixer," *Electrophoresis*, vol. 38, no. 9-10, pp. 1310-1317, 2017.
- [70] E. Choi, K. Kwon, S. J. Lee, D. Kim, and J. Park, "Non-equilibrium electrokinetic micromixer with 3D nanochannel networks," *Lab on a Chip*, vol. 15, no. 8, pp. 1794-1798, 2015.
- [71] T. Zhou, H. Wang, L. Shi, Z. Liu, and S. W. Joo, "An enhanced electroosmotic micromixer with an efficient asymmetric lateral structure," *Micromachines*, vol. 7, no. 12, p. 218, 2016.
- [72] K. Ren, J. Zhou, and H. Wu, "Materials for microfluidic chip fabrication," *Accounts of chemical research*, vol. 46, no. 11, pp. 2396-2406, 2013.
- [73] Y. Xia and G. M. Whitesides, "Softlithographie," *Angewandte Chemie*, vol. 110, no. 5, pp. 568-594, 1998.
- [74] A. Folch, *Introduction to bioMEMS*. CRC Press, 2016.
- [75] N. Bhattacharjee, A. Urrios, S. Kang, and A. Folch, "The upcoming 3D-printing revolution in microfluidics," *Lab on a Chip*, vol. 16, no. 10, pp. 1720-1742, 2016.
- [76] D. Huh *et al.*, "Microfabrication of human organs-on-chips," (in eng), *Nat Protoc*, vol. 8, no. 11, pp. 2135-57, Nov 2013.

- [77] Y. Xia, "Whitesides. GM: 'Soft lithography'," *Angew. Chem., Int. Ed. Engl.*, vol. 37, pp. 550-575, 1998.
- [78] A. K. Au, W. Huynh, L. F. Horowitz, and A. Folch, "3D-printed microfluidics," *Angewandte Chemie International Edition*, vol. 55, no. 12, pp. 3862-3881, 2016.
- [79] S. Waheed *et al.*, "3D printed microfluidic devices: enablers and barriers," *Lab on a Chip*, vol. 16, no. 11, pp. 1993-2013, 2016.
- [80] H. Gong, B. P. Bickham, A. T. Woolley, and G. P. Nordin, "Custom 3D printer and resin for 18  $\mu\text{m}$   $\times$  20  $\mu\text{m}$  microfluidic flow channels," *Lab on a Chip*, vol. 17, no. 17, pp. 2899-2909, 2017.
- [81] M. D. Nelson, N. Ramkumar, and B. K. Gale, "Flexible, transparent, sub-100  $\mu\text{m}$  microfluidic channels with fused deposition modeling 3D-printed thermoplastic polyurethane," *Journal of Micromechanics and Microengineering*, vol. 29, no. 9, p. 095010, 2019.
- [82] V. Romanov, R. Samuel, M. Chaharlang, A. R. Jafek, A. Frost, and B. K. Gale, "FDM 3D Printing of High-Pressure, Heat-Resistant, Transparent Microfluidic Devices," *Analytical Chemistry*, vol. 90, no. 17, pp. 10450-10456, 2018/09/04 2018.
- [83] C. W. Hull, "Apparatus for production of three-dimensional objects by stereolithography," *United States Patent, Appl., No. 638905, Filed*, 1984.
- [84] A. Waldbaur, H. Rapp, K. Länge, and B. E. Rapp, "Let there be chip—towards rapid prototyping of microfluidic devices: one-step manufacturing processes," *Analytical Methods*, vol. 3, no. 12, pp. 2681-2716, 2011.
- [85] N. Fang, C. Sun, and X. Zhang, "Diffusion-limited photopolymerization in scanning micro-stereolithography," *Applied Physics A*, vol. 79, no. 8, pp. 1839-1842, 2004.
- [86] A. Bertsch, P. Bernhard, C. Vogt, and P. Renaud, "Rapid prototyping of small size objects," *Rapid Prototyping Journal*, 2000.
- [87] A. P. Kuo, N. Bhattacharjee, Y. S. Lee, K. Castro, Y. T. Kim, and A. Folch, "High-Precision Stereolithography of Biomicrofluidic Devices," *Advanced materials technologies*, vol. 4, no. 6, p. 1800395, 2019.
- [88] R. Nielson, B. Kaehr, and J. B. Shear, "Microreplication and design of biological architectures using dynamic-mask multiphoton lithography," *Small*, vol. 5, no. 1, pp. 120-125, 2009.
- [89] S. S. Crump, "Apparatus and method for creating three-dimensional objects," ed: Google Patents, 1992.
- [90] D. Pranzo, P. Larizza, D. Filippini, and G. Percoco, "Extrusion-based 3D printing of microfluidic devices for chemical and biomedical applications: A topical review," *Micromachines*, vol. 9, no. 8, p. 374, 2018.
- [91] G. Comina, A. Suska, and D. Filippini, "PDMS lab-on-a-chip fabrication using 3D printed templates," *Lab on a Chip*, vol. 14, no. 2, pp. 424-430, 2014.
- [92] H. N. Chan, Y. Chen, Y. Shu, Y. Chen, Q. Tian, and H. Wu, "Direct, one-step molding of 3D-printed structures for convenient fabrication of truly 3D PDMS microfluidic chips," *Microfluidics and nanofluidics*, vol. 19, no. 1, pp. 9-18, 2015.
- [93] K.-i. Kamei *et al.*, "3D printing of soft lithography mold for rapid production of polydimethylsiloxane-based microfluidic devices for cell stimulation with concentration gradients," *Biomedical microdevices*, vol. 17, no. 2, pp. 1-8, 2015.
- [94] J. C. McDonald, M. L. Chabinyk, S. J. Metallo, J. R. Anderson, A. D. Stroock, and G. M. Whitesides, "Prototyping of microfluidic devices in poly (dimethylsiloxane) using solid-object printing," *Analytical chemistry*, vol. 74, no. 7, pp. 1537-1545, 2002.

- [95] W. Lee *et al.*, "3D-printed microfluidic device for the detection of pathogenic bacteria using size-based separation in helical channel with trapezoid cross-section," *Scientific reports*, vol. 5, no. 1, pp. 1-7, 2015.
- [96] T. Monaghan, M. Harding, R. A. Harris, R. J. Friel, and S. Christie, "Customisable 3D printed microfluidics for integrated analysis and optimisation," *Lab on a Chip*, vol. 16, no. 17, pp. 3362-3373, 2016.
- [97] C. I. Rogers, K. Qaderi, A. T. Woolley, and G. P. Nordin, "3D printed microfluidic devices with integrated valves," *Biomicrofluidics*, vol. 9, no. 1, p. 016501, 2015.
- [98] A. K. Au, N. Bhattacharjee, L. F. Horowitz, T. C. Chang, and A. Folch, "3D-printed microfluidic automation," *Lab on a Chip*, vol. 15, no. 8, pp. 1934-1941, 2015.
- [99] J. L. Sanchez Noriega *et al.*, "Spatially and optically tailored 3D printing for highly miniaturized and integrated microfluidics," *Nature communications*, vol. 12, no. 1, pp. 1-13, 2021.
- [100] P. J. Kitson, M. H. Rosnes, V. Sans, V. Dragone, and L. Cronin, "Configurable 3D-Printed millifluidic and microfluidic 'lab on a chip' reactionware devices," *Lab on a Chip*, vol. 12, no. 18, pp. 3267-3271, 2012.
- [101] N. P. Macdonald, J. M. Cabot, P. Smejkal, R. M. Guijt, B. Paull, and M. C. Breadmore, "Comparing microfluidic performance of three-dimensional (3D) printing platforms," *Analytical chemistry*, vol. 89, no. 7, pp. 3858-3866, 2017.
- [102] L. Qian, "DNA fragment purification: removal of agarose 10 minutes after electrophoresis," *BioTechniques*, vol. 10, pp. 736-738, 1991.
- [103] J.-J. Poh and S. K.-E. Gan, "Comparison of customized spin-column and salt-precipitation finger-prick blood DNA extraction," *Bioscience Reports*, vol. 34, no. 5, 2014.
- [104] C. W. Price, D. C. Leslie, and J. P. Landers, "Nucleic acid extraction techniques and application to the microchip," *Lab on a Chip*, vol. 9, no. 17, pp. 2484-2494, 2009.
- [105] J. Křížová, A. Španová, B. Rittich, and D. Horák, "Magnetic hydrophilic methacrylate-based polymer microspheres for genomic DNA isolation," *Journal of chromatography A*, vol. 1064, no. 2, pp. 247-253, 2005.
- [106] N.-T. Nguyen, S. T. Wereley, and S. A. M. Shaegh, *Fundamentals and applications of microfluidics*. Artech house, 2019.
- [107] L. Nan, Z. Jiang, and X. Wei, "Emerging microfluidic devices for cell lysis: a review," *Lab on a Chip*, vol. 14, no. 6, pp. 1060-1073, 2014.
- [108] H. Lodish *et al.*, *Molecular cell biology*. Macmillan, 2008.
- [109] A. Olanrewaju, M. Beaugrand, M. Yafia, and D. Juncker, "Capillary microfluidics in microchannels: from microfluidic networks to capillaric circuits," *Lab on a Chip*, vol. 18, no. 16, pp. 2323-2347, 2018.
- [110] R. Ziv, Y. Steinhardt, G. Pelled, D. Gazit, and B. Rubinsky, "Micro-electroporation of mesenchymal stem cells with alternating electrical current pulses," *Biomedical microdevices*, vol. 11, no. 1, pp. 95-101, 2009.
- [111] S. K. Kim, J. H. Kim, K. P. Kim, and T. D. Chung, "Continuous low-voltage dc electroporation on a microfluidic chip with polyelectrolytic salt bridges," *Analytical chemistry*, vol. 79, no. 20, pp. 7761-7766, 2007.
- [112] C.-Y. Lee, G.-B. Lee, J.-L. Lin, F.-C. Huang, and C.-S. Liao, "Integrated microfluidic systems for cell lysis, mixing/pumping and DNA amplification," *Journal of Micromechanics and Microengineering*, vol. 15, no. 6, p. 1215, 2005.
- [113] S.-k. Baek, J. Min, and J.-H. Park, "Wireless induction heating in a microfluidic device for cell lysis," *Lab on a Chip*, vol. 10, no. 7, pp. 909-917, 2010.

- [114] D. Ahn, J.-H. Kweon, S. Kwon, J. Song, and S. Lee, "Representation of surface roughness in fused deposition modeling," *Journal of Materials Processing Technology*, vol. 209, no. 15-16, pp. 5593-5600, 2009.
- [115] T. Nancharaiah, D. R. Raju, and V. R. Raju, "An experimental investigation on surface quality and dimensional accuracy of FDM components," *International Journal on Emerging Technologies*, vol. 1, no. 2, pp. 106-111, 2010.
- [116] A. K. Sood, R. Ohdar, and S. S. Mahapatra, "Improving dimensional accuracy of fused deposition modelling processed part using grey Taguchi method," *Materials & design*, vol. 30, no. 10, pp. 4243-4252, 2009.
- [117] G. Percoco, F. Lavecchia, and L. M. Galantucci, "Compressive properties of FDM rapid prototypes treated with a low cost chemical finishing," *Research Journal of Applied Sciences, Engineering and Technology*, vol. 4, no. 19, pp. 3838-3842, 2012.
- [118] F. Li, N. P. Macdonald, R. M. Guijt, and M. C. Breadmore, "Using printing orientation for tuning fluidic behavior in microfluidic chips made by fused deposition modeling 3D printing," *Analytical chemistry*, vol. 89, no. 23, pp. 12805-12811, 2017.
- [119] H. Wang, P. Iovenitti, E. Harvey, and S. Masood, "Numerical investigation of mixing in microchannels with patterned grooves," *Journal of Micromechanics and Microengineering*, vol. 13, no. 6, p. 801, 2003.
- [120] D. da Silva *et al.*, "Biocompatibility, biodegradation and excretion of polylactic acid (PLA) in medical implants and theranostic systems," (in eng), *Chem Eng J*, vol. 340, pp. 9-14, May 15 2018.
- [121] N. Miložič, M. Lubej, U. Novak, P. Žnidaršič-Plazl, and I. Plazl, "Evaluation of diffusion coefficient determination using a microfluidic device," *Chemical and biochemical engineering quarterly*, vol. 28, no. 2, pp. 215-223, 2014.
- [122] J. Jadidian, M. Zahn, N. Lavesson, O. Widlund, and K. Borg, "Optimization of Artificial Diffusion Stabilization Techniques and Corresponding Mesh Density Distribution in Drift Dominated Transport of Diluted Species," 2012.
- [123] F. Schlegel. (2014, 21/04/2021). *Understanding Stabilization Methods*. Available: <https://www.comsol.com/blogs/understanding-stabilization-methods/>
- [124] (Jan ). *Masmec Biomed*. Available: <https://masmecbiomed.com/>
- [125] M. Zeraatkar, D. Filippini, and G. Percoco, "On the Impact of the Fabrication Method on the Performance of 3D Printed Mixers," *Micromachines*, vol. 10, no. 5, p. 298, 2019.
- [126] M. Zeraatkar, M. D. de Tullio, and G. Percoco, "Fused Filament Fabrication (FFF) for Manufacturing of Microfluidic Micromixers: An Experimental Study on the Effect of Process Variables in Printed Microfluidic Micromixers," *Micromachines*, vol. 12, no. 8, p. 858, 2021.
- [127] (2022, Jan). *NucleoMag Blood 200 μL* Available: <https://www.mn-net.com/nucleomag-blood-200-l-for-dna-purification-from-blood-744501.4>
- [128] (2022, JAN). *NucleoMag Plant kit* Available: <https://www.mn-net.com/nucleomag-plant-kit-for-dna-purification-from-plants-744400.4>
- [129] K. Lertphirun and K. Srikulkit, "Properties of Poly(Lactic Acid) Filled with Hydrophobic Cellulose/SiO<sub>2</sub> Composites," *International Journal of Polymer Science*, vol. 2019, p. 7835172, 2019/01/31 2019.
- [130] M. A. Ianovska, P. P. M. Mulder, and E. Verpoorte, "Development of small-volume, microfluidic chaotic mixers for future application in two-dimensional liquid chromatography," *RSC advances*, vol. 7, no. 15, pp. 9090-9099, 2017.

- [131] C. Li and T. Chen, "Simulation and optimization of chaotic micromixer using lattice Boltzmann method," *Sensors and Actuators B: Chemical*, vol. 106, no. 2, pp. 871-877, 2005.
- [132] M. G. Guerra, C. Volpone, L. M. Galantucci, and G. Percoco, "Photogrammetric measurements of 3D printed microfluidic devices," *Additive Manufacturing*, vol. 21, pp. 53-62, 2018/05/01/ 2018.
- [133] D. Pranzo, P. Larizza, D. Filippini, and G. Percoco, "Extrusion-Based 3D Printing of Microfluidic Devices for Chemical and Biomedical Applications: A Topical Review," *Micromachines*, vol. 9, no. 8, 2018.
- [134] C. Simonnet and A. Groisman, "Chaotic mixing in a steady flow in a microchannel," *Physical review letters*, vol. 94, no. 13, p. 134501, 2005.

# Appendix A

In this section printing parameters in Cura software are shown for different devices.

## a) Setting parameters for devices with a line width of 0.2 mm and layer height of 0.1 mm

The image shows three panels of Cura software settings. The top-left panel shows the 'Quality' section with various line width and layer height parameters. The top-right panel shows the 'Shell' section with extruder and wall thickness settings. The bottom-left panel shows the 'Shell' section with various printing options like 'Outer before inner walls' and 'Minimum Wall Flow'. The bottom-right panel shows the 'Infill' section with settings for 'Infill Extruder', 'Infill Density', and 'Infill Line Distance'.

Section	Parameter	Value	Unit
Quality	Layer Height	0.1	mm
	Initial Layer Height	0.17	mm
	Line Width	0.2	mm
	Wall Line Width	0.2	mm
	Outer Wall Line Width	0.2	mm
	Inner Wall(s) Line Width	0.23	mm
	Top/Bottom Line Width	0.2	mm
	Infill Line Width	0.2	mm
	Skirt/Brim Line Width	0.2	mm
	Support Line Width	0.2	mm
	Prime Tower Line Width	0.2	mm
	Initial Layer Line Width	120	%
Shell	Wall Extruder	Not overridden	
	Outer Wall Extruder	Not overridden	
	Inner Wall Extruder	Not overridden	
	Wall Thickness	0.7	mm
	Wall Line Count	3	
Shell (continued)	Outer Wall Wipe Distance	0.25	mm
	Top/Bottom Extruder	Not overridden	
	Top/Bottom Thickness	0.72	mm
	Top Thickness	0.72	mm
	Top Layers	0	
	Bottom Thickness	0.72	mm
	Bottom Layers	999999	
	Top/Bottom Pattern	Lines	
	Bottom Pattern Initial Layer	Lines	
	Top/Bottom Line Directions	[ ]	
	Outer Wall Inset	0.015	mm
	Optimize Wall Printing Order	<input checked="" type="checkbox"/>	
Infill	Infill Extruder	Extruder 1	
	Infill Density	100	%
	Infill Line Distance	0.2	mm
	Infill Pattern	Grid	
	Connect Infill Lines	<input checked="" type="checkbox"/>	
	Infill Line Directions	[ ]	
	Infill X Offset	0	mm
	Infill Y Offset	0	mm
	Infill Line Multiplier	1	
	Extra Infill Wall Count	0	
	Infill Overlap Percentage	10	%
	Infill Overlap	0	mm
Skin Overlap Percentage	5	%	
Skin Overlap	0.0108	mm	
Outer before inner walls	<input type="checkbox"/>		
Alternate Extra Wall	<input type="checkbox"/>		
Compensate Wall Overlaps	<input checked="" type="checkbox"/>		
Compensate Outer Wall Overlaps	<input checked="" type="checkbox"/>		
Compensate Inner Wall Overlaps	<input checked="" type="checkbox"/>		
Minimum Wall Flow	0	%	
Fill Gaps Between Walls	Everywhere		
Filter Out Tiny Gaps	<input checked="" type="checkbox"/>		
Print Thin Walls	<input type="checkbox"/>		
Horizontal Expansion	0	mm	
Initial Layer Horizontal Expansion	0	mm	
Z Seam Alignment	Sharpest Corner		
Seam Corner Preference	Hide Seam		
Ignore Small Z Gaps	<input type="checkbox"/>		
Extra Skin Wall Count	1		
Enable Ironing	<input checked="" type="checkbox"/>		
Iron Only Highest Layer	<input checked="" type="checkbox"/>		
Ironing Pattern	Zig Zag		

### Material

Default Printing Temperature	200	°C
Printing Temperature	190	°C
Printing Temperature Initial Layer	195	°C
Initial Printing Temperature	180	°C
Final Printing Temperature	175	°C
Extrusion Cool Down Speed Modifier	0.7	°C/s
Default Build Plate Temperature	60	°C
Build Plate Temperature	60	°C
Build Plate Temperature Initial Layer	60	°C
Flow	100	%
Initial Layer Flow	100	%
Enable Retraction	<input checked="" type="checkbox"/>	
Retract at Layer Change	<input type="checkbox"/>	
Retraction Distance	6.5	mm
Retraction Speed	25	mm/s

### Speed

Print Speed	30	mm/s
Infill Speed	30	mm/s
Wall Speed	25	mm/s
Outer Wall Speed	20	mm/s
Inner Wall Speed	25	mm/s
Top/Bottom Speed	20	mm/s
Support Speed	20	mm/s
Support Infill Speed	20	mm/s
Prime Tower Speed	20	mm/s
Travel Speed	250	mm/s
Initial Layer Speed	30	mm/s
Initial Layer Print Speed	30	mm/s
Initial Layer Travel Speed	120	mm/s
Skirt/Brim Speed	30	mm/s

### Support

Generate Support	<input checked="" type="checkbox"/>
Support Extruder	Extruder 1
Support Infill Extruder	Extruder 1
First Layer Support Extruder	Extruder 1
Support Interface Extruder	Extruder 1
Support Roof Extruder	Extruder 1
Support Floor Extruder	Extruder 1
Support Placement	Everywhere
Support Overhang Angle	60
Support Pattern	Zig Zag
Support Wall Line Count	0
Connect Support ZigZags	<input checked="" type="checkbox"/>
Support Density	15
Support Line Distance	1.3333
Initial Layer Support Line Distance	1.3333

### Build Plate Adhesion

Use Towers	<input checked="" type="checkbox"/>
Tower Diameter	3.0
Minimum Diameter	3.0
Tower Roof Angle	65
Enable Prime Blob	<input checked="" type="checkbox"/>
Build Plate Adhesion Type	Brim
Build Plate Adhesion Extruder	Extruder 1
Skirt/Brim Minimum Length	250
Brim Width	8
Brim Line Count	16
Brim Replaces Support	<input checked="" type="checkbox"/>
Brim Only on Outside	<input checked="" type="checkbox"/>

- Dual Extrusion** <
- Mesh Fixes** <
- Special Modes** <
- Experimental** <

**b) Setting parameters for devices with a line width of 0.6 mm and layer height of 0.1 mm**

Quality	
Layer Height	0.1 mm
Initial Layer Height	0.27 mm
<b>Line Width</b>	0.6 mm
Wall Line Width	0.6 mm
Outer Wall Line Width	0.4 mm
Inner Wall(s) Line Width	0.51 mm
Top/Bottom Line Width	0.6 mm
Infill Line Width	0.6 mm
Skirt/Brim Line Width	0.6 mm
Support Line Width	0.6 mm
Initial Layer Line Width	120 %
Shell	
Wall Extruder	Not overridden
Outer Wall Extruder	Not overridden
Inner Wall Extruder	Not overridden
Wall Thickness	1 mm
Wall Line Count	3
Outer Wall Wipe Distance	0.2 mm
Top/Bottom Extruder	Not overridden
Top/Bottom Thickness	1 mm
Top Thickness	1 mm
Top Layers	0
Bottom Thickness	1 mm
Bottom Layers	999999
Top/Bottom Pattern	Lines
Bottom Pattern Initial Layer	Lines
Top/Bottom Line Directions	[ ]
Outer Wall Inset	0 mm
Optimize Wall Printing Order	<input checked="" type="checkbox"/>
Outer Before Inner Walls	<input type="checkbox"/>
Alternate Extra Wall	<input type="checkbox"/>
Compensate Wall Overlaps	<input checked="" type="checkbox"/>
Compensate Outer Wall Overlaps	<input checked="" type="checkbox"/>
Compensate Inner Wall Overlaps	<input checked="" type="checkbox"/>
Minimum Wall Flow	0 %
Fill Gaps Between Walls	Everywhere
Filter Out Tiny Gaps	<input checked="" type="checkbox"/>
Print Thin Walls	<input type="checkbox"/>
Horizontal Expansion	0 mm
Initial Layer Horizontal Expansion	0 mm
Z Seam Alignment	Sharpest Corner
Seam Corner Preference	Hide Seam
Ignore Small Z Gaps	<input type="checkbox"/>
Extra Skin Wall Count	1
Enable Ironing	<input checked="" type="checkbox"/>
Iron Only Highest Layer	<input checked="" type="checkbox"/>
Ironing Pattern	Zig Zag
Ironing Line Spacing	0.1 mm
Ironing Flow	10.0 %
Ironing Inset	0.185 mm
Infill	
Infill Extruder	Extruder 1
Infill Density	100 %
Infill Line Distance	0.6 mm
Infill Pattern	Grid
Connect Infill Lines	<input checked="" type="checkbox"/>
Infill Line Directions	[ ]
Infill X Offset	0 mm
Infill Y Offset	0 mm
Infill Line Multiplier	1
Extra Infill Wall Count	0
Infill Overlap Percentage	0 %
Infill Overlap	0 mm
Skin Overlap Percentage	10 %
Skin Overlap	0.05 mm
Infill Wipe Distance	0 mm

Material		Speed	
Default Printing Temperature	200 °C	Print Speed	70 mm/s
Printing Temperature	200 °C	Infill Speed	70 mm/s
Printing Temperature Initial Layer	205 °C	Wall Speed	30 mm/s
Initial Printing Temperature	190 °C	Outer Wall Speed	20 mm/s
Final Printing Temperature	185 °C	Inner Wall Speed	30 mm/s
Extrusion Cool Down Speed Modifier	0.7 °C/s	Top/Bottom Speed	30 mm/s
Default Build Plate Temperature	60 °C	Support Speed	20 mm/s
Build Plate Temperature	60 °C	Support Infill Speed	20 mm/s
Build Plate Temperature Initial Layer	60 °C	Travel Speed	250 mm/s
Flow	100 %	Initial Layer Speed	20 mm/s
Initial Layer Flow	100 %	Initial Layer Print Speed	20 mm/s
Enable Retraction	<input checked="" type="checkbox"/>	Initial Layer Travel Speed	71.4286 mm/s
Retract at Layer Change	<input type="checkbox"/>	Skirt/Brim Speed	20 mm/s
Retraction Distance	6.5 mm	Maximum Z Speed	0 mm/s
Retraction Speed	25 mm/s	Number of Slower Layers	2
Retraction Retract Speed	25 mm/s		
Retraction Prime Speed	25 mm/s		

Support		Build Plate Adhesion	
Generate Support	<input checked="" type="checkbox"/>	Enable Support Roof	<input type="checkbox"/>
Support Extruder	Extruder 1	Enable Support Floor	<input type="checkbox"/>
Support Infill Extruder	Extruder 1	Fan Speed Override	<input type="text"/>
First Layer Support Extruder	Extruder 1	Use Towers	<input checked="" type="checkbox"/>
Support Interface Extruder	Extruder 1	Tower Diameter	3.0 mm
Support Roof Extruder	Extruder 1	Minimum Diameter	3.0 mm
Support Floor Extruder	Extruder 1	Tower Roof Angle	65 °
Support Placement	Everywhere	<b>Build Plate Adhesion</b>	
Support Overhang Angle	60 °	Enable Prime Blob	<input checked="" type="checkbox"/>
Support Pattern	Zig Zag	Build Plate Adhesion Type	Brim
Support Wall Line Count	0	Build Plate Adhesion Extruder	Extruder 1
Connect Support ZigZags	<input checked="" type="checkbox"/>	Skirt/Brim Minimum Length	250 mm
Support Density	15 %	Brim Width	7 mm
Support Line Distance	4.0 mm	Brim Line Count	8
		Brim Replaces Support	<input checked="" type="checkbox"/>
		Brim Only on Outside	<input checked="" type="checkbox"/>

## Appendix B

### Colorimetric Analysis Algorithm

```
% ANALYSIS MIXING IN SIMPLE Y-SHAPED MICRO-MIXER BY MOJTABA
ZERAATKAR
%%

AA = imread ('IMG_0247.jpg');
% imshow(AA);
hsv = rgb2hsv(AA);
hChannel = hsv(:, :, 1);
sChannel = hsv(:, :, 2);
vChannel = hsv(:, :, 3);
hChannel = hChannel * 1; % Or whatever...
hsv = cat(3, hChannel, sChannel, vChannel);
rgbVivid = hsv2rgb(hsv);
imshow(rgbVivid);
% AA=imresize(AA,0.5);
% [M,N]=size(AA);
background=imopen(AA,strel('disk',10));
I=imsubtract(AA,background);
BW=rgb2gray(rgbVivid);
fig1 = figure(1);
imshow(BW);
bin=imbinarize(BW);
bin=bwareaopen(bin,5);
bin=edge(bin,'sobel');

%calculation center line of the channel

% [c,d]=size(bin);
% bin2=zeros(c,d);
%     for k=c:-1:1,
%         for h=d:-1:1,
%             if bin(k,h)==1
% %                 for s=k-1:-1:1,
%                     for s=1:k-1,
%                         if bin(s,h)==1
%                             m=(k+s)/2;
%                             m=fix(m);
%                             bin2(m,h)=1;
%                             bin(:,h)=0;
%                         end
%                     end
%                 end
%             end
%         end
%     end
```

```

%             end
%         end
%     end
% end

fig2 = figure(2);
imshow(bin);
Q=imline;
W=wait(Q);
W=round(W);
x=W(1,1)+1;
y1=W(1,2);

BB = AA;
% r=28;
r =45;
r1=90;
L=0;
for i=1:20
    cc(i,:)=[x y1+L r];
    L=L+200;
%     L=L+130;
    x=x+0.1;
%     x=x-5.8;
end

CC=cc';

for i = 1:20
    BB(CC(2,i):CC(2,i)+r1,CC(1,i):CC(1,i)+r,:) = 255;
end

fig3 = figure(3);
fig3.WindowStyle = 'docked';
image(BB(:,:, :));
hold on;
for i = 1:20
    text(CC(1,i)+r/3,CC(2,i)+r1/2,num2str(i));
end
%axis([0 700 300 1000]);
hold off;

c(1).cdata = AA;

```

```

rr = r;
k=1;
DD = c(k).cdata;
% ch = 3;
corr1 = 1.15;
%
for ch=1:3
for i=1:20

    col((i-1)*r1+1:i*r1+1,1+(k-1)*rr:k*rr+1,:) =...
    DD(CC(2,i):CC(2,i)+r1,CC(1,i):CC(1,i)+r,:).*corr1;
    comp(i,:,ch) =
mean(DD(CC(2,i):CC(2,i)+r1,CC(1,i):CC(1,i)+r,ch));
    comp(i,:,ch) = comp(i,:,ch).*corr1;
end

    comp1(ch) = mean(comp(1,1:r/2,ch));
    comp2(ch) = mean(comp(1,r/2+1:r,ch));
    diff(ch) = abs(comp2(ch)-comp1(ch));

end

[M,I] = max(diff);
ch=I;

for i=1:20

    col((i-1)*r1+1:i*r1+1,1+(k-1)*rr:k*rr+1,:) =...
    DD(CC(2,i):CC(2,i)+r1,CC(1,i):CC(1,i)+r,:).*corr1;
    roi(:,i) =
mean(DD(CC(2,i):CC(2,i)+r1,CC(1,i):CC(1,i)+r,ch))';
    sroi(:,i) =
std(double(DD(CC(2,i):CC(2,i)+r1,CC(1,i):CC(1,i)+r,ch)))';
    roi(:,i) = roi(:,i).*corr1;

end

fig4 = figure(4);
fig4.WindowStyle = 'docked';
temp = winter(255);
for i = 1:255
    mswinter(i,:) = temp(end+1-i,:);
end

```

```

colormap(mswinter)
imagesc(col(:,:,ch));
grid on;
colorbar

roi_back = mean(roi(1:2,:));
sroi_back = mean(sroi(1:2,:));
roi = roi-roi_back;
sroi = sroi-sroi_back;

fig5 = figure(5);
fig5.WindowStyle = 'docked';
box on;
hold on;

colorm = jet(20);
for i = 1:20
    plot(roi(:,i), 'v-', 'LineWidth', 2, 'Color', colorm(end+1-i,:));

end
legend('roi 1','roi 2','roi 3','roi 4','roi 5','roi 6','roi 7','roi
8','roi 9','roi 10','roi 11','roi 12','roi 13','roi 14','roi
15','roi 16','roi 17','roi 18','roi 19','roi 20','roi 21','roi
22','roi 23','roi 24','roi 25','roi 26','roi 27','roi 28','roi
29','roi 30','roi 31','roi 32','roi 33','roi 34','roi 35','roi
36','roi 37','roi 38','roi 39','roi 40');
%axis([11 20 -60 10]);
hold off;

cut = 20;

fig6 = figure(6);
fig6.WindowStyle = 'docked';
box on;
hold on;
% colorm = winter(cut);
for i = 1:cut
    errorbar(roi(:,i), sroi(:,i), 'LineWidth', 2, 'Color', colorm(end+1-
i,:));

```

```

end
legend('roi 1','roi 2','roi 3','roi 4','roi 5','roi 6','roi 7','roi
8','roi 9','roi 10','roi 11','roi 12','roi 13','roi 14','roi
15','roi 16','roi 17','roi 18','roi 19','roi 20','roi 21','roi
22','roi 23','roi 24','roi 25','roi 26','roi 27','roi 28','roi
29','roi 30','roi 31','roi 32','roi 33','roi 34','roi 35','roi
36','roi 37','roi 38','roi 39','roi 40');

% axis([10 20 -80 40]);
hold off;

fig7 = figure(7);
fig7.WindowStyle = 'docked';
box on;
meanr=zeros(20,1);
for i=1:20
    mse(i)=mean((mean(roi(:,i))-roi(:,i)).^2);
end
plot(mse,'r*-','LineWidth',1);
% axis([0 20 0 1000]);
fig8 = figure(8);
fig8.WindowStyle = 'docked';
box on;
% for i=1:20
% mse(i)=sum((roi(:,i)-meanr(i)).^2);
% end
% roiSM = roi(11,:);
rmax = max(mse);
rmin = min(mse);
roiN = (mse-rmin)/(rmax-rmin);
% sroiN = sroi(11,:)/(rmax-rmin);
plot(roiN,'go-','LineWidth',2);
% axis([1 20 0 1]);

% fig9 = figure(9);
% fig9.WindowStyle = 'docked';
% box on;

% rmax = max(roi(11,:));
% rmin = min(roi(11,:));

```

```

% roiN = (roi(11,:)'-rmin)/(rmax-rmin);
% sroiN = sroi(11,:)'/ (rmax-rmin);

% x = 1:cut;
% p = polyfit(x',roiN(1:cut),4);
% y1 = polyval(p,x');

% save('FDM15','roiN','sroiN','y1');
%
% hold on;
% plot(y1,'r-','LineWidth',2);
% errorbar(roiN(1:cut),sroiN(1:cut),'ko','LineWidth',1);
% axis([1 20 0 1]);
% hold off

```